NONLINEAR STOCHASTIC TOMOGRAPHY RECONSTRUCTION ALGORITHMS FOR OBJECTS WITH HELICAL SYMMETRY AND APPLICATIONS TO VIRUS STRUCTURES

A Thesis

Presented to the Faculty of the Graduate School

of Cornell University

in Partial Fulfillment of the Requirements for the Degree of

Master of Science

by

Qiaoyun Chen

January 2009

ABSTRACT

Natural and synthetic biological objects, e.g., Tobacco Mosaic Virus and tubes from bacteriophage P22 hexamers, form a large class of helically-symmetric biological nano-scale objects. Helical symmetry is a class of symmetries described by two relatively prime integers (u, v) and a period c. Typically u, v, and c are all unknown. Electron microscopy provides a method of visualizing such objects in 3-D via computational reconstruction from projection 2-D image measurements. Damage of the object by the electron beam restricts high-resolution studies to a single image of an unoriented object at low (≤ 0.2) SNR. This work considers the frequently-occurring case where multiple identical objects are available and so multiple images, one of each object, can be combined by computation to achieve a 3-D reconstruction of the object. Due to the poor SNR, the focus of this work is on maximum likelihood (ML) estimators to determine the reconstruction. The unknown orientation of the object in the microscope and the period of the helical symmetry are treated as nuisance parameters and the joint ML estimate of (u, v) and the parameters that describe the 3-D structure given the helical symmetry parameters is computed via an expectation maximization approach. This approach contrasts with a variety of current approaches which separate symmetry determination from reconstruction and which do not use explicit statistical models of the noise. Examples of the application of this approach to synthetic and experimental images from Tobacco Mosaic Virus are described.

BIOGRAPHICAL SKETCH

Qiaoyun Chen was born in 1983 to Jian Chen and Yuexiu Guo in Fujian, China. She came to the U.S.A. in February, 2000. She was a 2002 graduate of Jeffersonville-Youngsville High School, Jeffersonville, NY.

She received the B.S. degree in electrical and computer engineering from Rutgers University, New Brunswick, NJ in 2006. Her research interests include multidimensional signal processing, statistical signal processing, mathematical modeling, and inverse problems.

This document is dedicated to all Cornell graduate students.

ACKNOWLEDGEMENTS

My utmost gratitude goes to my advisor, Dr. Peter C. Doerschuk for his dedication in guiding me to success. His kindness, humor, patience and continuous support made this thesis possible. What I learned from him is far greater than my academic accomplishments. I am forever grateful for being a student of his. I would also like to thank John E. Johnson for stimulating the biological motivation for this work.

I would like to thank numerous colleagues. Seunghee Lee and Yili Zheng had generously provided me with documents and guidelines to jump-start the project. Bin Wang and Nathan R. Cornelius have been good friends who are always ready with assistances. I sincerely thank Kang Wang for valuable discussions and being enthusiastic all the time. I would also like to recognize and thank the staff and community of the Cornell University.

My deepest appreciation goes to my parents who tirelessly offered me tremendous supports and encouragements. The last but not the least, I would like to give my special thanks to Jin Zhang for being always by my side. With him on my side, I am never lost .

TABLE OF CONTENTS

LIST OF TABLES

LIST OF FIGURES

CHAPTER 1

INTRODUCTION

In this document, we present a statistical method to simultaneously determine the helical symmetry parameters and the electron scattering intensity as a function of 3-D spatial coordinates for an object based on electron microscopy images of the object. A novel extended Fourier-Bessel model is used where the Bessel order terms are replaced by a linear superposition of orthogonal basis functions. This method does not require that the orientation of the object shown in each image be determined before the 3-D reconstruction is computed. This method also does not require reference frames. Instead, this method includes all possible alignment parameters as nuisance parameters in a maximum likelihood (ML) estimator which is computed by an Expectation Maximization (EM) algorithm. If desired, the correct orientation can be determined as the orientation that results the highest likelihood given that the true structure is the same as the structure resulting from the ML estimator. A further advantage of this method is the automated processing of multiple images.

CHAPTER 2

PREVIOUS WORK

Objects with helical symmetry are studied. The primary motivation for studying objects with helical symmetry is the occurrence of viruses with such symmetry, especially Tobacco Mosaic Virus (TMV). Extensive theory has been developed for objects with helical symmetry [5]. Typically, both the electron scattering intensity as a function of 3-D spatial coordinates and the parameters of the helical symmetry are unknown and therefore are the goal of the computation. The helical symmetry implies that a single image of an object provides limited 3-D information because each object contains the asymmetric unit of the helical symmetry in a fixed set of different orientations [6]. To achieve a resolution of 20Å or better, additional views of the asymmetric unit of the helical symmetry are required. These views are provided by images of other objects in the electron microscope's field of view which are rotated about their helical axis relative to the first object. Therefore, tilting the stage of the microscope is unnecessary.

A Fourier-Bessel model representing the reciprocal space of an object with helical symmetry has been developed [7]. Due to the periodicity in the direction of the helical axis, the 3-D and 2-D reciprocal space of a helical object is made up of layer planes and layer lines, respectively. In order to reconstruct the particle, the problem becomes to determine the Bessel order terms on each layer line. This can be difficult since on each layer line, there are many Bessel order terms, and they cannot be easily separated.

Methods using the x-ray scattering pattern from ordered or partially ordered ensembles of particles have been studied extensively [8, 9, 10, 11]. The main challenge in the analysis of x-ray patterns is that the phase information for the

layer lines is lost. On the other hand, if using electron micrographs, the phase information is maintained, and the difficulty becomes to accurately determine the Contrast Transfer Function (CTF) that describes the effect of the microscope.

An atomic resolution of 2.9Å was achieved by Namba *et al.* in 1989 using x-ray diffraction data. Various researchers before that had also tried to reconstruct TMV using x-ray diffraction data. For example, in 1972, Barrett *et al.* [8] made an electron-density map of TMV at 10Å using the isomorphous replacement method (which was first introduced in Ref. [12]) to determine the helical parameters. Since then, the extended isomorphous replacement method had been employed to solve the phase problem when using data from x-ray diffraction pattern. In 1975, Holmes *et al.* [9] achieved 6.7Å in reconstructing TMV. In 1985, Namba *et al.* [10] also applied the method of isomorphous replacement; in addition, they made use of layer line splitting to get extra phase information. As a result, it was possible to separate five Bessel order terms per layer line, and a resolution of 3.6Å was achieved.

The fact that TMV diffraction pattern exhibits layer line splitting was first mentioned and explained in Ref. [13] in 1958. The helical parameters for TMV are (u, v, c). The reason the layer lines split is that the number of motifs for TMV is not an integer. If u/v is not rational, then a true axial repeat does not exist. That is to say, the Bessel-function contributions from different origins will no longer lie at exactly the same level, but will lie on either side of the mean layer lines that correspond to the rational approximation to u/v. When u is not an integer, the departure from an exact integer ratio will manifest itself as a splitting of the layer lines.

Researchers had also performed reconstructions from electron micrograph data [6, 14, 3]. In 1968, DeRosier and Klug [6] described the idea of using the projection slice theorem in reconstructing a three dimensional structure from electron micrographs. Over the succeeding years, several additional papers described methods related to reconstruct an object with helical symmetry [2, 5, 15, 16, 17]. In 1989, Jeng *et al.* [17] were able to resolve the structure to 10Å using 12 electron micrographs with sampling interval of 1.7Å per pixel. The images had observable data in the 7th layer line and, in theory, it is possible to reach 10Å if the 7th layer line of TMV could be computed. Three different defocus values for the CTF were present among the twelve images in order to retrieve the entire set of structure factors. CTF defocus and amplitude were furthered adjusted by examining the electron microscopy data and comparing to the x-ray model data. The procedures used to do the 3-D reconstruction were presented in Ref. [18]: first determine the relative orientations and axial displacement and then separate the Bessel terms by solving a linear system.

Determination of the orientation parameters can be difficult, especially when the Bessel-term overlap is severe. If the Bessel-term overlap is not severe, the orientation relationship between two images of the helix can be calculated by comparing the phases of layer lines closest to the meridian where there is only single Bessel term that contributes strongly to the layer line. If the Bessel overlap is severe, then an iterative Fourier-Bessel algorithm for determining the orientations can be applied [19].

All the work described above made use of the Fourier-Bessel model. Using reciprocal-space procedures, indexing is needed first to determine the helical parameters. Some real-space single particle procedures, such as IHRSR [20], can

determine the helical parameters automatically. IHRSR was developed by Egelman and collaborators which has been applied to reconstruct helical structures. Since it does not work in reciprocal space, the Bessel order overlap problem is avoided. The method describes a process which first imposes the helical symmetry on the estimated structure, then compares the estimated structure with reference projections to determine azimuthal rotation, and finally back projects images with assigned alignment (translational and rotational) to compute the 3-D structure. Sachse *et al.* [21] reconstructed TMV to 5Å using an extended IHRSR procedure with further CTF correction, introducing alignment parameters, and optimizing the helical symmetry of TMV. 135 images with sampling interval of 1.163Å per pixel were used. Images were broken up into segments with 90% overlap between successive segments. In total, 4251 segments, each of 770Å $\times$ 770Å were used in the processing. Each of the 4251 segments was included 50 times in the 3-D reconstruction to cover all symmetry-related views of TMV. Alignment parameters (α, β, γ) for rotational alignment and (x_{L_1}, x_{L_2}) for translational alignment were introduced, with α and β being processed one degree per step. In addition to normal CTF correction, after 3-D reconstruction of the volume from the CTF-corrected images, the amplitudes of the reconstruction were corrected again using sum-squared 3-D CTFs. Finally, additional refinement on the atomic model was applied to reconstruct the structure to atomic resolution.

In the following chapters, we present a new approach, using the extended Fourier-Bessel model, to perform the helical reconstruction.

CHAPTER 3

MATHEMATICAL PRELIMINARIES

Standard notation for the 2-D and 3-D vectors in real and reciprocal space in both rectangular and cylindrical coordinates (e.g., Ref. [22, p. 190]) is used as is described in Tables 3.1 and 3.2. The symbols $\mathcal{Z}$, $\mathcal{Z}^+$, $\mathbb{R}$, and $\mathbb{R}^+$ indicate the integers, positive integers, real numbers, and positive real numbers, respectively. The Fourier transform pair is defined by

$$F(\mathbf{k}) = \int_{\mathbf{x}} \rho(\mathbf{x}) \exp\left(-i2\pi\mathbf{k}^T\mathbf{x}\right) \mathrm{d}\mathbf{x} \tag{3.1}$$

$$\rho(\mathbf{x}) = \int_{\mathbf{k}} F(\mathbf{k}) \exp\left(+i2\pi\mathbf{k}^T\mathbf{x}\right) \mathrm{d}\mathbf{k} \tag{3.2}$$

for any dimension. The uth-order cylindrical Hankel transform pair is defined by

$$A_u(k) = 2\pi \int_0^\infty a(r) J_u(2\pi r k) r \mathrm{d}r \tag{3.3}$$

$$a(r) = 2\pi \int_0^\infty A_u(k) J_u(2\pi r k) k \mathrm{d}k. \tag{3.4}$$

Rotations are typically described by Euler angles (α, β, γ) using the conventions of Ref. [23, pp. 50–51] and the rotation matrix, denoted by R, is given by Ref. [23, Eq. 4.43, p. 65]. All rotation matrices satisfy $R^{-1} = R^T$ and $\det R = 1$. Let $\delta_{m,n}$ denote the Kronecker δ function which is defined by

$$\delta_{m,n} = \begin{cases} 1 & m = n \\ 0 & m \neq n \end{cases} \tag{3.5}$$

Table 3.1: Terminology for real- and reciprocal-space vectors in 2-D.

2-D			
	Abstract	Rectangular	Polar
Real	$\boldsymbol{\chi}$	$(\chi_1, \chi_2)^T$	(r, φ)
Reciprocal	$\boldsymbol{\kappa}$	$(\kappa_1, \kappa_2)^T$	(R, ψ)

Table 3.2: Terminology for real- and reciprocal-space vectors in 3-D.

3-D			
	Abstract	Rectangular	Cylindrical
Real	$\mathbf{x}$	$(x_1, x_2, x_3)^T$	(r, φ, z)
Reciprocal	$\mathbf{k}$	$(k_1, k_2, k_3)^T$	(R, ψ, ζ)
	$\mathbf{k}_L = R^{-1}\mathbf{k}$	$(k_{L_1}, k_{L_2}, k_{L_3})^T$	(R_L, ψ_L, ζ_L)
	$\mathbf{k}'_L = R^{-1}(k_1, k_2, 0)^T$	$(k'_{L_1}, k'_{L_2}, k'_{L_3})^T$	$(R'_L, \psi'_L, \zeta'_L)$

or, if the second argument is a subset of $\mathcal{Z}$, by

$$\delta_{m,S} = \begin{cases} 1, & m \in S \\ 0, & \text{otherwise} \end{cases} . \tag{3.6}$$

The Dirac δ function is denoted by $\delta(\cdot)$.

CHAPTER 4

MATHEMATICAL MODEL OF THE 3-D OBJECT

4.1 Objects that are periodic in one of three dimensions

In this chapter, the standard Fourier-Bessel model [7, 22] is derived in preparation for our generalization in later chapters. A helical object has infinite extent in one direction and is periodic with period $c \in \mathbb{R}^+ \cup \{0\}$ in that direction. (The period is sometimes called the axial repeat of the helix). Therefore it is natural to describe the helical object in cylindrical coordinates, denoted by (r, φ, z), where the z axis of the coordinate system corresponds with the periodic direction of the helix. Let the electron scattering intensity be denoted by $\rho(\mathbf{x}) = \rho(r, \varphi, z)$. The periodicity in z corresponds to

$$\rho(r, \varphi, z) = \rho(r, \varphi, z + mc) \tag{4.1}$$

for $m \in \mathcal{Z}$. Because $\rho(r, \varphi, z)$ is periodic in φ with period 2π by definition and periodic in z with period c by assumption, it follows that $\rho(r, \varphi, z)$ can be expanded as a double Fourier series in φ and z [24]:

$$\rho(r, \varphi, z) = \sum_{l=-\infty}^{+\infty} \sum_{n=-\infty}^{+\infty} g_{n,l}(r) \exp\left[i\left(n\varphi + \frac{2\pi}{c} lz\right)\right] \tag{4.2}$$

where the weights $g_{n,l}(r)$ can be computed by

$$g_{n,l}(r) = \frac{1}{2\pi c} \int_{z=0}^{c} \int_{\varphi=0}^{2\pi} \rho(r, \varphi, z) \exp\left[-i\left(n\varphi + \frac{2\pi}{c} lz\right)\right] \mathrm{d}\varphi \mathrm{d}z \tag{4.3}$$

for all $n \in \mathcal{Z}$ and $l \in \mathcal{Z}$. The key to compute the 3-D Fourier transform of $\rho(\mathbf{x})$ is to derive the relationship between $\exp\left(-i2\pi \mathbf{k}^T \mathbf{x}\right)$ and the components of $\mathbf{k}$ and $\mathbf{x}$ in cylindrical coordinates. This relationship can be derived as follows:

$$\exp\left(-i2\pi \mathbf{k}^T \mathbf{x}\right) = \exp\left[-i2\pi \left(Rr\cos\varphi\cos\psi + Rr\sin\varphi\sin\psi + z\zeta\right)\right] \tag{4.4}$$

$$
\begin{aligned}
& \text{Use } \cos(\varphi-\psi)=\cos\varphi\cos\psi+\sin\varphi\sin\psi \text{ to get} \\
= \;& \exp\left[-i2\pi\left(Rr\cos(\varphi-\psi)+z\zeta\right)\right] && (4.5) \\
& \text{Use } \cos(\omega)=\sin(\pi/2-\omega) \text{ to get} \\
= \;& \exp\left[-i2\pi\left(Rr\sin\left(\frac{\pi}{2}-\varphi+\psi\right)+z\zeta\right)\right] && (4.6) \\
= \;& \exp(-i2\pi z\zeta)\exp\left[-i2\pi Rr\sin\left(\frac{\pi}{2}-\varphi+\psi\right)\right] && (4.7) \\
= \;& \exp(-i2\pi z\zeta)\sum_{n=-\infty}^{\infty}\exp\left[-in\left(\frac{\pi}{2}-\varphi+\psi\right)\right]J_n(2\pi Rr) && (4.8)
\end{aligned}
$$

where the final equality is due to the complex conjugate of a standard result [25, p. 620] and the fact that the nth order cylindrical Bessel function of the first kind is real, where the standard result is

$$\exp(iz\sin\theta)=\sum_{n=-\infty}^{\infty}\exp(in\theta)J_n(z). \tag{4.9}$$

Alternative formulas are possible. In particular, if $\cos(\omega)=\cos(-\omega)$ is used between Eqs. 4.5 and 4.6 then the result is

$$\exp\left(-i2\pi\mathbf{k}^T\mathbf{x}\right)=\exp(-i2\pi z\zeta)\sum_{n=-\infty}^{\infty}\exp\left[-in\left(\frac{\pi}{2}+\varphi-\psi\right)\right]J_n(2\pi Rr) \tag{4.10}$$

which is the form that is used in the sequel.

Substitution of Eqs. 4.2 and 4.10 into Eq. 3.1 and performing the φ and z integrations leads to [7]

$$
\begin{aligned}
& F(R,\psi,\zeta) \\
= \;& \int_{r=0}^{\infty}\int_{\varphi=0}^{2\pi}\int_{z=-\infty}^{+\infty}\left[\sum_{l=-\infty}^{+\infty}\sum_{n=-\infty}^{+\infty}g_{n,l}(r)\exp\left[i\left(n\varphi+\frac{2\pi}{c}lz\right)\right]\right]\times \\
& \times\left[\exp\left(-i2\pi\zeta z\right)\sum_{n'=-\infty}^{+\infty}\exp(-in'(\varphi-\psi+\pi/2))J_{n'}(2\pi Rr)\right]\mathrm{d}z\mathrm{d}\varphi r\mathrm{d}r && (4.11) \\
= \;& \sum_{l=-\infty}^{+\infty}\sum_{n=-\infty}^{+\infty}\sum_{n'=-\infty}^{+\infty}\exp(-in'(-\psi+\pi/2))\left[\int_{r=0}^{\infty}g_{n,l}(r)J_{n'}(2\pi Rr)r\mathrm{d}r\right]\times
\end{aligned}
$$

$$\times \left[\int_{\varphi=0}^{2\pi} \exp(-in'\varphi)\exp\left(in\varphi\right)\mathrm{d}\varphi\right]\left[\int_{z=-\infty}^{+\infty} \exp\left(i\frac{2\pi}{c}lz\right)\exp\left(-i2\pi\zeta z\right)\mathrm{d}z\right] \tag{4.12}$$

$$= \sum_{l=-\infty}^{+\infty}\sum_{n=-\infty}^{+\infty}\sum_{n'=-\infty}^{+\infty} \exp(-in'(-\psi+\pi/2))\left[\int_{r=0}^{\infty} g_{n,l}(r)J_{n'}(2\pi Rr)r\mathrm{d}r\right]\times$$
$$\times \left[\int_{\varphi=0}^{2\pi}\exp\left(i(n-n')\varphi\right)\mathrm{d}\varphi\right]\left[\int_{z=-\infty}^{+\infty}\exp\left(i2\pi\left(\frac{l}{c}-\zeta\right)z\right)\mathrm{d}z\right] \tag{4.13}$$

$$= \sum_{l=-\infty}^{+\infty}\sum_{n=-\infty}^{+\infty}\sum_{n'=-\infty}^{+\infty} \exp(-in'(-\psi+\pi/2))\left[\int_{r=0}^{\infty} g_{n,l}(r)J_{n'}(2\pi Rr)r\mathrm{d}r\right]\times$$
$$\times 2\pi\delta_{n,n'}\delta\left(\zeta-\frac{l}{c}\right) \tag{4.14}$$

$$= \sum_{l=-\infty}^{+\infty}\sum_{n=-\infty}^{+\infty} \exp(-in(-\psi+\pi/2))\left[2\pi\int_{r=0}^{\infty} g_{n,l}(r)J_{n}(2\pi Rr)r\mathrm{d}r\right]\times$$
$$\times \delta\left(\zeta-\frac{l}{c}\right) \tag{4.15}$$

$$= \sum_{l=-\infty}^{+\infty}\left[\sum_{n=-\infty}^{+\infty} G_{n,l}(R)\exp(in(\psi-\pi/2))\right]\delta\left(\zeta-\frac{l}{c}\right) \tag{4.16}$$

where

$$G_{n,l}(R) = 2\pi\int_{r=0}^{\infty} g_{n,l}(r)J_n(2\pi Rr)r\mathrm{d}r \tag{4.17}$$

which is the cylindrical Hankel transform of order n of $g_{n,l}(r)$. Note that Eq. 4.16 is different from Ref. [7, Eq. 6] due to the sign convention in the Fourier transform, i.e., Eq. 3.1 has a minus sign in the exponent and Eq. 3.2 has a plus sign in the exponent. $F(R,\psi,\zeta)$ is non-zero only when ζ is an integer multiple of $1/c$ and these values of ζ are the so-called layer planes and are specified by the argument of the δ function in Eq. 4.16. Consider a particular layer plane with index $l = l_0$. Note that all terms in the sum

$$\sum_{n=-\infty}^{+\infty} G_{n,l_0}(R)\exp(in(\psi-\pi/2)) \tag{4.18}$$

contribute to the signal on the l_0th layer plane and do not contribute to the signal on any other layer plane. This fact is referred to as "Bessel function overlap".

Given only a single view, the Bessel terms on the same layer line cannot be separated [7], and various methods have been developed to deal with this problem by finding the correct orientation relationship among multiple views of the particles [16]. With multiple images, we are able to solve for $G_{n,l}(R)$ in a subspace defined by a collection of $H_{n,p}(R)$ functions.

4.2 Objects that have helical symmetry

Eqs. 4.2 and 4.16 describe objects that are periodic in z with period c. However, helical symmetry is more complicated. Let $u \in \mathcal{Z}^+$ be the number of subunits in one period (c) and $v \in \mathcal{Z}^+ \cup \{0\}$ be the number of turns in one period (c). (Standard terminology is that $p = c/v$ is the pitch and $\Delta z = c/u$ is the axial rise of the helix). Furthermore, a helix can be right or can be left handed. Note that $v = 0$ means that the symmetry of the helix is simply periodic with period c/u so results on periodic structures in the previous sections can be applied directly. For the case $v = 0$, it is not typical to refer to either right or left handedness.

There are several equivalent expressions for the helical symmetry. One expression for the symmetry of a right-handed helix is

$$\rho(r, \varphi, z) = \rho(r, \varphi + \frac{2\pi v}{u} m, z - \frac{c}{u} m) \tag{4.19}$$

for $m \in \mathcal{Z}$ and the corresponding expression for a left-handed helix is

$$\rho(r, \varphi, z) = \rho(r, \varphi - \frac{2\pi v}{u} m, z - \frac{c}{u} m) \tag{4.20}$$

for $m \in \mathcal{Z}$. If m is replaced by $-m$, which changes nothing since the equations are true for all $m \in \mathcal{Z}$, then a second expression for the symmetry of a right-handed

helix is

$$\rho(r,\varphi,z) = \rho(r,\varphi - \frac{2\pi v}{u}m, z + \frac{c}{u}m) \tag{4.21}$$

for $m \in \mathcal{Z}$ and the corresponding expression for a left-handed helix is

$$\rho(r,\varphi,z) = \rho(r,\varphi + \frac{2\pi v}{u}m, z + \frac{c}{u}m) \tag{4.22}$$

for $m \in \mathcal{Z}$.

Eqs. 4.19 and 4.20 or Eqs. 4.21 and 4.22 can be combined by allowing negative values of v. Allowing negative values of v leads to four equivalent expressions:

$$\rho(r,\varphi,z) = \rho(r,\varphi + \frac{2\pi v}{u}m, z - \frac{c}{u}m) \tag{4.23}$$

for $m \in \mathcal{Z}$ where $v > 0$ is right handed and $v < 0$ is left handed,

$$\rho(r,\varphi,z) = \rho(r,\varphi - \frac{2\pi v}{u}m, z - \frac{c}{u}m) \tag{4.24}$$

for $m \in \mathcal{Z}$ where $v > 0$ is left handed and $v < 0$ is right handed,

$$\rho(r,\varphi,z) = \rho(r,\varphi - \frac{2\pi v}{u}m, z + \frac{c}{u}m) \tag{4.25}$$

for $m \in \mathcal{Z}$ where $v > 0$ is right handed and $v < 0$ is left handed, or

$$\rho(r,\varphi,z) = \rho(r,\varphi + \frac{2\pi v}{u}m, z + \frac{c}{u}m) \tag{4.26}$$

for $m \in \mathcal{Z}$ where $v > 0$ is left handed and $v < 0$ is right handed.

The presence of a helical symmetry forces an infinite subset of the $G_{n,l}(R)$ functions (or equivalently, the $g_{n,l}(r)$ functions) to be identically zero. In order to derive this fact, return to Eq. 4.3. Note that

$$\int_{z=0}^{c} = \sum_{m=0}^{u-1} \int_{z=mc/u}^{(m+1)c/u} . \tag{4.27}$$

Use Eq. 4.27 in Eq. 4.3 to get

$$g_{n,l}(r) = \frac{1}{2\pi c} \sum_{m=0}^{u-1} \int_{z=mc/u}^{(m+1)c/u} \int_{\varphi=0}^{2\pi} \rho(r,\varphi,z) \exp\left[-i\left(n\varphi + \frac{2\pi}{c}lz\right)\right] \mathrm{d}\varphi \mathrm{d}z. \tag{4.28}$$

In the mth integral, change variables from z to $z' = z - mc/u$ to get

$$\begin{aligned} & g_{n,l}(r) \\ &= \frac{1}{2\pi c}\sum_{m=0}^{u-1}\int_{z'=0}^{c/u}\int_{\varphi=0}^{2\pi}\rho(r,\varphi,z'+mc/u)\exp\left[-i\left(n\varphi+\frac{2\pi}{c}l\left(z'+mc/u\right)\right)\right]\mathrm{d}\varphi\mathrm{d}z' \end{aligned} \tag{4.29}$$

$$\begin{aligned} &= \frac{1}{2\pi c}\sum_{m=0}^{u-1}\int_{z'=0}^{c/u}\int_{\varphi=0}^{2\pi}\rho\left(r,\left(\varphi+\frac{2\pi vm}{u}\right)-\frac{2\pi vm}{u},z'+\frac{mc}{u}\right)\times \\ &\quad\times\exp\left[-i\left(n\varphi+\frac{2\pi l}{c}z'+\frac{2\pi lm}{u}\right)\right]\mathrm{d}\varphi\mathrm{d}z'. \end{aligned} \tag{4.30}$$

Use Eq. 4.25 in the form

$$\rho(r,\varphi,z) = \rho(r,\varphi+\frac{2\pi v}{u}m, z-\frac{c}{u}m) \tag{4.31}$$

to get

$$\begin{aligned} & g_{n,l}(r) \\ &= \frac{1}{2\pi c}\sum_{m=0}^{u-1}\int_{z'=0}^{c/u}\int_{\varphi=0}^{2\pi}\rho\left(r,\varphi+\frac{2\pi vm}{u},z'\right)\exp\left[-i\left(n\varphi+\frac{2\pi l}{c}z'+\frac{2\pi lm}{u}\right)\right]\mathrm{d}\varphi\mathrm{d}z'. \end{aligned} \tag{4.32}$$

In the mth integral, change variables from φ to $\varphi' = \varphi + \frac{2\pi vm}{u}$ to get

$$\begin{aligned} & g_{n,l}(r) \\ &= \frac{1}{2\pi c}\sum_{m=0}^{u-1}\int_{z'=0}^{c/u}\int_{\varphi'=0}^{2\pi}\rho\left(r,\varphi',z'\right)\times \\ &\quad\times\exp\left[-i\left(n\left(\varphi'-\frac{2\pi vm}{u}\right)+\frac{2\pi l}{c}z'+\frac{2\pi lm}{u}\right)\right]\mathrm{d}\varphi'\mathrm{d}z' \end{aligned} \tag{4.33}$$

$$\begin{aligned} &= \frac{1}{2\pi c}\int_{z'=0}^{c/u}\int_{\varphi'=0}^{2\pi}\rho\left(r,\varphi',z'\right)\exp\left[-i\left(n\varphi'+\frac{2\pi l}{c}z'\right)\right]\mathrm{d}\varphi'\mathrm{d}z'\times \\ &\quad\left[\sum_{m=0}^{u-1}\exp\left[-i\left(-\frac{2\pi vnm}{u}+\frac{2\pi lm}{u}\right)\right]\right]\mathrm{d}\varphi'\mathrm{d}z' \end{aligned} \tag{4.34}$$

$$= \frac{1}{2\pi c}\int_{z'=0}^{c/u}\int_{\varphi'=0}^{2\pi}\rho\left(r,\varphi',z'\right)\times$$

$$\exp\left[-i\left(n\varphi' + \frac{2\pi l}{c}z'\right)\right]\mathrm{d}\varphi'\mathrm{d}z'\left[\sum_{m=0}^{u-1}\exp\left[i\frac{2\pi}{u}\left(vn-l\right)m\right]\right]\mathrm{d}\varphi'\mathrm{d}z'$$

. (4.35)

Since

$$\sum_{m=0}^{u-1}\alpha^m = \begin{cases} \frac{1-\alpha^u}{1-\alpha}, & \alpha \neq 1 \\ u, & \alpha = 1 \end{cases} \tag{4.36}$$

it follows that

$$\begin{aligned}
&\sum_{m=0}^{u-1}\exp\left[i\frac{2\pi}{u}\left(vn-l\right)m\right] \\
&= \begin{cases} \frac{1-\exp\left[i\frac{2\pi}{u}(vn-l)u\right]}{1-\exp\left[i\frac{2\pi}{u}(vn-l)\right]}, & \exp\left[i\frac{2\pi}{u}\left(vn-l\right)\right] \neq 1 \\ u, & \exp\left[i\frac{2\pi}{u}\left(vn-l\right)\right] = 1 \end{cases} && (4.37) \\
&= \begin{cases} \frac{1-\exp[i2\pi(vn-l)]}{1-\exp\left[i\frac{2\pi}{u}(vn-l)\right]}, & \exp\left[i\frac{2\pi}{u}\left(vn-l\right)\right] \neq 1 \\ u, & \frac{1}{u}\left(vn-l\right) = -j \text{ for some } j \in \mathcal{Z} \end{cases} && (4.38) \\
&= \begin{cases} 0, & \exp\left[i\frac{2\pi}{u}\left(vn-l\right)\right] \neq 1 \\ u, & vn + uj = l \text{ for some } j \in \mathcal{Z} \end{cases} && (4.39) \\
&= u\delta_{n,S_l} && (4.40)
\end{aligned}$$

where S_l is the set

$$S_l = \{n \in \mathcal{Z} : ju + nv = l \text{ for some } j \in \mathcal{Z}\}. \tag{4.41}$$

Therefore,

$$\begin{aligned}
&g_{n,l}(r) \\
&= \frac{u\delta_{n,S_l}}{2\pi c}\int_{z'=0}^{c/u}\int_{\varphi'=0}^{2\pi}\rho\left(r,\varphi',z'\right)\exp\left[-i\left(n\varphi' + \frac{2\pi l}{c}z'\right)\right]\mathrm{d}\varphi'\mathrm{d}z'
\end{aligned} \tag{4.42}$$

for all $n \in \mathcal{Z}$ and $l \in \mathcal{Z}$ which implies that for each layer plane (indexed by l), only certain Bessel orders are allowed, in particular, those Bessel orders n such that $n \in S_l$.

Table 4.1: Allowed pairs of l and n satisfying $0 \leq l \leq l_{\max}$ and $-n_{\max} \leq n \leq n_{\max}$ for $l_{\max} = 7$ and $n_{\max} = 49$ for a left-handed helix and for a right-handed helix where both helices have parameters $u = 49$ and $v = 3$.

left hand		right hand	
l	n	l	n
0	0	0	0
0	49	0	49
0	-49	0	-49
1	16	1	-16
1	-33	1	33
2	32	2	-32
2	-17	2	17
3	48	3	-48
3	-1	3	1
4	15	4	-15
4	-34	4	34
5	31	5	-31
5	-18	5	18
6	47	6	-47
6	-2	6	2
7	14	7	-14
7	-35	7	35

4.3 Properties of the helical selection rule

As is shown in Table 4.1 for the values of u and v that occur in Tobacco Mosaic Virus (TMV) (Chapter 12), the helical selection rule is a powerful aid to reconstruction since the large majority of (l, n) pairs are excluded and, furthermore, the values of l and n allowed by the selection rule differ if the helix is right- versus left-handed.

4.3.1 Solving the equation

The selection rule is defined by Eq. 4.41. The task is to determine all $n \in \mathcal{Z}$ such that

$$ju + nv = l \tag{4.43}$$

for some specific $l \in \mathcal{Z}$ and any $j \in \mathcal{Z}$. Eq. 4.43 is a linear Diophantine Equation [26, Section 2.5, p. 44]. The fundamental result for such equations is the following theorem.

Theorem 1 *Linear Diophantine Equations [26, Theorem 2.18, p. 44]. Suppose that $a, b \in \mathcal{Z}$ with $a \neq 0$ and $b \neq 0$ and d is the greatest common divisor of a and b. If d does not divide c then the equation*

$$ax + by = c \tag{4.44}$$

has no integral solutions for x and y. If d divides c then Eq. 4.44 has infinitely many solutions. If $x = x_0$ and $y = y_0$ is one integral solution to Eq. 4.44, then all integral solutions to Eq. 4.44 are given by

$$x = x_0 + t\frac{b}{d} \tag{4.45}$$

$$y = y_0 - t\frac{a}{d} \tag{4.46}$$

where $t \in \mathcal{Z}$.

In the helical problem, it is natural to assume that u and v have greatest common divisor of 1. Otherwise, let ξ be the greatest common divisor and then the helical symmetry (u, v, c) is the same as the helical symmetry $(u/\xi, v/\xi, c/\xi)$ where the second form is more fundamental since the period is shorter. Therefore, in all that follows, it is assumed that u and v are relatively prime. Then Theorem 1

guarantees an infinite set of (j, n) pairs that satisfy Eq. 4.43 for each value of l. This set must then be reorganized to find all pairs of (n, l) that satisfy Eq. 4.43 for some value of $j \in \mathcal{Z}$.

The values of n that satisfy the selection rule for fixed l, i.e., the set S_l (Eq. 4.41), are described in the following theorem.

Theorem 2 *Let $u \in \mathcal{Z}$ and $v \in \mathcal{Z}$ be relatively prime and fixed. Let $l \in \mathcal{Z}$ be fixed. Let $q \in \mathcal{Z}$ be such that*

$$qv \pmod{u} = +1. \tag{4.47}$$

Then the set N defined by

$$N = \{n \in \mathcal{Z} : ju + nv = l \text{ for some } j \in \mathcal{Z}\} \tag{4.48}$$

and the set N' defined by

$$N' = \{n \in \mathcal{Z} : n = ql + um \text{ for some } m \in \mathcal{Z}\} \tag{4.49}$$

are equal.

Proof: $ql \pmod{u} = q(ju + nv) \pmod{u}$ by Eq. 4.48. Furthermore, $q(ju + nv) = (qv)n \pmod{u}$ by the definition of equality mod u. In addition, $(qv)n \pmod{u} = n$ by the definition of q (Eq. 4.47). Therefore, it follows that $ql \pmod{u} = n$ which implies that $n = ql + um$ for some $m \in \mathcal{Z}$. $\diamond$

4.3.2 Properties of the selection rule equation

The selection rule has several important properties that can be exploited in order to reduce computation. Let $m \in \mathcal{Z}$.

1. If $l = 0$ then $n = mu$ is always a solution, since it results from choosing $j = 0$. $l = 0$ is the case where the helix does not have a handedness. $l = 0$ and $n = 0$ is the case where the object has a cylindrical symmetry, i.e., $\rho(r, \varphi, z)$ is a function of r alone.

2. Let $n = n^*$ be a solution for $l = l^*$. Then

   (a) $n = n^* + mu$ is also a solution for $l = l^*$.

   (b) $n' = mn^*$ is a solution for $l' = ml^*$.

For example,

$$1 = 49(-2) + 3(33) \tag{4.50}$$

$$33 \times 40 \pmod{49} = 46 \tag{4.51}$$

and therefore

$$40 = 49(-2) + 3(46) \tag{4.52}$$

is true. If one value of n is known for $l = 1$, then all other solutions are known for all l.

4.3.3 Left-handed versus right-handed selection rule

Let $l \in \mathcal{Z}$ be fixed. In both the right- and left-handed cases, the values of n are

$$\{n \in \mathcal{Z} : n = ql + um \text{ for some } m \in \mathcal{Z}\}. \tag{4.53}$$

However, the constraint satisfied by q is different in the right- versus left-handed cases. In particular, for the right-handed case, q must satisfy (Eq. 4.47)

$$qv \pmod{u} = +1 \tag{4.54}$$

while for the left-handed case, q must satisfy

$$qv \pmod{u} = u - 1. \tag{4.55}$$

The reason for the difference is that the left-handed rule is related to the right-handed rule by negating v.

4.4 The $g_{n,l}(r)$ and $G_{n,l}(R)$ functions for the case where the fundamental model for a helically-symmetric object is an impulsive atomic model

Suppose that the electron scattering intensity is impulsive, i.e.,

$$\rho(\mathbf{x}) = \sum_{j=1}^{N_j} f_j \delta(\mathbf{x} - \mathbf{x}_j) \tag{4.56}$$

or, in cylindrical coordinates,

$$\rho(r, \varphi', z') = \sum_{j=1}^{N_j} f_j \delta(z - z_j)\delta(\varphi - \varphi_j)\delta(r - r_j)/r, \tag{4.57}$$

where the N_j impulses represent one asymmetric unit of the helical symmetry, e.g., the N_j impulses are all located in the region $0 \le z \le c/u$ and $0 \le \varphi \le 2\pi$. Then (Eq. 4.42),

$$\begin{aligned} & g_{n,l}(r) \\ &= \frac{u\delta_{n,S_l}}{2\pi c} \int_{z=0}^{c/u} \int_{\varphi=0}^{2\pi} \left[\sum_{j=1}^{N_j} f_j \delta(z - z_j)\delta(\varphi - \varphi_j)\delta(r - r_j)/r \right] \times \\ &\quad \times \exp\left[-i \left(n\varphi + \frac{2\pi l}{c} z \right) \right] \mathrm{d}\varphi \mathrm{d}z \end{aligned} \tag{4.58}$$

$$= \frac{u\delta_{n,S_l}}{2\pi c r} \sum_{j=1}^{N_j} f_j \delta(r - r_j) \exp\left[-i \left(n\varphi_j + \frac{2\pi l}{c} z_j \right) \right] \tag{4.59}$$

for all $n \in \mathcal{Z}$ and $l \in \mathcal{Z}$. Therefore (Eq. 4.17),

$$G_{n,l}(R) = 2\pi \int_{r=0}^{\infty} \left[\frac{u\delta_{n,S_l}}{2\pi c r} \sum_{j=1}^{N_j} f_j \delta(r - r_j) \exp\left[-i \left(n\varphi_j + \frac{2\pi l}{c} z_j \right) \right] \right] J_n(2\pi R r) r \mathrm{d}r \tag{4.60}$$

$$= 2\pi \frac{u\delta_{n,S_l}}{2\pi c} \sum_{j=1}^{N_j} f_j \exp\left[-i \left(n\varphi_j + \frac{2\pi l}{c} z_j \right) \right] J_n(2\pi R r_j). \tag{4.61}$$

Using Eq. 4.61 in Eq. 4.16 provides an expression for the 3-D Fourier transform $F(R, \psi, \zeta)$ in terms of the atomic locations (r_j, φ_j, z_j) and scattering strengths f_j:

$$\begin{aligned} & F(R, \psi, \zeta) \\ &= \sum_{l=-\infty}^{+\infty} \left[\sum_{n=-\infty}^{+\infty} \left[2\pi \frac{u\delta_{n,S_l}}{2\pi c} \sum_{j=1}^{N_j} f_j \exp\left[-i \left(n\varphi_j + \frac{2\pi l}{c} z_j \right) \right] J_n(2\pi R r_j) \right] \exp(in(\psi - \pi/2)) \right] \times \\ &\quad \times \delta\left(\zeta - \frac{l}{c} \right) \end{aligned} \tag{4.62}$$

$$= \sum_{l=-\infty}^{+\infty} \left[\sum_{n=-\infty}^{+\infty} \frac{u\delta_{n,S_l}}{c} \sum_{j=1}^{N_j} f_j J_n(2\pi R r_j) \exp\left[i \left(n(\psi - \pi/2 - \varphi_j) - \frac{2\pi l}{c} z_j \right) \right] \right] \delta\left(\zeta - \frac{l}{c} \right) \tag{4.63}$$

.

where l^{th} layer plane in Eq. 4.63 is the $-l^{th}$ layer plane in the Ref. [7, Eq. 8].

4.5 Objects with further symmetries

4.5.1 C_μ symmetry

In addition to helical symmetry, C_μ symmetry may be present. Such symmetry implies

$$\rho(r, \varphi, z) = \rho\left(r, \varphi + \frac{2\pi}{\mu} m, z \right) \tag{4.64}$$

for all $m \in \mathcal{Z}$. Therefore, this symmetry concerns only the φ variable.

Any square-integrable function $f(\varphi)$ that is periodic with period 2π has a Fourier series

$$f(\varphi) = \sum_{n=-\infty}^{+\infty} f_n \exp(in\varphi) \tag{4.65}$$

$$f_n = \frac{1}{2\pi}\int_{\varphi=0}^{2\pi} f(\varphi)\exp(-in\varphi)\mathrm{d}\varphi. \tag{4.66}$$

In terms of the Fourier series coefficients f_n,

$$f(\varphi) = f\left(\varphi + \frac{2\pi}{\mu}m\right) \tag{4.67}$$

for all $m \in \mathcal{Z}$ if and only if $n \neq \mu m$ $(m \in \mathcal{Z})$ implies $f_n = 0$.

Define the set

$$S_\mu^C = \{\mu m : m \in \mathcal{Z}\}. \tag{4.68}$$

Then the result of the previous paragraph, combined with Eq. 4.42, implies that

$$g_{n,l}(r) = \frac{u\delta_{n,S_l}\delta_{n,S_\mu^C}}{2\pi c}\int_{z'=0}^{c/u}\int_{\varphi'=0}^{2\pi}\rho\left(r,\varphi',z'\right)\exp\left[-i\left(n\varphi' + \frac{2\pi l}{c}z'\right)\right]\mathrm{d}\varphi'\mathrm{d}z' \tag{4.69}$$

for all $n \in \mathcal{Z}$ and $l \in \mathcal{Z}$ which reduces the number of Bessel orders allowed on any particular layer plane.

4.5.2 D_μ symmetry

In addition to helical symmetry, D_μ symmetry may be present. Such symmetry implies C_μ symmetry plus the additional symmetry

$$\rho(r,\varphi,z) = \rho(r,\varphi,-z). \tag{4.70}$$

Therefore, relative to helical plus C_μ symmetry, the additional symmetry concerns only the z variable.

Any square-integrable function $f(z)$ that is periodic with period c has a Fourier series

$$f(z) = \sum_{n=-\infty}^{+\infty} f_n \exp\left(i\frac{2\pi}{c}nz\right) \tag{4.71}$$

$$f_n = \frac{1}{c}\int_{z=0}^{c} f(z)\exp\left(-i\frac{2\pi}{c}nz\right)\mathrm{d}z. \tag{4.72}$$

In terms of the Fourier series coefficients f_n,

$$f(z) = f(-z) \tag{4.73}$$

if and only if $f_n = f_{-n}$ for all $n \in \mathcal{Z}$ since

$$f_n = \frac{1}{c}\int_{z=0}^{c} f(z)\exp\left(-i\frac{2\pi}{c}nz\right)\mathrm{d}z \tag{4.74}$$

change variables from z to $z' = -z$ to get

$$= \frac{1}{c}\int_{z'=-c}^{0} f(-z')\exp\left(-i\frac{2\pi}{c}n(-z')\right)\mathrm{d}z' \tag{4.75}$$

since the integrand is period with period c, any region of integration of duration c is equivalent and so

$$= \frac{1}{c}\int_{z'=0}^{c} f(-z')\exp\left(-i\frac{2\pi}{c}n(-z')\right)\mathrm{d}z' \tag{4.76}$$

which, by applying the symmetry, is equivalent to

$$= \frac{1}{c}\int_{z'=0}^{c} f(z')\exp\left(-i\frac{2\pi}{c}(-n)z'\right)\mathrm{d}z' \tag{4.77}$$

$$= f_{-n}. \tag{4.78}$$

Therefore, there is an additional constraint on the $g_{n,l}(r)$ functions, in particular, based on Eq. 4.69,

$$g_{n,-l}(r) = g_{n,l}(r) \tag{4.79}$$

$$= \frac{u\delta_{n,S_l}\delta_{n,S_\mu^C}}{2\pi c}\int_{z'=0}^{c/u}\int_{\varphi'=0}^{2\pi}\rho\left(r,\varphi',z'\right)\exp\left[-i\left(n\varphi'+\frac{2\pi l}{c}z'\right)\right]\mathrm{d}\varphi'\mathrm{d}z' \tag{4.80}$$

for all $n \in \mathcal{Z}$ and $l \in \mathcal{Z}^+ \cup \{0\}$ which constrains the $+l$ and $-l$ layer planes to share the same $g_{n,l}(r)$ (or, equivalently, $G_{n,l}(R)$) functions.

4.5.3 $\rho(\mathbf{x})$ is real valued

If $\rho(\mathbf{x}) \in \mathbb{R}$ then there is a further constraint on the $g_{n,l}(r)$ (or, equivalently, $G_{n,l}(R)$) functions.

The most elementary implication of $\rho(\mathbf{x}) \in \mathbb{R}$ is that $F(\mathbf{k}=\mathbf{0}) \in \mathbb{R}$ since $F(\mathbf{k})$ is the 3-D Fourier transform of $\rho(\mathbf{x})$. This result follows immediately from the definition of the Fourier transform evaluated at $\mathbf{k}=\mathbf{0}$, i.e., Eq. 3.1 evaluated at $\mathbf{k}=\mathbf{0}$. Evaluating $F(\mathbf{k}=\mathbf{0})$ via Eq. 4.16 implies evaluating Eq. 4.16 at $R=0$ and $\zeta=0$ for arbitrary value of ψ. The result is

$$F(R=0,\psi,\zeta=0)=\sum_{l=-\infty}^{+\infty}\left[\sum_{n=-\infty}^{+\infty}G_{n,l}(0)\exp(in(\psi-\pi/2))\right]\delta\left(-\frac{l}{c}\right). \tag{4.81}$$

Because the δ function is nonzero only for $l=0$ it follows that the only nonzero contribution is

$$F(R=0,\psi,\zeta=0)=\left[\sum_{n=-\infty}^{+\infty}G_{n,0}(0)\exp(in(\psi-\pi/2))\right]\delta\left(0\right). \tag{4.82}$$

From the definition of $G_{n,l}(R)$ (Eq. 4.17) it follows that

$$G_{n,0}(0)=2\pi\int_{r=0}^{\infty}g_{n,0}(r)J_n(0)r\mathrm{d}r. \tag{4.83}$$

Because $J_n(0)=0$ for all $n \in \{\pm1,\pm2,\ldots\}$ it follows that the only nonzero $G_{n,0}(0)$ is for $n=0$ which implies that

$$F(R=0,\psi,\zeta=0)=G_{0,0}(0)\delta\left(0\right) \tag{4.84}$$

so that $F(\mathbf{k}=\mathbf{0})$ is completely determined by $G_{0,0}(0)$. This implies that $G_{0,0}(0) \in \mathbb{R}$ for $\rho(\mathbf{x}) \in \mathbb{R}$. But more is true, in particular, the definition of $g_{n,l}(r)$ (Eq. 4.3) evaluated at $n = l = 0$ gives

$$g_{0,0}(r) = \frac{1}{2\pi c} \int_{z=0}^{c} \int_{\varphi=0}^{2\pi} \rho(r,\varphi,z) \mathrm{d}\varphi \mathrm{d}z \tag{4.85}$$

so $\rho(\mathbf{x}) \in \mathbb{R}$ implies $g_{0,0}(r) \in \mathbb{R}$ which implies $G_{0,0}(R) \in \mathbb{R}$ since $J_0(\cdot) \in \mathbb{R}$. Therefore, for $\rho(\mathbf{x}) \in \mathbb{R}$, $G_{0,0}(R) \in \mathbb{R}$ for all R, not just $R = 0$.

More generally, take the complex conjugate of Eq. 4.3 to get

$$\begin{aligned}
[g_{n,l}(r)]^* &= \left[\frac{1}{2\pi c} \int_{z=0}^{c} \int_{\varphi=0}^{2\pi} \rho(r,\varphi,z) \exp\left[-i\left(n\varphi + \frac{2\pi}{c} lz\right)\right] \mathrm{d}\varphi \mathrm{d}z\right]^* && (4.86)\\
&= \frac{1}{2\pi c} \int_{z=0}^{c} \int_{\varphi=0}^{2\pi} \left[\rho(r,\varphi,z) \exp\left[-i\left(n\varphi + \frac{2\pi}{c} lz\right)\right]\right]^* \mathrm{d}\varphi \mathrm{d}z && (4.87)\\
&\quad \text{which, since } \rho^*(\mathbf{x}) = \rho(\mathbf{x}), \text{ implies that}\\
&= \frac{1}{2\pi c} \int_{z=0}^{c} \int_{\varphi=0}^{2\pi} \rho(r,\varphi,z) \left[\exp\left[-i\left(n\varphi + \frac{2\pi}{c} lz\right)\right]\right]^* \mathrm{d}\varphi \mathrm{d}z && (4.88)\\
&= \frac{1}{2\pi c} \int_{z=0}^{c} \int_{\varphi=0}^{2\pi} \rho(r,\varphi,z) \exp\left[-i\left((-n)\varphi + \frac{2\pi}{c}(-l)z\right)\right] \mathrm{d}\varphi \mathrm{d}z && (4.89)\\
&= g_{-n,-l}(r) && (4.90)
\end{aligned}$$

for all $n \in \mathcal{Z}$ and $l \in \mathcal{Z}$. Eq. 4.90 implies that

$$g_{0,0}(r) \in \mathbb{R} \tag{4.91}$$

which in turn implies that

$$G_{0,0}(R) \in \mathbb{R} \tag{4.92}$$

since $J_n(\cdot) \in \mathbb{R}$ in Eq. 4.17. More generally, Eq. 4.90 implies that there is an additional constraint on the $g_{n,l}(r)$ functions, specifically,

$$\begin{aligned}
& g^*_{-n,-l}(r)\\
&= g_{n,l}(r) && (4.93)\\
&= \frac{u\delta_{n,S_l}}{2\pi c} \int_{z'=0}^{c/u} \int_{\varphi'=0}^{2\pi} \rho\left(r,\varphi',z'\right) \exp\left[-i\left(n\varphi' + \frac{2\pi l}{c} z'\right)\right] \mathrm{d}\varphi' \mathrm{d}z' && (4.94)
\end{aligned}$$

for all $n \in \mathcal{Z}$ and $l \in \mathcal{Z}^+ \cup \{0\}$ which constrains the $+l$ and $-l$ layer planes to have complex-conjugate pairs of $g_{n,l}(r)$ (or, equivalently, $G_{n,l}(R)$) functions.

If $\rho(\mathbf{x}) \in \mathbb{R}$ is combined with C_μ symmetry then

$$\begin{aligned} & g^*_{-n,-l}(r) \\ &= g_{n,l}(r) \qquad (4.95) \\ &= \frac{u\delta_{n,S_l}\delta_{n,S^C_\mu}}{2\pi c}\int_{z'=0}^{c/u}\int_{\varphi'=0}^{2\pi}\rho\left(r,\varphi',z'\right)\exp\left[-i\left(n\varphi'+\frac{2\pi l}{c}z'\right)\right]\mathrm{d}\varphi'\mathrm{d}z' \qquad (4.96) \end{aligned}$$

for all $n \in \mathcal{Z}$ and $l \in \mathcal{Z}^+ \cup \{0\}$ which constrains the $+l$ and $-l$ layer planes to have complex-conjugate pairs of $g_{n,l}(r)$ (or, equivalently, $G_{n,l}(R)$) functions and further restricts the number of nonzero Bessel orders that are permitted by the δ_{n,S^C_μ} factor. If $\rho(\mathbf{x}) \in \mathbb{R}$ is combined with D_μ symmetry then $g^*_{-n,-l}(r) = g_{n,l}(r)$ and $g_{n,-l}(r) = g_{n,l}(r)$ which implies

$$\begin{aligned} & g^*_{-n,-l}(r) \\ &= g_{n,-l}(r) \qquad (4.97) \\ &= g_{n,l}(r) \qquad (4.98) \\ &= \frac{u\delta_{n,S_l}\delta_{n,S^C_\mu}}{2\pi c}\int_{z'=0}^{c/u}\int_{\varphi'=0}^{2\pi}\rho\left(r,\varphi',z'\right)\exp\left[-i\left(n\varphi'+\frac{2\pi l}{c}z'\right)\right]\mathrm{d}\varphi'\mathrm{d}z' \qquad (4.99) \end{aligned}$$

for all $n \in \mathcal{Z}$ and $l \in \mathcal{Z}^+ \cup \{0\}$ which constrains the $+l$ and $-l$ layer planes to have complex-conjugate pairs of $g_{n,l}(r)$ functions, constrains the $g_{n,l}(r)$ functions on a single layer plane such that $g_{n,l}(r) = g^*_{-n,l}(r)$, and further restricts the number of nonzero Bessel orders that are permitted by the δ_{n,S^C_μ} factor.

In terms of $F(R,\psi,\zeta)$, the constraint $\rho(\mathbf{x}) \in \mathbb{R}$ implies $F(\mathbf{k}) = F^*(-\mathbf{k})$ which implies $F(R,\psi,\zeta) = F^*(R,\psi+\pi,-\zeta)$.

CHAPTER 5

MATHEMATICAL MODEL OF THE IMAGE FORMATION PROCESS

5.1 Images of infinite extent

The image formation model includes the orientation (rotation and translation) of the object in the microscope, the 2-D projection of the 3-D object, and the convolution of the 2-D projection with the so-called contrast transfer function (CTF) [27] of the microscope to include the electron-optical effects of the microscope. Let $\rho(\mathbf{x})$ (with 3-D Fourier transform $F(\mathbf{k})$) be the electron scattering function of the object in the natural coordinates of the object, e.g., the coordinates where z is the axis of the helix. Let $\rho'(\mathbf{x})$ (with 3-D Fourier transform $F'(\mathbf{k})$) be the electron scattering function of the object after it is rotated to the orientation it has in the microscope where the rotation is described by Euler angles (α, β, γ). Then

$$\rho'(\mathbf{x}) = \rho(R^{-1}(\alpha, \beta, \gamma)\mathbf{x}) \tag{5.1}$$

which implies that

$$F'(\mathbf{k}) = F(R^{-1}(\alpha, \beta, \gamma)\mathbf{k}). \tag{5.2}$$

Let $\rho''(\mathbf{x})$ (with 3-D Fourier transform $F''(\mathbf{k})$) be the electron scattering function of the object after it is both rotated and translated so that it is in its final position in the microscope. Then

$$\rho''(\mathbf{x}) = \rho'(\mathbf{x} - \mathbf{x}_0) = \rho(R^{-1}(\alpha, \beta, \gamma)(\mathbf{x} - \mathbf{x}_0)) \tag{5.3}$$

which implies that

$$F''(\mathbf{k}) = \exp(-i2\pi\mathbf{k}^T\mathbf{x}_0)F'(\mathbf{k}) = \exp(-i2\pi\mathbf{k}^T\mathbf{x}_0)F(R^{-1}(\alpha, \beta, \gamma)\mathbf{k}). \tag{5.4}$$

The coordinate system in the microscope is chosen so that the 2-D projection is always in the z direction. Note that this is the coordinate system in the microscope, not the coordinate system for describing the object. The object coordinate system is related to the microscope coordinate system by the rotation described by Euler angles (α, β, γ) and, typically, β is near $\pi/2$ so that the long axis of the helix lies nearly flat on the stage of the microscope. Let $\sigma'(\boldsymbol{\chi})$ be the resulting 2-D projection image with 2-D Fourier transform denoted by $\Sigma'(\boldsymbol{\kappa})$. Therefore, by the projection-slice theorem [28, 29],

$$\Sigma'(\boldsymbol{\kappa}) = F''((\boldsymbol{\kappa}^T, 0)^T), \tag{5.5}$$

i.e., $F''(\mathbf{k})$ evaluated at the 3-D $\mathbf{k}$ vector whose first two components are $\boldsymbol{\kappa}$ and whose third component is 0. Therefore,

$$\begin{aligned} \Sigma'(\boldsymbol{\kappa}) &= \exp(-i2\pi(\boldsymbol{\kappa}^T, 0)\mathbf{x}_0) F(R^{-1}(\alpha, \beta, \gamma)(\boldsymbol{\kappa}^T, 0)^T) & (5.6) \\ &= \exp(-i2\pi\boldsymbol{\kappa}^T\boldsymbol{\chi}_0) F(R^{-1}(\alpha, \beta, \gamma)(\boldsymbol{\kappa}^T, 0)^T) & (5.7) \end{aligned}$$

where $\boldsymbol{\chi}_0 \in \mathbb{R}^2$ is the first two components of $\mathbf{x}_0 \in \mathbb{R}^3$. Finally, let $\sigma(\boldsymbol{\chi})$ be the ideal (i.e., uncorrupted and infinite in extent) image with 2-D Fourier transform $\Sigma(\boldsymbol{\kappa})$. Then

$$\Sigma(\boldsymbol{\kappa}) = C(|\boldsymbol{\kappa}|)\Sigma'(\boldsymbol{\kappa}) = C(|\boldsymbol{\kappa}|)\exp(-i2\pi\boldsymbol{\kappa}^T\boldsymbol{\chi}_0) F(R^{-1}(\alpha, \beta, \gamma)(\boldsymbol{\kappa}^T, 0)^T) \tag{5.8}$$

where $C(\cdot)$ is the CTF.

In order to derive an explicit formula combining Eqs. 4.16 and 5.8, it is necessary to determine the cylindrical coordinates of the 3-D vector $R^{-1}(\alpha, \beta, \gamma)(\boldsymbol{\kappa}^T, 0)^T$ as a function of $\boldsymbol{\kappa} = (\kappa_1, \kappa_2)^T$ and (α, β, γ). As is indicated in Table 3.2, these coordinates are denoted by

$$\mathbf{k}'_L = R^{-1}(\alpha, \beta, \gamma)(\kappa_1, \kappa_2, 0)^T = (k'_{L_1}, k'_{L_2}, k'_{L_3})^T = (R'_L, \psi'_L, \zeta'_L) \tag{5.9}$$

which depends on the details of $R_L(\alpha, \beta, \gamma)$.

For general $\mathbf{k}$,

$$\begin{bmatrix} k_{L_1} \\ k_{L_2} \\ k_{L_3} \end{bmatrix} = R^{-1}\mathbf{k} \tag{5.10}$$

$$= \begin{bmatrix} k_1(\cos\alpha\cos\beta\cos\gamma - \sin\alpha\sin\gamma) - k_2(\cos\alpha\cos\beta\sin\gamma + \sin\alpha\cos\gamma) + k_3\cos\alpha\sin\beta \\ k_1(\sin\alpha\cos\beta\cos\gamma + \cos\alpha\sin\gamma) + k_2(-\sin\alpha\cos\beta\sin\gamma + \cos\alpha\cos\gamma) + k_3\sin\alpha\sin\beta \\ -k_1\sin\beta\cos\gamma + k_2\sin\beta\sin\gamma + k_3\cos\beta \end{bmatrix}. \tag{5.11}$$

Converting to cylindrical coordinates gives

$$R_L = \sqrt{k_{L_1}^2 + k_{L_2}^2} \tag{5.12}$$

$$\psi_L = \arctan(k_{L_2}/k_{L_1}) \tag{5.13}$$

$$\zeta_L = k_{L_3} \tag{5.14}$$

$$= -k_1\sin\beta\cos\gamma + k_2\sin\beta\sin\gamma + k_3\cos\beta. \tag{5.15}$$

Because (α, β, γ) represent a rotation, it follows that $R^{-1}(\alpha, \beta, \gamma)$ is an orthogonal matrix and therefore

$$|\mathbf{k}_L| = |\mathbf{k}| \tag{5.16}$$

but the length of the 3-D vector is not one of the coordinates in cylindrical coordinates. For the case when $\mathbf{k} = (\boldsymbol{\kappa}^T, 0)^T$, which is needed in Eq. 5.8, the formulas simplify:

$$R'_L = \sqrt{k'^2_{L_1} + k'^2_{L_2}} \tag{5.17}$$

$$= \begin{bmatrix} [\kappa_1(\cos\alpha\cos\beta\cos\gamma - \sin\alpha\sin\gamma) - \kappa_2(\cos\alpha\cos\beta\sin\gamma + \sin\alpha\cos\gamma)]^2 \\ + [\kappa_1(\sin\alpha\cos\beta\cos\gamma + \cos\alpha\sin\gamma) + \kappa_2(-\sin\alpha\cos\beta\sin\gamma + \cos\alpha\cos\gamma)]^2 \end{bmatrix}^{1/2}$$

(5.18)

$$= \left[\begin{array}{c} \kappa_1^2 \left[(\cos\alpha\cos\beta\cos\gamma - \sin\alpha\sin\gamma)^2 + (\sin\alpha\cos\beta\cos\gamma + \cos\alpha\sin\gamma)^2 \right] \\ +\kappa_2^2 \left[(\cos\alpha\cos\beta\sin\gamma + \sin\alpha\cos\gamma)^2 + (-\sin\alpha\cos\beta\sin\gamma + \cos\alpha\cos\gamma)^2 \right] \\ +\kappa_1\kappa_2[-2(\cos\alpha\cos\beta\cos\gamma - \sin\alpha\sin\gamma)(\cos\alpha\cos\beta\sin\gamma + \sin\alpha\cos\gamma) \\ +2(\sin\alpha\cos\beta\cos\gamma + \cos\alpha\sin\gamma)(-\sin\alpha\cos\beta\sin\gamma + \cos\alpha\cos\gamma)] \end{array} \right]^{1/2}$$

(5.19)

$$= \left[\begin{array}{c} \kappa_1^2[\cos^2\alpha\cos^2\beta\cos^2\gamma + \sin^2\alpha\sin^2\gamma - 2\cos\alpha\cos\beta\cos\gamma\sin\alpha\sin\gamma \\ +\sin^2\alpha\cos^2\beta\cos^2\gamma + \cos^2\alpha\sin^2\gamma + 2\sin\alpha\cos\beta\cos\gamma\cos\alpha\sin\gamma] \\ +\kappa_2^2[\cos^2\alpha\cos^2\beta\sin^2\gamma + \sin^2\alpha\cos^2\gamma + 2\cos\alpha\cos\beta\sin\gamma\sin\alpha\cos\gamma \\ +\sin^2\alpha\cos^2\beta\sin^2\gamma + \cos^2\alpha\cos^2\gamma - 2\sin\alpha\cos\beta\sin\gamma\cos\alpha\cos\gamma] \\ +\kappa_1\kappa_2 2[-\cos^2\alpha\cos^2\beta\sin\gamma\cos\gamma - \sin\alpha\cos\alpha\cos\beta\cos^2\gamma \\ +\sin\alpha\cos\alpha\cos\beta\sin^2\gamma + \sin^2\alpha\sin\gamma\cos\gamma \\ -\sin^2\alpha\cos^2\beta\sin\gamma\cos\gamma + \sin\alpha\cos\alpha\cos\beta\cos^2\gamma \\ -\sin\alpha\cos\alpha\cos\beta\sin^2\gamma + \cos^2\alpha\sin\gamma\cos\gamma] \end{array} \right]^{1/2}$$

(5.20)

$$= \left[\begin{array}{c} \kappa_1^2 \left[\cos^2\beta\cos^2\gamma + \sin^2\gamma \right] \\ +\kappa_2^2 \left[\cos^2\beta\sin^2\gamma + \cos^2\gamma \right] \\ +\kappa_1\kappa_2 2[-\cos^2\beta\sin\gamma\cos\gamma + \sin\gamma\cos\gamma] \end{array} \right]^{1/2} \tag{5.21}$$

$$= \left[\begin{array}{c} \kappa_1^2 \left(\cos^2\beta\cos^2\gamma + \sin^2\gamma \right) + \kappa_2^2 \left(\cos^2\beta\sin^2\gamma + \cos^2\gamma \right) \\ +\kappa_1\kappa_2 2\sin^2\beta\sin\gamma\cos\gamma \end{array} \right]^{1/2} \tag{5.22}$$

$$\psi'_L = \arctan(k'_{L_2}/k'_{L_1}) \tag{5.23}$$

$$= \arctan\left[\frac{\kappa_1(\sin\alpha\cos\beta\cos\gamma + \cos\alpha\sin\gamma) + \kappa_2(-\sin\alpha\cos\beta\sin\gamma + \cos\alpha\cos\gamma)}{\kappa_1(\cos\alpha\cos\beta\cos\gamma - \sin\alpha\sin\gamma) - \kappa_2(\cos\alpha\cos\beta\sin\gamma + \sin\alpha\cos\gamma)} \right] \tag{5.24}$$

$$\zeta'_L = k'_{L_3} \tag{5.25}$$

$$= -\kappa_1\sin\beta\cos\gamma + \kappa_2\sin\beta\sin\gamma. \tag{5.26}$$

Note from Eq. 5.22 that R'_L is not a function of α. Furthermore, if $\gamma = 0$ (please see Section 5.2), then

$$R'_L = \sqrt{\kappa_1^2\cos^2\beta + \kappa_2^2} \tag{5.27}$$

$$\psi'_L = \arctan\left[\frac{\kappa_1\sin\alpha\cos\beta + \kappa_2\cos\alpha}{\kappa_1\cos\alpha\cos\beta - \kappa_2\sin\alpha} \right]. \tag{5.28}$$

Consider the δ function in Eq. 4.16:

$$\begin{aligned}
\delta\left(\zeta'_L - \frac{l}{c}\right) &= \delta\left(-\kappa_1 \sin\beta\cos\gamma + \kappa_2 \sin\beta\sin\gamma - \frac{l}{c}\right) && (5.29)\\
&= \delta\left(-\sin\beta\cos\gamma\left[\kappa_1 - \kappa_2\tan\gamma + \frac{l}{c\sin\beta\cos\gamma}\right]\right) && (5.30)\\
&= \frac{1}{|-\sin\beta\cos\gamma|}\delta\left(\kappa_1 - \kappa_2\tan\gamma + \frac{l}{c\sin\beta\cos\gamma}\right) && (5.31)\\
&= \frac{1}{|\sin\beta\cos\gamma|}\delta\left(\kappa_1 - \kappa_2\tan\gamma + \frac{l}{c\sin\beta\cos\gamma}\right) && (5.32)
\end{aligned}$$

since $\delta(at) = (1/|a|)\delta(t)$. Note that the Euler angle β satisfies $0 \leq \beta \leq \pi$ so that $\sin\beta \geq 0$ always. However, the Euler angle γ satisfies $0 \leq \gamma < 2\pi$ so that $\cos\gamma$ can take either sign and therefore the absolute value signs are necessary. Using Eq. 5.32 in Eq. 4.16 and the result in Eq. 5.8 implies that

$$\begin{aligned}
\Sigma(\boldsymbol{\kappa}) &= \frac{1}{|\sin\beta\cos\gamma|}C(|\boldsymbol{\kappa}|)\exp(-i2\pi\boldsymbol{\kappa}^T\boldsymbol{\chi}_0)\sum_{l=-\infty}^{+\infty}\left[\sum_{n=-\infty}^{+\infty}G_{n,l}(R'_L)\exp(in(\psi'_L - \pi/2))\right]\times\\
&\quad\times\delta\left(\kappa_1 - \kappa_2\tan\gamma + \frac{l}{c\sin\beta\cos\gamma}\right) && (5.33)
\end{aligned}$$

for structures with no symmetry and

$$\begin{aligned}
\Sigma(\boldsymbol{\kappa}) &= \frac{1}{|\sin\beta\cos\gamma|}C(|\boldsymbol{\kappa}|)\exp(-i2\pi\boldsymbol{\kappa}^T\boldsymbol{\chi}_0)\sum_{l=-\infty}^{+\infty}\left[\sum_{n=-\infty}^{+\infty}\delta_{n,S_l}G_{n,l}(R'_L)\exp(in(\psi'_L - \pi/2))\right]\times\\
&\quad\times\delta\left(\kappa_1 - \kappa_2\tan\gamma + \frac{l}{c\sin\beta\cos\gamma}\right) && (5.34)
\end{aligned}$$

for objects with helical symmetry where R'_L and ψ'_L are defined as functions of κ_1, κ_2, α, β, and γ by Eqs. 5.22 and 5.24, respectively. For an impulsive electron scattering intensity, use of Eq. 4.61 in Eq. 5.34 or, equivalently, use of Eq. 5.32 in Eq. 4.63 followed by using the result in Eq. 5.8, provides a formula for the 2-D Fourier transform $\Sigma(\boldsymbol{\kappa})$ of the image in terms of the atomic locations (r_j, φ_j, z_j) and scattering strengths f_j for a helical object,

$$\begin{aligned}
\Sigma(\boldsymbol{\kappa}) &= \frac{1}{|\sin\beta\cos\gamma|}C(|\boldsymbol{\kappa}|)\exp(-i2\pi\boldsymbol{\kappa}^T\boldsymbol{\chi}_0)\times\\
&\quad\times\sum_{l=-\infty}^{+\infty}\left[\sum_{n=-\infty}^{+\infty}\frac{u\delta_{n,S_l}}{c}\sum_{j=1}^{N_j}f_j J_n(2\pi R'_L r_j)\exp\left[i\left(n(\psi'_L - \pi/2 - \varphi_j) - \frac{2\pi l}{c}z_j\right)\right]\right]\times\\
&\quad\times\delta\left(\kappa_1 - \kappa_2\tan\gamma + \frac{l}{c\sin\beta\cos\gamma}\right), && (5.35)
\end{aligned}$$

where R'_L and ψ'_L are defined as functions of κ_1, κ_2, α, β, and γ by Eqs. 5.22 and 5.24, respectively.

5.2 Windowed images [1, 2, 3]

The real-space 3-D cube (2-D image) for an ideal helix is periodic along the axis of the helix and, correspondingly, the reciprocal-space 3-D cube (2-D image) has layer planes or layer lines represented by, for example, the δ functions of Eq. 4.16 (Eqs. 5.33–5.35). While the electron micrograph will show the entire width of the helix, it will not, of course, show the entire infinite length of the helix and therefore it is inevitable that processing must be based on windowed images. In addition to being realistic, windowing provides the computational advantage that the impulsive layer line is broadened to a smooth function that can be represented numerically. Because the electron micrograph shows the entire width of the helix but only a part of its length, the window that is used in this document is infinite in the width direction but finite in the length direction. The use of infinite width simplifies the mathematics, as will be shown in the sequel, because it leads to a δ function in κ_2.

Let $\mu(\boldsymbol{\chi})$ and $M(\boldsymbol{\kappa})$ denote the real-space and reciprocal-space representations of the window, respectively. Define $\mu(\boldsymbol{\chi})$ by

$$\mu(\boldsymbol{\chi}) = \begin{cases} 1 & |\chi_1| \leq w/2 \\ 0 & \text{otherwise} \end{cases} \tag{5.36}$$

where w is the width of the window. In the calculations of this document, if Δ is the sampling interval of the image and N_1 is the number of pixels in the χ_1

direction in the image then $w = N_1\Delta/2$. Correspondingly,

$$
\begin{aligned}
& M(\boldsymbol{\kappa}) \\
&= \int \mu(\boldsymbol{\chi}) \exp(-i2\pi\boldsymbol{\kappa}^T\boldsymbol{\chi}) \mathrm{d}^2\boldsymbol{\chi} && (5.37)\\
&= \left[\int_{\chi_1=-w/2}^{+w/2} \exp(-i2\pi\kappa_1\chi_1)\mathrm{d}\chi_1\right]\left[\int_{\chi_2=-\infty}^{+\infty} \exp(-i2\pi\kappa_2\chi_2)\mathrm{d}\chi_2\right] && (5.38)\\
&= \left[\frac{1}{-i2\pi\kappa_1}\exp(-i2\pi\kappa_1\chi_1)|_{\chi_1=-w/2}^{+w/2}\right][\delta(\kappa_2)] && (5.39)\\
&= \delta(\kappa_2)\frac{1}{-i2\pi\kappa_1}[\exp(-i2\pi\kappa_1 w/2) - \exp(i2\pi\kappa_1 w/2)] && (5.40)\\
&= \delta(\kappa_2)\frac{1}{-i2\pi\kappa_1}[-2i\sin(2\pi\kappa_1 w/2)] && (5.41)\\
&= \delta(\kappa_2)\frac{1}{\pi\kappa_1}\sin(\pi\kappa_1 w) && (5.42)\\
&= \delta(\kappa_2) w \frac{\sin(\pi\kappa_1 w)}{\pi\kappa_1 w} && (5.43)\\
&= \delta(\kappa_2) w \,\mathrm{sinc}(\kappa_1 w) && (5.44)
\end{aligned}
$$

where $\mathrm{sinc}(x) = \sin(\pi x)/(\pi x)$. Let $\mu(\boldsymbol{\chi})$ and $M(\boldsymbol{\kappa})$ denote the real-space and reciprocal-space representations of the windowed image, respectively. Therefore,

$$y(\boldsymbol{\chi}) = \mu(\boldsymbol{\chi})\sigma(\boldsymbol{\chi}) \tag{5.45}$$

which implies that

$$
\begin{aligned}
& Y(\boldsymbol{\kappa}) \\
&= M(\boldsymbol{\kappa}) * \Sigma(\boldsymbol{\kappa}) && (5.46)\\
&= \int M(\boldsymbol{\kappa}')\Sigma(\boldsymbol{\kappa}-\boldsymbol{\kappa}')\mathrm{d}^2\boldsymbol{\kappa}' && (5.47)\\
&= \int_{\kappa_1'=-\infty}^{+\infty}\int_{\kappa_2'=-\infty}^{+\infty} \delta(\kappa_2') w\,\mathrm{sinc}(\kappa_1' w)\Sigma\left((\kappa_1-\kappa_1', \kappa_2-\kappa_2')^T\right)\mathrm{d}\kappa_1'\mathrm{d}\kappa_2' && (5.48)\\
&= \int_{\kappa_1'=-\infty}^{+\infty} w\,\mathrm{sinc}(\kappa_1' w)\Sigma\left((\kappa_1-\kappa_1', \kappa_2)^T\right)\mathrm{d}\kappa_1' && (5.49)
\end{aligned}
$$

where $*$ indicates convolution (here, 2-D convolution). The expressions for $\Sigma(\boldsymbol{\kappa})$ (e.g., Eqs. 5.33–5.35) are all of the form

$$\Sigma(\boldsymbol{\kappa}) = \Sigma^{(a)}(\boldsymbol{\kappa};\beta,\gamma,\boldsymbol{\chi}_0)\sum_{l=-\infty}^{+\infty}\Sigma_l^{(b)}(\boldsymbol{\kappa};\alpha,\beta,\gamma)\delta\left(\kappa_1 - \kappa_2\tan\gamma + \frac{l}{c\sin\beta\cos\gamma}\right). \tag{5.50}$$

Inserting Eq. 5.50 in Eq. 5.49 gives

$$
\begin{aligned}
&Y(\boldsymbol{\kappa}) \\
&= \int_{\kappa_1'=-\infty}^{+\infty} w\,\mathrm{sinc}(\kappa_1' w)\Sigma^{(a)}\left((\kappa_1-\kappa_1',\kappa_2)^T;\beta,\gamma,\boldsymbol{\chi}_0\right)\times \\
&\quad\times\sum_{l=-\infty}^{+\infty}\Sigma_l^{(b)}\left((\kappa_1-\kappa_1',\kappa_2)^T;\alpha,\beta,\gamma\right)\delta\left(\kappa_1-\kappa_1'-\kappa_2\tan\gamma+\frac{l}{c\sin\beta\cos\gamma}\right)\mathrm{d}\kappa_1' \qquad (5.51)\\
&= \sum_{l=-\infty}^{+\infty}\int_{\kappa_1'=-\infty}^{+\infty} w\,\mathrm{sinc}(\kappa_1' w)\Sigma^{(a)}\left((\kappa_1-\kappa_1',\kappa_2)^T;\beta,\gamma,\boldsymbol{\chi}_0\right)\times \\
&\quad\times\Sigma_l^{(b)}\left((\kappa_1-\kappa_1',\kappa_2)^T;\alpha,\beta,\gamma\right)\delta\left(\kappa_1-\kappa_1'-\kappa_2\tan\gamma+\frac{l}{c\sin\beta\cos\gamma}\right)\mathrm{d}\kappa_1'. \qquad (5.52)
\end{aligned}
$$

Using the δ function to evaluate the κ_1' integral implies that

$$\kappa_1' = \kappa_1 - \left(\kappa_2\tan\gamma - \frac{l}{c\sin\beta\cos\gamma}\right) \qquad (5.53)$$

or, equivalently,

$$\kappa_1 - \kappa_1' = \kappa_2\tan\gamma - \frac{l}{c\sin\beta\cos\gamma} \qquad (5.54)$$

so that

$$
\begin{aligned}
Y(\boldsymbol{\kappa}) &= \sum_{l=-\infty}^{+\infty} w\,\mathrm{sinc}\left(\left(\kappa_1-\left(\kappa_2\tan\gamma-\frac{l}{c\sin\beta\cos\gamma}\right)\right)w\right)\times \\
&\quad\times\Sigma^{(a)}\left(\left(\kappa_2\tan\gamma-\frac{l}{c\sin\beta\cos\gamma},\kappa_2\right)^T;\beta,\gamma,\boldsymbol{\chi}_0\right)\times \\
&\quad\times\Sigma_l^{(b)}\left(\left(\kappa_2\tan\gamma-\frac{l}{c\sin\beta\cos\gamma},\kappa_2\right)^T;\alpha,\beta,\gamma\right). \qquad (5.55)
\end{aligned}
$$

Define

$$K_1(l;\kappa_2,c,\beta,\gamma) = \kappa_2\tan\gamma - \frac{l}{c\sin\beta\cos\gamma}. \qquad (5.56)$$

K_1 is the κ_1 location of the lth layer line as a function of the value of κ_2 and the period (c) and orientation (β and γ) of the helix. If the long axis of the helix is aligned with the χ_1 axis of the image, then $\gamma = 0$. This case is the most important

case because most experimental images are preprocessed so that the axis of the helix is in the χ_1 direction. Furthermore, this is the only case used in this document in the synthetic image results of Chapter 15. In the case of $\gamma = 0$, K_1 simplifies and loses its dependence on κ_2 because the layer lines are now along the κ_2 direction. The result is

$$K_1(l; \kappa_2, c, \beta, \gamma = 0) = -\frac{l}{c \sin \beta}. \tag{5.57}$$

Using Eq. 5.56 in Eq. 5.55 gives

$$\begin{aligned} Y(\boldsymbol{\kappa}) &= \sum_{l=-\infty}^{+\infty} w \operatorname{sinc}\left(\left(\kappa_1 - K_1(l; \kappa_2, c, \beta, \gamma)\right) w\right) \times \\ &\quad \times \Sigma^{(a)}\left(\left(K_1(l; \kappa_2, c, \beta, \gamma), \kappa_2\right)^T; \beta, \gamma, \boldsymbol{\chi}_0\right) \times \\ &\quad \times \Sigma_l^{(b)}\left(\left(K_1(l; \kappa_2, c, \beta, \gamma), \kappa_2\right)^T; \alpha, \beta, \gamma\right). \end{aligned} \tag{5.58}$$

For the case of $\gamma = 0$, Eqs. 5.33, 5.34, and 5.35, become

$$\begin{aligned} Y(\boldsymbol{\kappa}) &= \frac{1}{|\sin\beta\cos\gamma|} \sum_{l=-\infty}^{+\infty} C\left(\sqrt{\left(\frac{l}{c\sin\beta}\right)^2 + \kappa_2^2}\right) \times \\ &\quad \times \exp\left(-i2\pi\left(-\frac{l}{c\sin\beta} x_{L_1} + \kappa_2 x_{L_2}\right)\right) \times \\ &\quad \times \left[\sum_{n=-\infty}^{+\infty} G_{n,l}(R'_L) \exp(in(\psi'_L - \pi/2))\right] w \operatorname{sinc}\left(\left(\kappa_1 + \frac{l}{c\sin\beta}\right) w\right) \end{aligned} \tag{5.59}$$

for structures with no symmetry,

$$\begin{aligned} Y(\boldsymbol{\kappa}) &= \frac{1}{|\sin\beta\cos\gamma|} \sum_{l=-\infty}^{+\infty} C\left(\sqrt{\left(\frac{l}{c\sin\beta}\right)^2 + \kappa_2^2}\right) \times \\ &\quad \times \exp\left(-i2\pi\left(-\frac{l}{c\sin\beta} x_{L_1} + \kappa_2 x_{L_2}\right)\right) \times \\ &\quad \times \left[\sum_{n=-\infty}^{+\infty} \delta_{n,S_l} G_{n,l}(R'_L) \exp(in(\psi'_L - \pi/2))\right] \times \\ &\quad \times w \operatorname{sinc}\left(\left(\kappa_1 + \frac{l}{c\sin\beta}\right) w\right) \end{aligned} \tag{5.60}$$

for objects with helical symmetry, and

$$\begin{aligned} Y(\boldsymbol{\kappa}) &= \frac{1}{|\sin\beta\cos\gamma|}\sum_{l=-\infty}^{+\infty} C\left(\sqrt{\left(\frac{l}{c\sin\beta}\right)^2+\kappa_2^2}\right)\times \\ &\quad \times\exp\left(-i2\pi\left(-\frac{l}{c\sin\beta}x_{L_1}+\kappa_2 x_{L_2}\right)\right)\times \\ &\quad \times\left[\sum_{n=-\infty}^{+\infty}\frac{u\delta_{n,S_l}}{c}\sum_{j=1}^{N_j} f_j J_n(2\pi R'_L r_j)\exp\left[i\left(n(\psi'_L-\pi/2-\varphi_j)-\frac{2\pi l}{c}z_j\right)\right]\right]\times \\ &\quad \times w\,\mathrm{sinc}\left(\left(\kappa_1+\frac{l}{c\sin\beta}\right)w\right) \end{aligned} \tag{5.61}$$

for objects with helical symmetry and an impulsive electron scattering intensity where R'_L and ψ'_L are defined as functions of $\kappa_1 = K_1(l;\kappa_2,c,\beta,\gamma=0) = -l/(c\sin\beta)$, κ_2, α, β, and $\gamma = 0$ by Eqs. 5.22 and 5.24, respectively, or Eqs. 5.27 and 5.28, respectively.

Note from Eqs. 5.27 and 5.28 that R'_L depends on β but not α while ψ'_L depends on both α and β except for the 0th layer line (i.e., $l = 0$) in which case $\kappa_1 = 0$ so that ψ'_L depends on α but not β. These results have implications for the computational complexity of the algorithm (please see Chapter 9.3).

CHAPTER 6

REPRESENTING THE BESSEL ORDER TERMS BY A LINEAR SUPERPOSITION OF ORTHONORMAL BASIS FUNCTIONS

The goal of structure determination is to determine $g_{n,l}(r)$ or, equivalently, $G_{n,l}(R)$, for each (n,l) pair subject to any selection rule or other constraint imposed by a symmetry condition. The novel approach of this document is to assume that $g_{n,l}(r)$ is nonzero only in the region $r_1 \leq r \leq r_2$ in which case $g_{n,l}(r)$ can be represented as a weighted sum of basis functions which are denoted by $h_{n,p}(r)$:

$$g_{n,l}(r) = \sum_{p=1}^{\infty} d_{l,n,p} h_{n,p}(r). \tag{6.1}$$

While $r_1 = 0$ is allowed, $r_2 = \infty$ is not allowed. In this framework, the goal of structure determination is to estimate the values of the unknown weights $d_{l,n,p}$ for some range of indices (l,n,p). Representing $g_{n,l}(r)$ by Eq. 6.1 implies that

$$G_{n,l}(R) = \sum_{p=1}^{\infty} d_{l,n,p} H_{n,p}(R) \tag{6.2}$$

where $H_{n,p}(r)$ is the nth order cylindrical Hankel transform (defined in Eqs. 3.3 and 3.4) of $h_{n,p}(r)$:

$$H_{n,p}(R) = 2\pi \int_{r=0}^{\infty} h_{n,p}(r) J_n(2\pi R r) r \mathrm{d}r. \tag{6.3}$$

With the assumptions of Eqs. 6.1 and 6.2, the previous formulas can be rewritten in terms of the unknown weights $d_{l,n,p}$: Eq. 4.2 (real-space 3-D cube, periodicity only) becomes

$$\rho(r,\varphi,z) = \sum_{l=-\infty}^{+\infty} \sum_{n=-\infty}^{+\infty} \left[\sum_{p=1}^{\infty} d_{l,n,p} h_{n,p}(r) \right] \exp\left[i \left(n\varphi + \frac{2\pi}{c} l z \right) \right], \tag{6.4}$$

Eq. 4.16 (reciprocal-space 3-D cube, periodicity only) becomes

$$F(R,\psi,\zeta) = \sum_{l=-\infty}^{+\infty} \left[\sum_{n=-\infty}^{+\infty} \left[\sum_{p=1}^{\infty} d_{l,n,p} H_{n,p}(R) \right] \exp(in(\psi - \pi/2)) \right] \delta\left(\zeta - \frac{l}{c} \right), \tag{6.5}$$

Eq. 5.33 (reciprocal-space 2-D image, periodicity only) becomes

$$\begin{aligned}\Sigma(\boldsymbol{\kappa}) &= \frac{1}{|\sin\beta\cos\gamma|}C(|\boldsymbol{\kappa}|)\exp(-i2\pi\boldsymbol{\kappa}^T\boldsymbol{\chi}_0)\times \\ &\quad\times\sum_{l=-\infty}^{+\infty}\delta\left(\kappa_1-\kappa_2\tan\gamma+\frac{l}{c\sin\beta\cos\gamma}\right)\times \\ &\quad\times\left[\sum_{n=-\infty}^{+\infty}\left[\sum_{p=1}^{\infty}d_{l,n,p}H_{n,p}(R'_L)\right]\exp(in(\psi'_L-\pi/2))\right], \end{aligned} \tag{6.6}$$

Eq. 5.34 (reciprocal-space 2-D image, helical symmetry) becomes

$$\begin{aligned}\Sigma(\boldsymbol{\kappa}) &= \frac{1}{|\sin\beta\cos\gamma|}C(|\boldsymbol{\kappa}|)\exp(-i2\pi\boldsymbol{\kappa}^T\boldsymbol{\chi}_0)\times \\ &\quad\times\sum_{l=-\infty}^{+\infty}\delta\left(\kappa_1-\kappa_2\tan\gamma+\frac{l}{c\sin\beta\cos\gamma}\right)\times \\ &\quad\times\left[\sum_{n=-\infty}^{+\infty}\delta_{n,S_l}\left[\sum_{p=1}^{\infty}d_{l,n,p}H_{n,p}(R'_L)\right]\exp(in(\psi'_L-\pi/2))\right], \end{aligned} \tag{6.7}$$

Eq. 5.59 (reciprocal-space 2-D windowed image, only periodicity) becomes

$$\begin{aligned}&Y(\boldsymbol{\kappa}) \\ &= \frac{1}{|\sin\beta\cos\gamma|}\sum_{l=-\infty}^{+\infty}C\left(\sqrt{\left(\frac{l}{c\sin\beta}\right)^2+\kappa_2^2}\right)\times \\ &\quad\times\exp\left(-i2\pi\left(-\frac{l}{c\sin\beta}x_{L_1}+\kappa_2 x_{L_2}\right)\right)\times \\ &\quad\times\left[\sum_{n=-\infty}^{+\infty}\left[\sum_{p=1}^{\infty}d_{l,n,p}H_{n,p}(R'_L)\right]\exp(in(\psi'_L-\pi/2))\right]\times \\ &\quad\times w\,\mathrm{sinc}\left(\left(\kappa_1+\frac{l}{c\sin\beta}\right)w\right), \end{aligned} \tag{6.8}$$

and Eq. 5.60 (reciprocal-space 2-D windowed image, helical symmetry) becomes

$$\begin{aligned}&Y(\boldsymbol{\kappa}) \\ &= \frac{1}{|\sin\beta\cos\gamma|}\sum_{l=-\infty}^{+\infty}C\left(\sqrt{\left(\frac{l}{c\sin\beta}\right)^2+\kappa_2^2}\right)\times \\ &\quad\times\exp\left(-i2\pi\left(-\frac{l}{c\sin\beta}x_{L_1}+\kappa_2 x_{L_2}\right)\right)\times \end{aligned}$$

$$\times \left[\sum_{n=-\infty}^{+\infty} \delta_{n,S_l} \left[\sum_{p=1}^{\infty} d_{l,n,p} H_{n,p}(R'_L) \right] \exp(in(\psi'_L - \pi/2)) \right] \times$$
$$\times w \operatorname{sinc}\left(\left(\kappa_1 + \frac{l}{c \sin\beta} \right) w \right) \tag{6.9}$$

where R'_L and ψ'_L are defined as functions of $\kappa_1 = K_1(l; \kappa_2, c, \beta, \gamma = 0) = -l/(c \sin\beta)$, κ_2, α, β, and $\gamma = 0$ by Eqs. 5.22 and 5.24, respectively, and

$$\boldsymbol{\chi}_0 = (x_{L_1}, x_{L_2})^T \tag{6.10}$$

The key feature of all of these equations is that they are linear in the unknown weights $d_{l,n,p}$ though the coefficients of the linear operator depend on the unknown parameters (u, v, c) and $(\alpha, \beta, \gamma, x_{L_1}, x_{L_2})$. After the infinite sums are truncated, let N_d be the number of (l, n, p) triples that are used. It is most natural to consider only triples which satisfy the helical selection rule although that is not necessary in order to make the following definitions. For computation, the reciprocal-space 2-D image will be sampled at values $\boldsymbol{\kappa}_\xi$ and let N_y be the number of samples. Array the values of $d_{l,n,p}$ in a N_d-dimensional vector denoted by d and the values of $Y(\boldsymbol{\kappa}_\xi)$ in a N_y-dimensional vector denoted by y. Define

$$\tau = (\alpha, \beta, \gamma, x_{L_1}, x_{L_2}) \tag{6.11}$$

and

$$\eta = (u, v, c). \tag{6.12}$$

Then Eq. 6.9 is equivalent to

$$y = L(\tau, \eta) d \tag{6.13}$$

where the matrix L, with dimensions $N_y \times N_d$, has elements

$$(L(\tau, \eta))_{\xi,(l,n,p)}$$
$$= \frac{1}{|\sin\beta \cos\gamma|} C \left(\sqrt{\left(\frac{l}{c \sin\beta} \right)^2 + \kappa_{\xi,2}^2} \right) \exp\left(-i2\pi \left(-\frac{l}{c \sin\beta} x_{L_1} + \kappa_{\xi,2} x_{L_2} \right) \right) \times$$

$$\times \delta_{n,S_l} d_{l,n,p} H_{n,p}(R'_L) \exp(in(\psi'_L - \pi/2)) w \operatorname{sinc}\left(\left(\kappa_{\xi,1} + \frac{l}{c \sin\beta}\right) w\right) \tag{6.14}$$

where $\boldsymbol{\kappa}_\xi = (\kappa_{\xi,1}, \kappa_{\xi,2})^T$. R'_L and ψ'_L are defined as functions of $\kappa_{\xi,1} = K_1(l; \kappa_{\xi,2}, c, \beta, \gamma = 0) = -l/(c \sin\beta)$, $\kappa_{\xi,2}$, α, β, and $\gamma = 0$ by Eqs. 5.22 and 5.24, respectively.

6.1 Defining $h_{n,p}(r)$

The goal is that for each n, the functions $h_{n,p}(r)$ ($p \in \{1, 2, \ldots\}$) form a complete orthonormal basis for square-integrable functions on $r_1 \leq r \leq r_2$. The choices made in this section yield $h_{n,p}(r) \in \mathbb{R}$ and $H_{n,p}(R) \in \mathbb{R}$.

6.1.1 The case where $r_1 = 0$ and $\rho(\mathbf{x} = \mathbf{0}) \neq 0$

While basis functions exist for this case, they are not developed in this document.

6.1.2 The case where $r_1 = 0$ and $\rho(\mathbf{x} = \mathbf{0}) = 0$ or where $r_1 > 0$

The Sturm-Liouville problem

The basis functions are defined by a Sturm-Liouville problem for the second-order ordinary differential equation that is one definition of cylindrical Bessel functions. From the general theory of Sturm-Liouville problems [30, Chap. 7], the resulting countably-infinite set of functions is a complete basis in the space of square

integrable functions on the chosen subset of $\mathbb{R}$. Let primed and double primed functions denote first and second derivatives, respectively. The differential equation for cylindrical Bessel functions is [25, p. 550]

$$r^2 z''(r) + r z'(r) + (r^2 - n^2) z(r) = 0. \tag{6.15}$$

Define

$$y(r) = z(\gamma r) \tag{6.16}$$

or, equivalently,

$$y(r/\gamma) = z(r). \tag{6.17}$$

From Eq. 6.16 and the chain rule it follows that the derivatives of y are

$$y'(r) = z'(\gamma r)\gamma \tag{6.18}$$

$$y''(r) = z''(\gamma r)\gamma^2. \tag{6.19}$$

Therefore

$$y'(r)/\gamma = z'(\gamma r) \tag{6.20}$$

$$y''(r)/\gamma^2 = z''(\gamma r) \tag{6.21}$$

and therefore

$$y'(r/\gamma)/\gamma = z'(r) \tag{6.22}$$

$$y''(r/\gamma)/\gamma^2 = z''(r). \tag{6.23}$$

Substituting Eqs. 6.17, 6.22, and 6.23 into Eq. 6.15 gives

$$r^2 y''(r/\gamma)/\gamma^2 + r y'(r/\gamma)/\gamma + (r^2 - n^2) y(r/\gamma) = 0 \tag{6.24}$$

which implies

$$(\gamma r)^2 y''(r)/\gamma^2 + \gamma r y'(r)/\gamma + ((\gamma r)^2 - n^2) y(r) = 0 \tag{6.25}$$

which implies

$$r^2y''(r) + ry'(r) + (\gamma^2r^2 - n^2)y(r) = 0. \tag{6.26}$$

Since the general solution to Eq. 6.15 is

$$c_1J_n(r) + c_2Y_n(r) \tag{6.27}$$

it follows from Eq. 6.16 that the general solution to Eq. 6.26, which is the equation to which Sturm-Liouville theory will be applied, is

$$h_n(r) = c_1J_n(\gamma_n r) + c_2Y_n(\gamma_n r) \tag{6.28}$$

where c_1 and c_2 are arbitrary constants. Impose the boundary conditions

$$y(a) = 0, y(b) = 0 \tag{6.29}$$

on Eq. 6.26 where a and b rather than r_1 and r_2, respectively, are used in order to simplify notation. Since $h_n(r)$ must satisfy the boundary conditions, if follows that

$$c_1J_n(\gamma_n a) + c_2Y_n(\gamma_n a) = 0 \tag{6.30}$$

$$c_1J_n(\gamma_n b) + c_2Y_n(\gamma_n b) = 0 \tag{6.31}$$

or equivalently that

$$\begin{bmatrix} J_n(\gamma_n a) & Y_n(\gamma_n a) \\ J_n(\gamma_n b) & Y_n(\gamma_n b) \end{bmatrix} \begin{bmatrix} c_1 \\ c_2 \end{bmatrix} = \begin{bmatrix} 0 \\ 0 \end{bmatrix}. \tag{6.32}$$

From Eq. 6.32 it follows that a necessary and sufficient condition for Eq. 6.28 to represent the solution of the Sturm-Liouville problem is that

$$\det \begin{bmatrix} J_n(\gamma_n a) & Y_n(\gamma_n a) \\ J_n(\gamma_n b) & Y_n(\gamma_n b) \end{bmatrix} = 0 \tag{6.33}$$

or equivalently that

$$J_n(\gamma_n a)Y_n(\gamma_n b) - J_n(\gamma_n b)Y_n(\gamma_n a) = 0. \tag{6.34}$$

Eq. 6.34 has an countably-infinite number of solutions for γ_n which are labeled $\gamma_{n,p}$ for $p \in \{1, 2, \ldots\}$. When the pth solution is used, the resulting basis function is labeled $h_{n,p}(r)$. The $h_{n,p}(r)$ function is only defined up to a multiplicative scaling.

Rearrange Eq. 6.30 to give

$$c_1 = -c_2 \frac{Y_n(\gamma_{n,p}a)}{J_n(\gamma_{n,p}a)}. \tag{6.35}$$

Set

$$c_2 = J_n(\gamma_{n,p}a) \tag{6.36}$$

in which case it follows that

$$c_1 = -Y_n(\gamma_{n,p}a). \tag{6.37}$$

Then,

$$h_{n,p}(r) = \begin{cases} \left[-Y_n(\gamma_{n,p}a)J_n(\gamma_{n,p}r) + J_n(\gamma_{n,p}a)Y_n(\gamma_{n,p}r)\right]/M_{n,p}, & a \le r \le b \\ 0, & \text{otherwise} \end{cases} \tag{6.38}$$

where $M_{n,p}$ is an arbitrary scaling.

Mathematical facts concerning Bessel functions

There are two key indefinite integrals [31, Eq. 7.14.1 (9)-(10)]:

$$\begin{aligned} &\int w_\nu(\alpha z)W_\nu(\beta z)z\mathrm{d}z \\ &\quad = z(\beta^2 - \alpha^2)^{-1}\left[\beta W_{\nu+1}(\beta z)w_\nu(\alpha z) - \alpha W_\nu(\beta z)w_{\nu+1}(\alpha z)\right] \end{aligned} \tag{6.39}$$

$$\begin{aligned} &\int w_\nu(\alpha z)W_\nu(\alpha z)z\mathrm{d}z \\ &\quad = \frac{1}{4}z^2\left[2w_\nu(\alpha z)W_\nu(\alpha z) - w_{\nu+1}(\alpha z)W_{\nu-1}(\alpha z) - w_{\nu-1}(\alpha z)W_{\nu+1}(\alpha z)\right] \end{aligned} \tag{6.40}$$

where $w_\nu(\cdot)$ and $W_\nu(\cdot)$ are any cylindrical Bessel functions of the first, second, or third kinds of the same order ν. There are four key recursions [31, 7.2.7 (54)–(57)] for Bessel functions of the first, second, or third kinds. Similar relationships hold for modified Bessel functions. In terms of $W_\nu(\cdot)$ which is any cylindrical Bessel function of the first, second, or third kind of order ν, the recursions are

$$\begin{aligned} zW'_\nu(z) + \nu W_\nu(z) &= zW_{\nu-1}(z), && (6.41)\\ zW'_\nu(z) - \nu W_\nu(z) &= -zW_{\nu+1}(z), && (6.42)\\ W_{\nu-1}(z) + W_{\nu+1}(z) &= 2\nu z^{-1} W_\nu(z), && (6.43)\\ W_{\nu-1}(z) - W_{\nu+1}(z) &= 2W'_\nu(z).. && (6.44) \end{aligned}$$

Eqs. 6.41 and 6.42 can be rearranged to give for $J_\nu(\cdot)$ and $Y_\nu(\cdot)$, specifically,

$$\begin{aligned} J_{v-1}(z) &= J'_v(z) + \frac{v}{z} J_v(z) && (6.45)\\ J_{v+1}(z) &= -J'_v(z) + \frac{v}{z} J_v(z) && (6.46)\\ Y_{v-1}(z) &= Y'_v(z) + \frac{v}{z} Y_v(z) && (6.47)\\ Y_{v+1}(z) &= -Y'_v(z) + \frac{v}{z} Y_v(z). && (6.48) \end{aligned}$$

The calculation of the normalizer

The functions defined by Eq. 6.38 are orthogonal but not necessarily orthonormal. To achieve orthonormality, it is necessary to chose a particular definition of $M_{n,p}$. The requirement is that

$$\int_{r=0}^{\infty} h_{n,p}^2(r) r \mathrm{d}r = 1 \tag{6.49}$$

which implies that

$$M_{n,p}^2 = \int_{r=0}^{\infty} \left[-Y_n(\gamma_{n,p} a) J_n(\gamma_{n,p} r) + J_n(\gamma_{n,p} a) Y_n(\gamma_{n,p} r) \right]^2 r \mathrm{d}r. \tag{6.50}$$

This integral can be done explicitly by using Eqs. 6.39–6.40 and 6.45–6.48 as is shown in Appendix A. The result is

$$\begin{aligned} M_{n,p}^2 &= \frac{1}{2}\Big\{b^2[J_n(\gamma_{n,p}a)Y_n'(\gamma_{n,p}b) - J_n'(\gamma_{n,p}b)Y_n(\gamma_{n,p}a)]^2 \\ &\quad - a^2[J_n(\gamma_{n,p}a)Y_n'(\gamma_{n,p}a) - J_n'(\gamma_{n,p}a)Y_n(\gamma_{n,p}a)]^2\Big\}. \end{aligned} \tag{6.51}$$

The calculation of $H_{n,p}(R)$

The function $H_{n,p}(R)$ is the nth order cylindrical Hankel transform (Eqs. 3.3 and 3.4) of the function $h_{n,p}(r)$. Because of Eq. 6.39, the cylindrical Hankel transform can be computed symbolically which is the primary reason for using the Bessel function differential equation in the Sturm-Liouville problem. As is shown in more detail in Appendix B, the cylindrical Hankel transform is

$$H_{n,p}(R) = 2\pi \int_a^b h_{n,p}(r) J_n(2\pi R r) r \mathrm{d}r \tag{6.52}$$

$$= 2\pi \frac{b h_{n,p}'(b) J_n(2\pi R b) - a h_{n,p}'(a) J_n(2\pi R a)}{(2\pi R)^2 - \gamma_{n,p}^2} \tag{6.53}$$

where $h_{n,p}'(\cdot)$ is the derivative of $h_{n,p}(\cdot)$. If $2\pi R = \gamma_{n,p}$ then, by L'Hospital's Rule,

$$H_{n,p}(R) = \pi \frac{b^2 h_{n,p}'(b) J_n'(\gamma_{n,p}b) - a^2 h_{n,p}'(a) J_n'(\gamma_{n,p}a)}{\gamma_{n,p}}. \tag{6.54}$$

6.2 Computing $d_{l,n,p}$ from a known $\rho(\mathbf{x})$, including the case of an impulsive $\rho(\mathbf{x})$

Since $d_{l,n,p}$ and $h_{n,p}(r)$ are related by Eq. 6.1 and $h_{n,p}(r)$ are a complete orthonormal basis, it follows that

$$d_{l,n,p} = \int_{r=0}^{\infty} g_{n,l}(r) h_{n,p}(r) r \mathrm{d}r. \tag{6.55}$$

Then, for the case of helical symmetry, by Eq. 4.42 it follows that

$$\begin{aligned} & d_{l,n,p} \\ & = \int_{r=0}^{\infty} \frac{u\delta_{n,S_l}}{2\pi c} \int_{z'=0}^{c/u} \int_{\varphi'=0}^{2\pi} \rho\left(r,\varphi',z'\right) \exp\left[-i\left(n\varphi' + \frac{2\pi l}{c} z'\right)\right] \mathrm{d}\varphi' \mathrm{d}z' h_{n,p}(r) r \mathrm{d}r. \end{aligned} \tag{6.56}$$

When $\rho(\mathbf{x})$ is impulsive, i.e., Eq. 4.56, it follows that

$$d_{l,n,p} = \frac{u\delta_{n,S_l}}{2\pi c} \sum_{j=1}^{N_j} f_j \exp\left[-i\left(n\varphi_j + \frac{2\pi l}{c} z_j\right)\right] h_{n,p}(r_j). \tag{6.57}$$

CHAPTER 7

STATISTICAL NOISE MODEL

An Additive White Gaussian Noise (AWGN) model is used to describe the uncertainty of pixel values in the real-space 2-D image. Therefore, since real- and reciprocal-space 2-D images are related by a 2-D Fourier transform, the noise in reciprocal space is also AWGN. Continue with the vector notation for y and d that was introduced in Section 6 and use similar notation for the noise which is denoted by $w(\boldsymbol{\chi})$ in real space and $W(\boldsymbol{\kappa})$ in reciprocal space. Then

$$y = L(\tau, \eta)d + w \tag{7.1}$$

where w is the vector of pixel noises and τ (η) was defined in Eq. 6.11 (Eq. 6.12). Let $N(\mu, Q)(x)$ be the multivariate Gaussian probability density function (pdf) with mean μ and covariance Q. Then w has pdf $N(0, K)$ where K is proportional to the identity matrix. Since the theory to be developed in the following sections does not depend on the structure of K, beyond the fact that K is a covariance matrix and therefore $K = K^T$ and $K > 0$, the general notation of an arbitrary covariance matrix K is used. However, in the software, the fact that K is proportional to the identity can be exploited to decrease the computational burden. The additive Gaussian model is used rather than alternative models, such as Poisson models, which more accurately describe at least the electron-counting parts of the physics of the microscope. The reason for using the additive Gaussian model is that it greatly reduces the computation in the maximum likelihood (ML) estimator for $d_{l,n,p}$ when the ML estimator is computed by an expectation maximization algorithm because the maximization step of the algorithm is to maximize a quadratic form which can be done by solving a linear system of equations. When multiple images are considered, it is natural to consider the noise present in each image to

be independent. This independence assumption allows the joint pdf for all of the images conditional on the values of (u, v, c) and $(\alpha, \beta, \gamma, x_{L_1}, x_{L_2})$ for each image to factor. The factorization reduces computation in the computation of the ML estimate by expectation maximization in the expectation step.

CHAPTER 8

INVERSE PROBLEM

8.1 The maximum likelihood (ML) estimators

The approach of this document is to simultaneously solve for the parameters that define the helical symmetry and the 3-D structure by using a maximum likelihood (ML) estimator. The image-formation probability density function (pdf) is

$$p(y|\alpha,\beta,\gamma,x_{L_1},x_{L_2},u,v,c,d) = N(L(\alpha,\beta,\gamma,x_{L_1},x_{L_2},u,v,c)d,K)(y) \tag{8.1}$$

where x_{L_1} and x_{L_2} are defined in Eq. 6.10. The parameters to be estimated are (u,v,d). The remaining parameters,

$$z = (\alpha,\beta,\gamma,x_{L_1},x_{L_2},c), \tag{8.2}$$

are treated as nuisance parameters which means that *a priori* pdfs for these parameters are defined and used to integrate these parameters out of the likelihood function. Specifically, the likelihood function to be maximized with respect to (u,v,d) is

$$p(y|u,v,d) = \int_z p(y|z,u,v,d)\mathrm{d}z \tag{8.3}$$

and so the estimate is

$$\widehat{u,v,d} = \arg\max_{u,v,d} p(y|u,v,d). \tag{8.4}$$

The nuisance parameters for different images are assumed to be independent random variables. The motivation for the independence assumption is complicated. The orientational parameters $(\alpha,\beta,\gamma,x_{L_1},x_{L_2})$ are probably independent from object to object. However, more is assumed. In particular, most biological helical objects are imperfect helices. Therefore, most processing of an image of a helical object is done by first dividing the image into subimages which are sufficiently

Table 8.1: Nuisance parameter ranges and *a priori* probability density functions: α describes rotation around the long axis (z-axis) of the helix, β describes how the helix is tilted out of the plane of the microscope stage, γ describes rotation around the z-axis in the plane of the microscope stage, and x_{L_1} and x_{L_2} describe the translational shift along x_1 and x_2 directions, respectively. $0 \leq \beta_0 < \frac{\pi}{2}$, $0 \leq \gamma_0 < \pi$, $0 \leq \epsilon \ll 1$.

nuisance parameter	pdf	interval
α	uniform	$[0, 2\pi)$
β		$[\frac{\pi}{2} - \beta_0, \frac{\pi}{2} + \beta_0]$
γ		$[0, \gamma_0) \cup [2\pi - \gamma_0, 2\pi)$
x_{L_1}		$[0, (c \sin \beta)/u)$
x_{L_2}		$[-N_{x_{L_2}}\Delta, N_{x_{L_2}}\Delta]$
c		$[(1-\epsilon)c_0, (1+\epsilon)c_0]$

small such that the assumption of perfect helical symmetry is accurate. We assume that the orientational parameters $(\alpha, \beta, \gamma, x_{L_1}, x_{L_2})$ for each subimage are independent while, in fact, there is some dependence because the imperfect helical object does have some helical character that extends over the entire image. However, the dependence is difficult to quantify. For the problems of interest in this document all images (and therefore all subimages) share the same nominal helical symmetry, where the word "nominal" is used in recognition of the fact that the symmetry is imperfectly obeyed. Therefore, (u, v, c) are nominally the same for all images (including all subimages). For (u, v) this characteristic is enforced exactly and there is only one (u, v) pair for all images (including all subimages). However, for c this characteristic is relaxed and c is treated like an orientational parameter and assumed to be independent from subimage to subimage. The nuisance parameters have *a priori* pdfs that are tabulated in Table 8.1.

This approach is similar to the approach of Refs. [28, 29, 32] and, in particular, the fact that the nuisance parameters for different subimages are independent implies that it is a Case 1 problem in the classification of Ref. [28]. The approach

is also similar to the approach of Ref. [1] except that the method of describing the object by a finite number of parameters is completely different (compare Eq. 6.14 with the corresponding equations in Ref. [33]) and that Ref. [1] also considers the situation where one value of c is common to all images (including all subimages), i.e., so that c is treated like (u, v) rather than like $(\alpha, \beta, \gamma, x_{L_1}, x_{L_2})$.

To simplify the notation, let

$$\omega = (u, v). \tag{8.5}$$

There are several reasons why ω is chosen not to be a nuisance parameter. First, eventually the value of ω is necessary in order to use the estimated coefficients d to reconstruct the helical object, though its value could be estimated in a second step analogous to what is done for c [34]. Second, it is difficult to specify the joint probability mass function on the u and v components of ω. Third, changing u and v changes the selection rule which implies a different set of (l, n, p) indices are permitted and this change would complicate the data structure for d. Fourth, estimating ω rather than treating it as a nuisance parameter leads to software that can easily be parallelized, which leads to decreased wall clock time. In order to treat all values of ω equivalently, the same number of $d_{l,n,p}$ coefficients are estimated for each value of ω (i.e., N_d is constant) even though the coefficients contribute to different sets of Bessel orders due to the different selection rules implied by different values of ω.

Soft constraints of packing in the helical object limit the allowed pairs of (u, v) [1]. The resulting list has less than 100 elements and therefore it is practical to compute the maximum likelihood estimate (Eq. 8.4) by computing the maximum over d for fixed (u, v) for each element in the list and finally taking the

maximum of the maxima, that is,

$$\widehat{\omega, d} = \arg \max_{\omega,d} p(y|\omega, d) \tag{8.6}$$

can be implemented by

$$\hat{\omega} = \arg \max_{\omega} \left[\max_{d} p(y|\omega, d) \right] \tag{8.7}$$

$$\hat{d} = \arg \max_{d} p(y|\hat{\omega}, d). \tag{8.8}$$

Pseudo-code implementing this approach, where the pseudo-code includes results from Chapter 9, is:

---

pseudo code

for ω in ω_list **do**
  while not_converged (d_0, d_*) **do**
    $d_0 = d_*$
    $[T, g] = \text{get}_{Tg}(\omega, d_0, y)$
    Solve $Td = g$ for d_*
  end while
  Store d_* and $p(y|\omega, d_*)$ indexed by ω
end for
$\hat{\omega}$ = index of the largest $p(y|\omega, d_*)$
$\hat{d} = d_*(\hat{\omega})$

8.2 Uniqueness of the inverse problem

If only one image is recorded of each object then a unique reconstruction is not possible since it is not possible to distinguish $\rho(\mathbf{x})$ from $\rho'(\mathbf{x}) = \rho(-\mathbf{x})$. If $\rho(\mathbf{x})$ has right-handed helical symmetry then $\rho'(\mathbf{x})$ has left-handed helical symmetry. Therefore, if it is possible to achieve atomic resolution, which is unusual, the correct choice can be made since all biological amino acids are left handed and so which ever of $\rho(\mathbf{x})$ and $\rho'(\mathbf{x})$ show left-handed amino acids is the correct structure.

However, if multiple images of the same object are recorded where the projection directions of the different images are different and at least the relative projection directions are known, then it is possible to compute a unique reconstruction [22].

In terms of $g_{n,l}(r)$ functions, the relation between right- and left-handed helical objects is $g_{n,l}(r) = g'_{n,-l}(r)$. Using this fact, it is always possible to assume that the object is right handed (or left handed) and then perform the above operation to reverse the hand if the object is later determined to be left handed (or right handed).

CHAPTER 9

THE EXPECTATION MAXIMIZATION (EM) ALGORITHM FOR COMPUTING MAXIMUM LIKELIHOOD (ML) ESTIMATORS

9.1 General comments

A variety of nonlinear programming algorithms are available to maximize the likelihood defined by Eq. 8.3. Most algorithms compute a search direction and then perform a line search along that direction. The line search requires appropriate step sizes, and choosing step sizes has been a challenge in electron microscopy problems [35]. Because our problem formulation has natural nuisance variables and expectation maximization (EM) algorithms do not require step sizes, we have computed the maximum likelihood (ML) estimate via an EM algorithm where the natural nuisance parameters are used.

EM algorithms are local search algorithms. As is described in Chapter 13, we address that issue by testing multiple different initial conditions.

EM algorithms are iterative algorithms. Therefore, the EM algorithm requires a convergence test which is also described in Chapter 13.

At each iteration, an EM algorithm performs both an expectation and a maximization step. In our problem, the expectation step, which integrates out the nuisance parameters given their known pdfs, represents the bulk of the computation and the maximization step, a maximization over the unknown parameter values in order to compute the next in the sequence of parameter value estimates, is a simple computation, in particular, the solution of a linear system. As discussed in Chapter 7, this simplicity follows from our assumption of a Gaussian model and

is one of the primary motivations for the Gaussian assumption.

9.2 Detailed results

Let y_i for $i \in \{1, \ldots, N_v\}$ denote the total set of subimages. Using Eq. 7.1 for each subimage, it follows that,

$$y_i = L_i(z_i, \omega)d + w_i \tag{9.1}$$

where w_i is independent and identically distributed with pdf $N(0, K_i)$. Let y and z denote the vector representation of all y_i and all z_i for $i \in \{1, ..., N_v\}$, respectively. Let N_y be the total number of pixels in an image. (In detail, we divide a complex-valued pixel into real and imaginary parts and count the resulting number of real numbers after accounting for the conjugate symmetry implied by $\rho(\mathbf{x}) \in \mathbb{R}$). Recall that ω is to be estimated by ML using an EM algorithm in which z_i ($i \in \{1, \ldots, N_v\}$) is the nuisance parameter to be integrated out for the ith image. When multiple images are processed, the generalization of Eq. 8.1 is

$$p(y|z, \omega, d) = \prod_{i=1}^{N_v} N(L_i(z_i, \omega)d, K_i)(y_i). \tag{9.2}$$

The expectation step in the EM algorithm is to compute

$$Q(\omega, d|\omega_0, d_0, y) = \int_z \ln\left[p(y, z|\omega, d)\right] p(z|\omega_0, d_0, y)\mathrm{d}z. \tag{9.3}$$

It can be shown that

$$Q(\omega, d|\omega_0, d_0, y) = \prod_{i=1}^{N_v} Q_i(\omega, d|\omega_0, d_0, y) \tag{9.4}$$

where

$$Q_i(\omega, d|\omega_0, d_0, y) = \frac{\int_{z_i} \ln\left[p(y_i|z_i, \omega, d)p(z_i)\right] p(y_i|z_i, \omega_0, d_0)p(z_i)\mathrm{d}z_i}{\int_{z_i} p(y_i|z_i, \omega_0, d_0)p(z_i)\mathrm{d}z_i}. \tag{9.5}$$

We now incorporate the details of the Gaussian pdf $p(y_i|z_i,\omega,d)$. Define

$$\begin{aligned} a_i(y_i,z_i,\omega) &= \ln\left[(2\pi)^{\frac{N_y}{2}}\sqrt{\det K_i}\right] + \frac{1}{2}y_i^T K_i^{-1} y_i && (9.6)\\ b_i(y_i,z_i,\omega) &= L_i^T(z_i,\omega)K_i^{-1}y_i && (9.7)\\ D_i(z_i,\omega) &= L_i^T(z_i,\omega)K_i^{-1}L_i(z_i,\omega) && (9.8)\end{aligned}$$

where the dimensions of a_i, b_i, D_i are $N_{z_i}\times N_v$, $N_d\times N_{z_i}\times N_v$, and $N_d\times N_d\times N_{z_i}$, respectively, where N_{z_i} is the number of abscissas that are eventually required to perform a numerical integral over the nuisance parameters in z_i. Then

$$\begin{aligned} p(y_i|z_i,\omega,d) &= N(L_i(z_i,\omega)d, K_i)(y_i)\\ &= \exp\left[-a_i(y_i,z_i,\omega) + b_i^T(y_i,z_i,\omega)d - \frac{1}{2}d^T D_i(z_i,\omega)d\right]. \quad (9.9)\end{aligned}$$

Note that

$$\ln p(y_i|z_i,\omega,d) = -a_i(y_i,z_i,\omega) + b_i^T(y_i,z_i,\omega)d - \frac{1}{2}d^T D_i(z_i,\omega)d. \quad (9.10)$$

Define

$$\begin{aligned} \alpha_i(y_i,\omega,d) &= \int_{z_i} a_i(y_i,z_i,\omega)p(y_i|z_i,\omega,d)p(z_i)\mathrm{d}z_i && (9.11)\\ \beta_i(y_i,\omega,d) &= \int_{z_i} b_i(y_i,z_i,\omega)p(y_i|z_i,\omega,d)p(z_i)\mathrm{d}z_i && (9.12)\\ \Delta_i(y_i,\omega,d) &= \int_{z_i} D_i(y_i,z_i,\omega)p(y_i|z_i,\omega,d)p(z_i)\mathrm{d}z_i && (9.13)\\ \gamma_i(y_i,\omega,d) &= \int_{z_i} p(y_i|z_i,\omega,d)p(z_i)\mathrm{d}z_i && (9.14)\\ \upsilon_i(y_i,\omega,d) &= \int_{z_i} \ln\left[p(z_i)\right]p(y_i|z_i,\omega,d)p(z_i)\mathrm{d}z_i && (9.15)\\ I_i(\omega,d|\omega_0,d_0,y_i) &= \int_{z_i} \ln\left[p(y_i|z_i,\omega,d)\right]p(y_i|z_i,\omega_0,d_0)p(z_i)\mathrm{d}z_i && (9.16)\\ &= -\alpha_i(y_i,\omega_0,d_0) + \beta_i^T(y_i,\omega_0,d_0)d - \frac{1}{2}d^T\Delta_i(y_i,\omega_0,d_0)d. && (9.17)\end{aligned}$$

We have

$Q(\omega,d|\omega_0,d_0,y)$

$$= \sum_{i=1}^{N_v} \frac{I_i(\omega, d|\omega_0, d_0, y_i) + \upsilon_i(y_i, \omega_0, d_0)}{\gamma_i(y_i, \omega_0, d_0)} \tag{9.18}$$

$$= \sum_{i=1}^{N_v} \frac{\left[-\alpha_i(y_i, \omega_0, d_0) + \beta_i^T(y_i, \omega_0, d_0)d - \frac{1}{2}d^T\Delta_i(y_i, \omega_0, d_0)d + \upsilon_i(y_i, \omega_0, d_0)\right]}{\gamma_i(y_i, \omega_0, d_0)} \tag{9.19}$$

$$= -h(\omega, \omega_0, d_0, y) + g^T(\omega, \omega_0, d_0, y)d - \frac{1}{2}d^T T(\omega, \omega_0, d_0, y)d \tag{9.20}$$

where

$$T(\omega, \omega_0, d_0, y) = \sum_{i=1}^{N_v} \frac{\Delta_i(y_i, \omega_0, d_0)}{\gamma_i(y_i, \omega_0, d_0)} \tag{9.21}$$

$$g(\omega, \omega_0, d_0, y) = \sum_{i=1}^{N_v} \frac{\beta_i(y_i, \omega_0, d_0)}{\gamma_i(y_i, \omega_0, d_0)} \tag{9.22}$$

$$h(\omega, \omega_0, d_0, y) = \sum_{i=1}^{N_v} \frac{-\alpha_i(y_i, \omega_0, d_0) + \upsilon_i(y_i, \omega_0, d_0)}{\gamma_i(y_i, \omega_0, d_0)}. \tag{9.23}$$

These formulas complete the expectation step of the EM algorithm.

To locate the maximum of Q with respect to d is straightforward because Eq. 9.20 is a quadratic form. In particular, the location is the solution of the linear equation found by setting the gradient of Q with respect to d equal to zero:

$$Td = g. \tag{9.24}$$

Therefore even for a large number of d's (e.g., N_d on the order of 10^3), the maximization computation contributes little to the computational burden in comparison with the expectation step which typically involves N_{z_i} on the order of 10^5 abscissas.

9.3 Computation complexity of the EM algorithm

This section contains a list of useful observations that help decrease the computation complexity of the EM algorithm.

1. Due to conjugate symmetry property in reciprocal space, only half of the data needs to be processed for a real-valued object. Furthermore, in order to achieve a resolution of 10Å, only the data up to 7th layer line (i.e., $l = 7$) is needed.

2. Due to the periodicity of the helical object in the z direction, the reciprocal space is composed of layer lines with a line width due to windowing. By ignoring the regions of reciprocal space outside of the widened layer lines, many rows in the L matrix can be dropped, equivalently, N_y is reduced, without removing any information from the estimation problem.

3. $H_{n,p}(R'_L)$ is a complicated and nested function which must be computed in order to compute L. Many L values are required, in particular, a different value for each of the z_i abscissas of which there are N_{z_i}. However, $H_{n,p}(R'_L)$ is not a function of α (Eq. 5.22) and therefore only needs to be computed N_{z_i}/N_α times where N_α is the number of abscissas for α in an overall rule which is the product of rules for each element in z_i (Eq. 8.2).

4. If one image is processed instead of many subimages from many images, then the nuisance parameters α and x_{L_1} are unnecessary. The reason that they can be removed is that any helical object can be translated along its axis and rotated around its axis and remain a helical object that can be represented by the mathematics used in this document. However, the values of $d_{l,n,p}$ for the translated and rotated object will change (Eqs. 6.56 and 10.7). This approach can be employed for getting a fast and low resolution estimate from one image of a relatively straight long helical object.

CHAPTER 10

MEASURES OF PERFORMANCE

10.1 Fourier Shell Correlation (FSC)

A standard definition of resolution is based on the Fourier Shell Correlation (FSC) function [36, Eq. 2] [37, Eq. 17] [27, p. 879] [38] which compares the reciprocal-space scattering densities of two structures. Let $F^{\mathrm{a}}(\mathbf{k})$ and $F^{\mathrm{b}}(\mathbf{k})$ be the two reciprocal-space scattering densities to be compared. The FSC function [denoted by $p_{\mathrm{FSC}}(k)$] is a function of the magnitude of the reciprocal-space frequency vector (k) and is defined by

$$p_{\mathrm{FSC}}(k) \doteq \frac{\int F^{\mathrm{a}}(\mathbf{k}) \left[F^{\mathrm{b}}(\mathbf{k})\right]^* \mathrm{d}\Omega'}{\sqrt{\int |F^{\mathrm{a}}(\mathbf{k})|^2 \mathrm{d}\Omega' \int |F^{\mathrm{b}}(\mathbf{k})|^2 \mathrm{d}\Omega'}} \tag{10.1}$$

where $\mathrm{d}\Omega'$ is integration over the angles of spherical coordinates (i.e., $\int \mathrm{d}\Omega' = \int_{\phi'=0}^{2\pi} \int_{\theta'=0}^{\pi} \sin(\theta') \mathrm{d}\theta' \mathrm{d}\phi'$ where θ' and ϕ' are the angles of spherical coordinates in reciprocal space). Note that $p_{\mathrm{FSC}}(k)$ is real valued because $\rho(\mathbf{x})$ is real valued and that $|p_{\mathrm{FSC}}(k)| \leq 1$ by the Cauchy-Schwarz inequality. The two structures, $F^{\mathrm{a}}(\mathbf{k})$ and $F^{\mathrm{b}}(\mathbf{k})$, are often the reconstructions resulting from using even and odd numbered images, respectively. We also consider the case where $F^{\mathrm{b}}(\mathbf{k})$ is a known reciprocal-space cube. Once the FSC has been computed, the resolution is defined as the smallest value of k such that $p_{\mathrm{FSC}}(k)$ is less than a threshold which may depend on k [39].

Because of the periodicity in z, as is shown in Eq. 4.16, the reciprocal-space cube has the form

$$F(R, \psi, \zeta) = \sum_{l=-\infty}^{+\infty} F_l(R, \psi) \delta(l/c - \zeta). \tag{10.2}$$

Because of the δ functions, the integrals in Eq. 10.1 are not defined. Both to make the integrals in Eq. 10.1 well-defined and to evaluate their values, we define a discretized version of $F(R, \psi, \zeta)$ which has value $F_l(R, \psi)$ when the voxel contains $\zeta = l/c$ and has value 0 otherwise and use the discretized version in a numerical quadrature. An alternative approach would be to write $\rho'(\mathbf{x}) = \rho(\mathbf{x})w(x_3)$ where $w(\cdot)$ is a windowing function so that $F'(\mathbf{k}) = F(\mathbf{k}) * [\delta(k_1)\delta(k_2)W(k_3)]$ and use F' in FSC rather than F. This does not appear to be fundamentally better because, while the continuous $\mathbf{k}$ integrals would exist, they would still have to be done numerically.

We are not aware of a method to uniquely chose the coordinate system used to describe a helically-symmetric object by the mathematics used in this document. In particular, if such an object is rotated around the z axis by angle δ_φ and/or translated along the z axis by distance δ_z, it remains a helically-symmetric object that can be described by the same mathematics. However, the values of $d_{l,n,p}$ will change in accordance with Eq. 6.56. Let $\rho(\mathbf{x})$ be one density and $\rho'(\mathbf{x}) = \rho(r, \varphi - \delta_\varphi, z - \delta_z)$ be the second density. Let $d_{l,n,p}$ correspond to $\rho(\mathbf{x})$. Then

$$\begin{aligned} & d'_{l,n,p} \\ &= \int_{r=0}^{\infty} \frac{u\delta_{n,S_l}}{2\pi c} \int_{z'=0}^{c/u} \int_{\varphi'=0}^{2\pi} \rho'(r, \varphi', z') \exp\left[-i\left(n\varphi' + \frac{2\pi l}{c} z'\right)\right] \mathrm{d}\varphi' \mathrm{d}z' h_{n,p}(r) r \mathrm{d}r \qquad (10.3) \\ &= \int_{r=0}^{\infty} \frac{u\delta_{n,S_l}}{2\pi c} \int_{z'=0}^{c/u} \int_{\varphi'=0}^{2\pi} \rho(r, \varphi' - \delta_\varphi, z' - \delta_z) \exp\left[-i\left(n\varphi' + \frac{2\pi l}{c} z'\right)\right] \mathrm{d}\varphi' \mathrm{d}z' h_{n,p}(r) r \mathrm{d}r. \qquad (10.4) \end{aligned}$$

Change variables from φ' to $\varphi = \varphi' - \delta_\varphi$ and from z' to $z = z' - \delta_z$ to get

$$\begin{aligned} & d'_{l,n,p} \\ &= \int_{r=0}^{\infty} \frac{u\delta_{n,S_l}}{2\pi c} \int_{z=0}^{c/u} \int_{\varphi=0}^{2\pi} \rho(r, \varphi, z) \exp\left[-i\left(n(\varphi + \delta_\varphi) + \frac{2\pi l}{c}(z + \delta_z)\right)\right] \mathrm{d}\varphi \mathrm{d}z h_{n,p}(r) r \mathrm{d}r \qquad (10.5) \\ &= \exp\left[-i\left(n\delta_\varphi + \frac{2\pi l}{c}\delta_z\right)\right] \int_{r=0}^{\infty} \frac{u\delta_{n,S_l}}{2\pi c} \int_{z=0}^{c/u} \int_{\varphi=0}^{2\pi} \rho(r, \varphi, z) \exp\left[-i\left(n\varphi + \frac{2\pi l}{c} z\right)\right] \times \\ &\quad \times \mathrm{d}\varphi \mathrm{d}z h_{n,p}(r) r \mathrm{d}r \end{aligned}$$

$$= \exp\left[-i\left(n\delta_\varphi + \frac{2\pi l}{c}\delta_z\right)\right] d_{l,n,p}. \tag{10.7}$$

Therefore, when comparing an estimated value of $d_{l,n,p}$ with a standard value of $d_{l,n,p}$, denoted by $d^0_{l,n,p}$, it is first necessary to consider all possible variations in $d_{l,n,p}$. We quantify this comparison by defining a cost,

$$C(d_{l,n,p}, d^0_{l,n,p}, \delta_\varphi, \delta_z) = \sum_{l=-\infty}^{+\infty}\sum_{n=-\infty}^{+\infty}\sum_{p=1}^{+\infty}\left[d^0_{l,n,p} - \exp\left[-i\left(n\delta_\varphi + \frac{2\pi l}{c}\delta_z\right)\right] d_{l,n,p}\right]^2, \tag{10.8}$$

and determining the optimal variation by

$$\delta^0_\varphi, \delta^0_z = \underset{\delta_\varphi\in[0,2\pi),\delta_z\in[0,c/u)}{\arg\min}\, C(d_{l,n,p}, d^0_{l,n,p}, \delta_\varphi, \delta_z). \tag{10.9}$$

When computing the reciprocal-space 3-D cube for the reconstruction in preparation for computing FSC, the estimated values of $d_{l,n,p}$, u, v, and c are used in Eqs. 4.16 and 6.2. The period c is treated as a nuisance parameter in the maximum likelihood estimator that estimates $d_{l,n,p}$, u, and v. However, an estimate of c can be computed as a post processing operation [34].

10.2 Quadratic norm

The basis functions are orthonormal (Chapter 6.1), the Fourier transform definition (Eqs. 3.1 and 3.2) is unitary, and $\rho(\mathbf{x}) \in \mathbb{R}$. Therefore,

$$\int \rho^2(\mathbf{x})\mathrm{d}^3\mathbf{x} = \int |F(\mathbf{k})|^2\mathrm{d}^3\mathbf{k} = \sum_{l=-\infty}^{+\infty}\sum_{n=-\infty}^{+\infty}\sum_{p=1}^{\infty}|d_{l,n,p}|^2. \tag{10.10}$$

In the case where it is desired to compare two structures, both defined by $d_{l,n,p}$ coefficients and sharing the same values for r_1 and r_2, then by replacing ρ, F, and $d_{l,n,p}$ by $\rho^{\mathrm{a}} - \rho^{\mathrm{b}}$, $F^{\mathrm{a}} - F^{\mathrm{b}}$, and $d^{\mathrm{a}}_{l,n,p} - d^{\mathrm{b}}_{l,n,p}$, respectively, Eq. 10.10 provides an exact

and straightforward way to compute the squared quadratic norm of the difference between the two structures which is denoted by q^2.

CHAPTER 11

IMAGE PROCESSING

The cross correlation function can be used to select good images automatically, but since the number of images we have is of order 10^2, it is possible for us to do an interactive particle selection [40, Chapter 3 Section II]. First, images showing relatively good and straight helical objects are selected by examining the real-space 2-D images directly. Second, among those images, only the images which have relatively clean layer lines, determined by examining the reciprocal-space 2-D images directly, are used.

About 10^2 near-to-focus images were selected using the above method. Further preprocessing was then performed: first and second order sample statistics were computed by averging in areas outside the helical object. The assumption of zero mean pixel noise was achieved in practice by subtracting the mean from the data.

The period c is estimated as follows. First, each real-space 2-D image is transformed to reciprocal space by a 2-D fast Fourier transform (FFT). Second, the magnitude-squared of each reciprocal-space 2-D image is averaged in the κ_2 direction. Third, define the apparent period, $c_a = c \sin\beta \cos\gamma$. The inverse of the location of the maximum in the average determines the estimate of c_a, which is denoted by $\hat{c}_a$. Often the maximum does not occur at the first harmonic, e.g., in Figure 16.2 the maximum occurs at the third harmonic, so the relationship is $\hat{c}_a = \xi/\kappa_*$ where ξ is the order of the harmonic that has the maximum value and κ_* is the reciprocal space location of the maximum. Different images have different apparent periods due to different rotation angles β and γ while c is ideally the same for every object. With order 10^2 trials, it is likely that at least one value of β is quite close to $\pi/2$. We assume $\gamma = 0$ by previous alignment of the images. Since

$c \sin\beta \cos\gamma \leq c$, the maximum of the $\hat{c}_a$ values is taken to be the nominal period c_0. The nuisance parameter c has a uniform pdf centered at c_0. Notice that when c changes, the layer lines move. In particular, if c increases, the distance between two layer lines decreased, and vice versa.

The data y input to the EM algorithm is prepared by subdividing each image into subimages of size 128×128 pixels. Subimages are used instead of the original images to prevent the errors in an imperfect helix from accumulating over a long distance as was discussed in Chapter 8.1. Successive subimages do not overlap each other. Using nonoverlapping subimages differs from the methods other investigators [20, 21] use to create subimages. There are two reasons we decided not to overlap images in our approach. First, the helical symmetry is built into our approach so overlapping information is not required. Second, the noise model used in our approach includes the assumption that the additive pixel noise in different subimages is independent (Eq. 9.1).

Once the subimages are generated, the 2-D reciprocal data which the EM algorithm processes is generated in the following way. A 2-D FFT is performed to compute the reciprocal space image which contains the layer lines. The layer lines are separated by $1/(c \sin\beta \cos\gamma)$ with the 0th layer line at the origin of 2-D reciprocal space. The spatial frequency variable κ_1 is discretized. The numerical integral over the nuisance parameter z_i includes integrals over c, β and γ. Therefore $c_a = c \sin\beta \cos\gamma$ changes. As c_a changes, the software changes the location of the layer lines in the reciprocal space image. In particular, the three columns of pixels (a column has fixed κ_1 and varying κ_2 values) closest to the layer line location l/c_a are only pixels included in the data y_i. (Eq. 9.1).

CHAPTER 12

TOBACCO MOSAIC VIRUS (TMV) AND THE CHOICE OF CONTRAST TRANSFER FUNCTION (CTF) AND OTHER PARAMETERS

Tobacco Mosaic Virus (TMV) has been studied because TMV has been much investigated (e.g., [21]) and because an atomic resolution structure of the motif is known [11]. The helical parameters for TMV are [11] $u_{\mathrm{TMV}} = 49$, $v_{\mathrm{TMV}} = 3$, and $c_{\mathrm{TMV}} = 69$Å and the helix has one start (so there is no additional symmetry of the C_μ or D_μ type). There are $N_{\mathrm{TMV}} = 1354$ [11] non-hydrogen atoms in the motif structure. Let the N_{TMV} atomic scattering intensities and cylindrical coordinates be denoted by f_j and $\mathbf{x}_j = (r_j, \varphi_j, z_j)$, respectively.

110 images of TMV each measuring roughly 128×1300 pixels at sampling interval 2.263Å were kindly provided by Prof. Bridget Carragher (The Scripps Research Institute). Because the experimental TMV images have CTFs that can be approximated by the parameter values described in Table 12.1, these values have been used in all forward and inverse calculations.

Table 12.1: CTF parameters: Δf is the deviation from Gaussian focus, C_s is the coefficient of spherical aberration, λ is the electron wavelength, F_{amp} is the fractional amplitude contrast, and B is the decay.

	parameter	value
CTF	Δf	0.7×10^4Å
	C_s	2.0×10^7Å
	λ	0.0336Å
	F_{amp}	0.2
	B	100Å^2

Based on the dimensions of the TMV particle, all calculations described in this document use the basis functions of Chapter 6.1.2 with values $r_1 = 20$Å and $r_2 = 90$Å.

CHAPTER 13

PRACTICAL ISSUES FOR ALL RECONSTRUCTION CALCULATIONS

As in many other structural biology reconstruction algorithms, the resolution of the reconstruction is increased as the computation progresses. In the algorithm of this paper, resolution is increased in a series of steps where the number of d coefficients used in a step increases from the number used in the previous step as is described in Table 13.1.

The expectation maximization algorithm is an iterative algorithm and therefore each step requires an initial condition. Because it is also a local optimization algorithm, multiple initial conditions are tested and the best (in the sense of log likelihood) of the answers are taken as the source of the initial conditions for the subsequent step. In the final step, the answer with the highest log likelihood is taken as the final answer of the complete algorithm.

A Step 0 which is not described in Table 13.1 is used to start the calculation. First, use a model with only $d_{l=0,n=0,p=1}$ and determine the value of $d_{l=0,n=0,p=1}$ by least squares. Second, use a model of the size described for Step 1 in Table 13.1. Initialize the model with all 0s except for $d_{l=0,n=0,p=1}$ which takes the value determined by least squares. Use this model as the initial condition for the EM algorithm and iterate until convergence is achieved. The resulting model and 499 random perturbations of that model are the $N_{\text{ic}} = 500$ initial conditions for Step 1. When transitioning from Step i to Step $i+1$, the best 3 results from the earlier step are saved. The saved results are augmented with 0s and used as initial conditions. These initial conditions are also random perturbed to generate additional initial conitions for the later step.

Table 13.1: Truncation limits ($l_{\max}$, $n_{\max}$, and $p_{\max}$) at each step of the algorithm and the resulting number of $d_{l,n,p}$ coefficients (N_d). The numbers of random initial conditions used at each step are denoted by N_{ic} which are also tabulated. As is illustrated in Table 4.1, the allowed n are not nearly all n. In fact, for the case of $(u, v) = (49, 3)$, the choice of $n_{\max} = 49$ leads to 2 values of n for each $l \neq 0$ and three values of n for $l = 0$ which are $n \in \{-49, 0, +49\}$. But, since $\rho(\mathbf{x}) \in \mathbb{R}$, there is the constraint $g^*_{-n,-l}(r) = g_{n,l}(r)$ (Eq. 4.93) which implies $g_{-n,l=0}(r) = g^*_{n,l=0}(r)$. Therefore $g_{n=-49,l=0}(r) = g^*_{n=49,l=0}(r)$ so the $(n = -49, l = 0)$ term is determined by the $(n = 49, l = 0)$ term. Therefore, there are only 2 independent terms for $l = 0$ exactly as there are 2 independent terms for $l \neq 0$.

step	$l_{\max}$	$n_{\max}$	$p_{\max}$	N_d	N_{ic}
1	7	25	1	15	500
2	7	49	1	31	300
3	7	49	5	155	10
4	7	49	10	310	4

The EM algorithm is iterative and therefore requires a convergence test. We use the same test that was used in Ref. [29]. In particular, the EM algorithm is stopped if the l^1-norm of the difference between the weights d at the previous and current iterations normalized by the average of the l^1-norms of the weight at the previous and current iterations is less than 10^{-5}.

The optimization of the log likelihood could be done over all relatively prime pairs of u and v. However, given some knowledge of the size of the motif and the radius of the helix, considering all relatively prime pairs of u and v is wasteful of computation since many (u, v) pairs lead to impossible packing of the motifs. Based on such considerations [1], a feasible set of reduced size is used as is enumerated in Table 13.2.

For computing synthetic 3-D cubes and 2-D images and for computing reconstructions, the various infinite summations must be truncated. Let the integers $l_{\max}$, $n_{\max}$, and $p_{\max}$ describe the truncations used by the reconstruction algo-

Table 13.2: Feasible set for the optimization of (u, v).

u	v
41	3
43	3
44	3
46	3
47	3
49	3
50	3
52	3
53	3
55	3
55	4
56	3
57	4
58	3
59	3
59	4
61	3
61	4
63	4
65	4
67	4
68	5
69	4
71	4
73	4
75	4
77	4
79	4
81	4

rithm of the three infinite sums in Eq. 6.9. Similarly, the integers $l_{\max}^{\mathrm{TMV}}$, $n_{\max}^{\mathrm{TMV}}$, and $p_{\max}^{\mathrm{TMV}}$ describe the truncations used in generating synthetic TMV images and comparing reconstructions with the PDB reconstruction. Typically, $l_{\max} \leq l_{\max}^{\mathrm{TMV}}$, $n_{\max} \leq n_{\max}^{\mathrm{TMV}}$, and $p_{\max} \leq p_{\max}^{\mathrm{TMV}}$.

In several equations, e.g., Eqs. 5.13 and 5.24, the arctan function that is indicated in the equation is replace by the `atan2` function in the software.

To get a resolution of 10Å, 8 layer lines including the 0th layer line must be estimated. For each layer line, two Bessel terms are necessary and sufficient to get a resolution of 6-7Å [9]. With up to the 7th layer line estimated, the resolution we can possibly obtain would be $\frac{7}{69}$Å $\approx \frac{1}{10}$Å [17].

CHAPTER 14

CALCULATION OF SYNTHETIC IMAGES

Two methods have been developed for computing synthetic images from the known atomic resolution structure of TMV.

14.1 PDB atomic locations to d coefficients to synthetic images

The first way in which to compute synthetic reciprocal-space images and cubes is to use an impulsive mathematical model for the electron scattering intensity, i.e.,

$$\rho_{\mathrm{TMV}}(\mathbf{x}) \;=\; \sum_{j=1}^{N_{\mathrm{TMV}}} f_j \delta(\mathbf{x}-\mathbf{x}_j), \tag{14.1}$$

evaluate the d coefficients by Eq. 6.57 for $l \in \{-l_{\max}^{\mathrm{TMV}},\ldots,l_{\max}^{\mathrm{TMV}}\}$, $n \in \{-n_{\max}^{\mathrm{TMV}},\ldots,n_{\max}^{\mathrm{TMV}}\}$, and $p \in \{1,\ldots,p_{\max}^{\mathrm{TMV}}\}$, and then use Eqs. 5.60 and 6.2 to compute a reciprocal-space windowed 2-D image or Eqs. 4.16 and 6.2 to compute a reciprocal-space 3-D cube. To compute a reciprocal-space image it is also necessary to choose nuisance parameters. When computing a set of images, the values of the nuisance parameters α, β, γ, x_{L_1}, and x_{L_2} were set as independent realizations of pseudo random variables drawn from the pdfs described in Chapter 8.1. For the nuisance parameter c, the value was set to c_{TMV} for all images., i.e., the pdf is $\delta(c-c_{\mathrm{TMV}})$ and there is no distinction between using one realization for all images and using independent realizations for each image. Let the signal variance in the ith image be denoted by $\sigma_s^2(i)$ and defined by

$$\sigma_s^2(i) = \frac{1}{N_y}\sum_{n=1}^{N_y}\left(y_i(n) - \frac{1}{N_y}\sum_{n=1}^{N_y} y_i(n)\right)^2 \tag{14.2}$$

where $y_i(n)$ is the nth pixel of the ith image. Independently for each image, the ith noisy image is the ith noise-free image plus additive zero-mean white Gaussian noise with variance $\sigma_s^2(i)/\text{SNR}$ where a variety of values for SNR are considered.

14.2 PDB atomic locations to synthetic images directly

The second way in which to compute synthetic reciprocal-space images and cubes is to use an impulsive mathematical model for the electron scattering intensity, i.e.,

$$\rho_{\text{TMV}}(\mathbf{x}) \quad = \quad \sum_{j=1}^{N_{\text{TMV}}} f_j \delta(\mathbf{x} - \mathbf{x}_j), \tag{14.3}$$

and apply Eq. 4.63 to compute a reciprocal-space 3-D cube or Eq. 5.61 to compute a reciprocal-space windowed 2-D image. This amounts to the case of $p_{\text{max}}^{\text{TMV}} = \infty$. All other processing is identical to the processing described in Section 14.1.

CHAPTER 15

NUMERICAL RESULTS BASED ON SYNTHETIC IMAGES

Figure 15.1 gives an overview of the entire algorithm which is used in this section on synthetic images and in the following section on experimental images.

Using the method of Section 14.1, a total of 64 images each measuring 128×128 pixels with sampling interval $\Delta = 2.2$Å were computed with independent realizations of the nuisance parameters α, β, γ, x_{L_1}, and x_{L_2} and the additive pixel noise for each image and the same value of nuisance parameter $c = c_{\mathrm{TMV}}$ for all images. There was no partitioning of an image into subimages: there is one subimage per image and the subimage is identical to the image. The sampling interval and subimage size are the same as in the experimental TMV images (Chapter 12). The values at which the infinite sums were truncated in the computing of the images and the computing of the reconstructions were the same (i.e., the calculations were matched) and had values (Table 13.1) $l_{\max}^{\mathrm{TMV}} = l_{\max} = 7$, $n_{\max}^{\mathrm{TMV}} = n_{\max} = 49$, and $p_{\max}^{\mathrm{TMV}} = p_{\max} = 10$. Two SNR values were considered, specifically, 1.0 and 0.2.

Two natural ways in which to compute FSC are to compare the reciprocal-space 3-D cube from the reconstruction with the reciprocal-space 3-D cube computed from Eq. 4.16 with either (1) $G_{n,l}(R)$ computed from Eq. 6.2 using the same number of $d_{l,n,p}$ coefficients (i.e., $l_{\max}^{\mathrm{TMV}}$, $n_{\max}^{\mathrm{TMV}}$, and $p_{\max}^{\mathrm{TMV}}$) as were used to compute the reconstruction and using the values of the $d_{l,n,p}$ coefficients computed from the PDB structure of TMV by Eq. 6.57 or (2) $G_{n,l}(R)$ computed from Eq. 4.61, i.e., directly from the atomic scattering factors and locations, using the same values of $l_{\max}^{\mathrm{TMV}}$ and $n_{\max}^{\mathrm{TMV}}$ as where used in computing the images. Calculations of the first type are referred to as matched-FSC and calculations of the second type are referred to as direct-FSC. A third natural way is to divide the set of images into

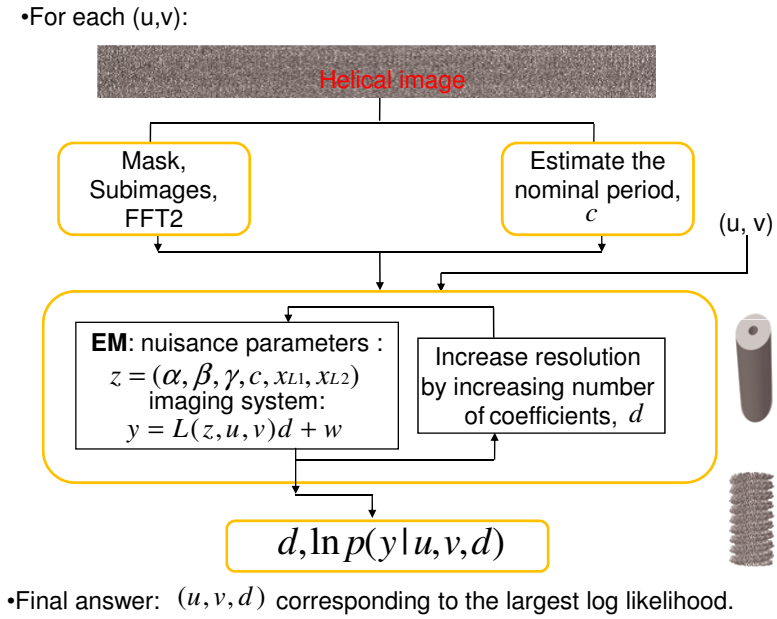

Figure 15.1: Overview.

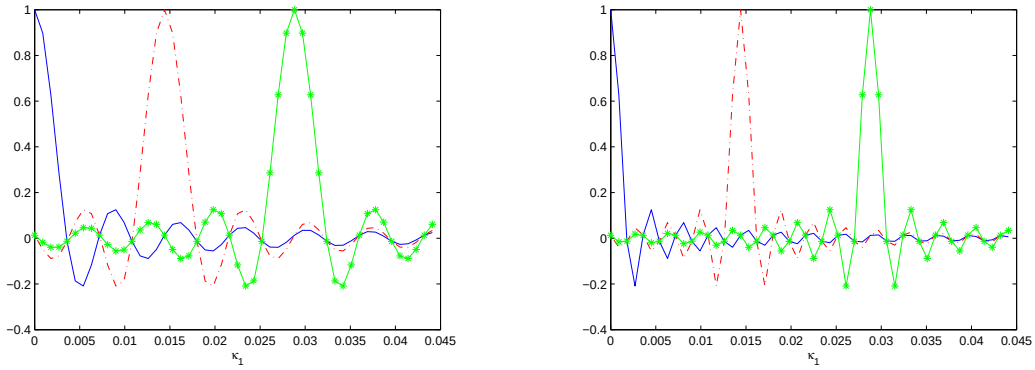

128 × 128 pixel subimage

128 × 256 pixel subimage

Figure 15.2: The shifted sinc functions for the $l \in \{0, 1, 2\}$ layer lines indicating the amount of layer line broadening due to windowing of the images.

two equal-sized subsets, typically the even and the odd numbered images, and compute the FSC between a reconstruction based on the even number images and a reconstruction based on the odd numbered images. This third method is the method typically used when the true structure is unknown and is referred to as even/odd-FSC. In this document, the third method is used only for the experimental TMV images.

15.1 Determination of the effect of the windowing

The windowing introduces a broadening of the layer lines. If the broadening is too great, then the layer lines will overlap. Figure 15.2 shows a plot of the shifted sinc functions that result from the windowing for the lowest three layer lines, i.e., for $l \in \{0, 1, 2\}$, versus κ_1. Because the three sinc functions do not greatly overlap, the broadened layer lines will not greatly overlap.

Table 15.1: Integration rules for nuisance parameters. Note also Table 8.1.

nuisance parameter	integration rule type	number of abscissas
α	uniform	150
β	Gauss-Legendre	7
γ	Gauss-Legendre	1
c	Gauss-Legendre	1
x_{L_1}	Gauss-Legendre	3
x_{L_2}	Gauss-Legendre	10

15.2 Determination of the number of abscissas in the nuisance parameter integration rules

The necessary number of abscissas in the integration rules used in the expectation step of the expectation maximization algorithm for integrating the nuisance parameters was investigated by holding all but one nuisance parameter at its true value and computing the log likelihood with a variety of integration rules for the remaining nuisance parameter. Plots of log likelihood versus number of abscissas for each of the nuisance parameters is shown in Figure 15.3. The result is the integration rules listed in Table 15.1.

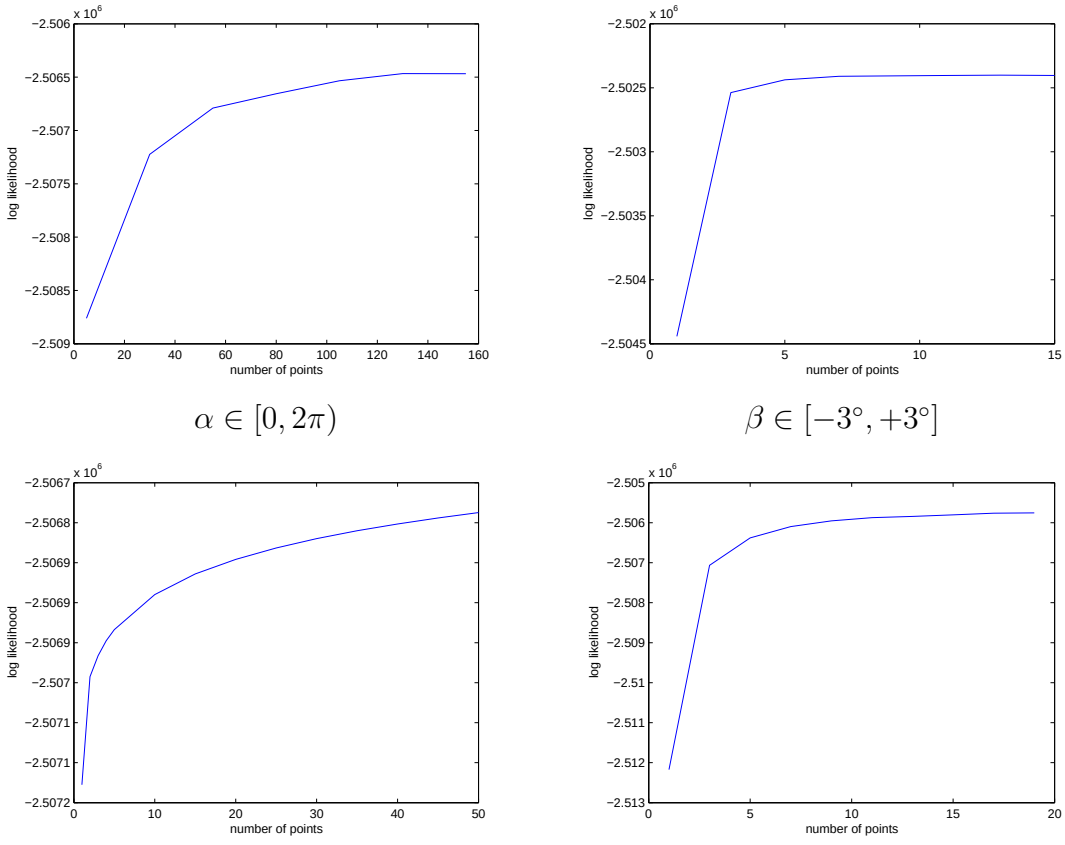

$\alpha \in [0, 2\pi)$ $\beta \in [-3°, +3°]$

$x_{L_1} \in [0, c/u)$ $x_{L_2} \in [-5, +5]$ pixels

Figure 15.3: The log likelihood as a function of the number of abscissas in the integration rule for one nuisance parameter when the other nuisance parameters are held constant at their true values.

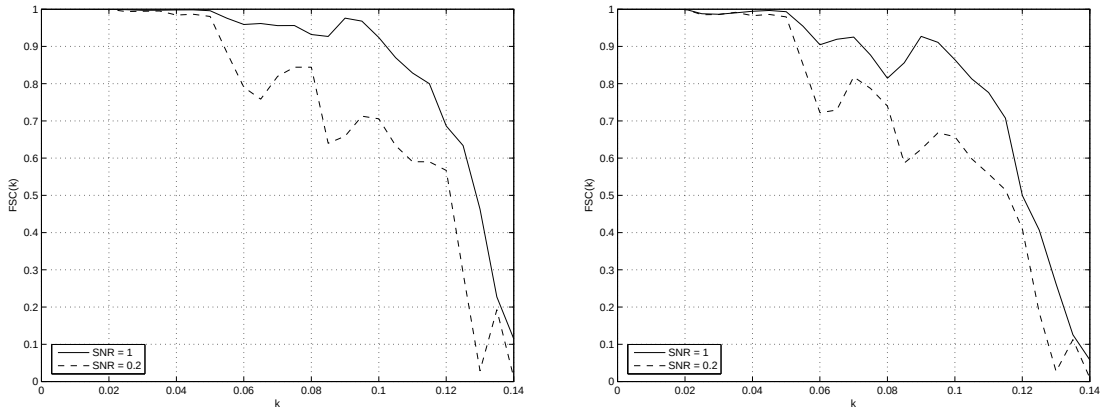

matched-FSC direct-FSC

Figure 15.4: FSC curves for reconstruction calculations using 64 images and two different SNRs. Both matched-FSC and direct-FSC calculations are shown illustrating that the difference between the two types is small.

15.3 Resolution via FSC as a function of SNR and the similarity of the two FSC comparisons

The resolution achieved should increase as the SNR increases. As is shown by the FSC curves plotted in Figure 15.4 for the case of 64 images, that behavior occurs as expected. Figure 15.4 shows both matched-FSC and direct-FSC calculations and the differences are small. For that reason, the remainder of the FSC calculations described in this document are of the direct-FSC type unless otherwise specified.

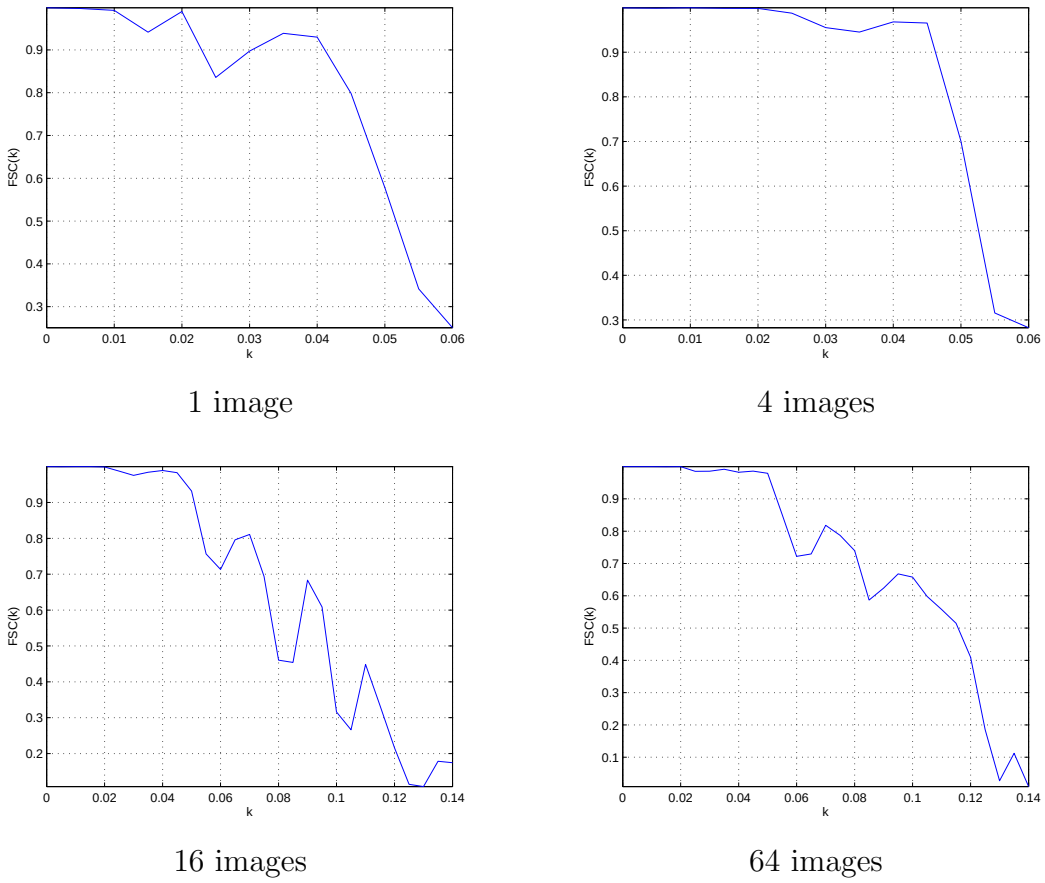

Figure 15.5: Matched-FSC curves for reconstruction calculations using SNR 0.2 and a variety of number of images. Note the different ranges of k in each plot.

15.4 Resolution via FSC as a function of number of images

The resolution achieved should increase as the number of images used increases. As is shown by the FSC curves plotted in Figure 15.5 for the case of SNR 0.2, that behavior occurs as expected.

15.5 Coefficients and reconstructions as a function of iteration

At each resolution step, the expectation-maximization algorithm is an iterative algorithm. Using 64 images and SNR 0.2, Figure 15.6 shows the evolution of $d_{l,n,p}$ for the selected values of l, n, and p at the highest resolution step (Table 13.1) which uses $l_{\max} = 7$, $n_{\max} = 49$, $p_{\max} = 10$ resulting in $N_d = 310$ coefficients. Both Figure 15.6 and Table 15.2 show the values for the same selected $d_{l,n,p}$ computed by Eq. 6.57 for comparison. Figure 15.7 shows the change of the real-space 3-D cube from the initial to the final iteration for the same calculation.

15.6 Ability to determine the correct values of u and v

All of the previous calculations were done with the correct values of u and v, specifically, $u = 49$ and $v = 3$. In Table 15.3 is shown the rank-ordered list of log likelihood values as a function of the assumed value of u and v for a reconstruction problem with 64 subimages at SNR values 0.2 and 1.0. The estimated values are the correct values. The SNR 0.2 data from Table 15.3 are plotted in Figure 15.8. These plots make clearer the absence of ambiguity in the estimate of v and the presence of ambiguity in the estimate of u, where the estimator is ambiguous about $u \in \{43, 49, 55\}$ which is every 6th integer corresponding to insertion or deletion of pair of motifs from each of the three turns of one period of the $v = 3$ helical symmetry.

Table 15.2: Comparison of selected estimated $d_{l,n,p}$ at Iteration 0 - 5 at Step 4 against the true $d_{l,n,p}$ that are derived from the PDB. The total number of $d_{l,n,p}$ is 310 (Table 13.1). For cases in which l is non-zero, both the real and imaginary part of the coefficients are estimated and the real part is listed before the imaginary part in the table.

0	1	2	3	4	5	PDB	l	n	p
23.8163	23.724	23.7239	23.7239	23.7239	23.7239	23.7829	0	0	1
2.20021	2.33195	2.33194	2.33194	2.33194	2.33194	2.39091	0	0	2
0.537217	0.712254	0.712244	0.712247	0.712248	0.712249	0.644081	0	0	3
2.72175	3.06445	3.06443	3.06443	3.06443	3.06443	3.06768	0	0	4
-0.958153	-0.78198	-0.78198	-0.78198	-0.78197	-0.78197	-0.7157	0	0	5
-0.962662	-1.17696	-1.17719	-1.1772	-1.1772	-1.1772	-1.04362	3	1	1
0.945372	1.10446	1.10396	1.1039	1.10388	1.10389	1.05668	3	1	2
-1.02869	-1.23776	-1.23699	-1.23689	-1.23687	-1.23687	-1.12306	3	1	3
-0.0486221	-0.05711	-0.05778	-0.05787	-0.05789	-0.05789	-0.01252	3	1	4
0.907487	0.778129	0.778825	0.778914	0.778929	0.77893	0.679688	3	1	5
2.00293	1.90189	1.90224	1.90228	1.9023	1.90229	1.92453	3	1	1
-1.47361	-1.37867	-1.37795	-1.37786	-1.37784	-1.37785	-1.45844	3	1	2
1.27137	1.15497	1.15413	1.15403	1.15401	1.15401	1.27026	3	1	3
0.795841	0.802666	0.803647	0.803766	0.803787	0.803786	0.80188	3	1	4
-1.5948	-1.56273	-1.56325	-1.56331	-1.56332	-1.56332	-1.62282	3	1	5
1.10717	0.855538	0.854809	0.854297	0.854135	0.85408	0.920829	6	2	1
-1.21512	-1.07563	-1.07727	-1.07724	-1.07718	-1.07721	-0.95605	6	2	2
0.427031	0.5017	0.496338	0.495894	0.495838	0.495831	0.875235	6	2	3
0.677793	0.424208	0.427146	0.427113	0.427012	0.427018	1.20115	6	2	4
-0.185935	-0.27936	-0.28476	-0.2856	-0.28583	-0.28586	-0.55443	6	2	5
1.37396	1.54002	1.54105	1.54091	1.54086	1.54084	1.42681	6	2	1
-0.578738	-0.72657	-0.72202	-0.7213	-0.72117	-0.72113	-0.57811	6	2	2
-0.0122239	0.114931	0.112888	0.112612	0.11254	0.112557	-0.05289	6	2	3
1.36882	1.43885	1.4506	1.45181	1.45205	1.45206	1.71484	6	2	4
0.0907919	0.216545	0.204593	0.20283	0.202526	0.202516	0.427629	6	2	5

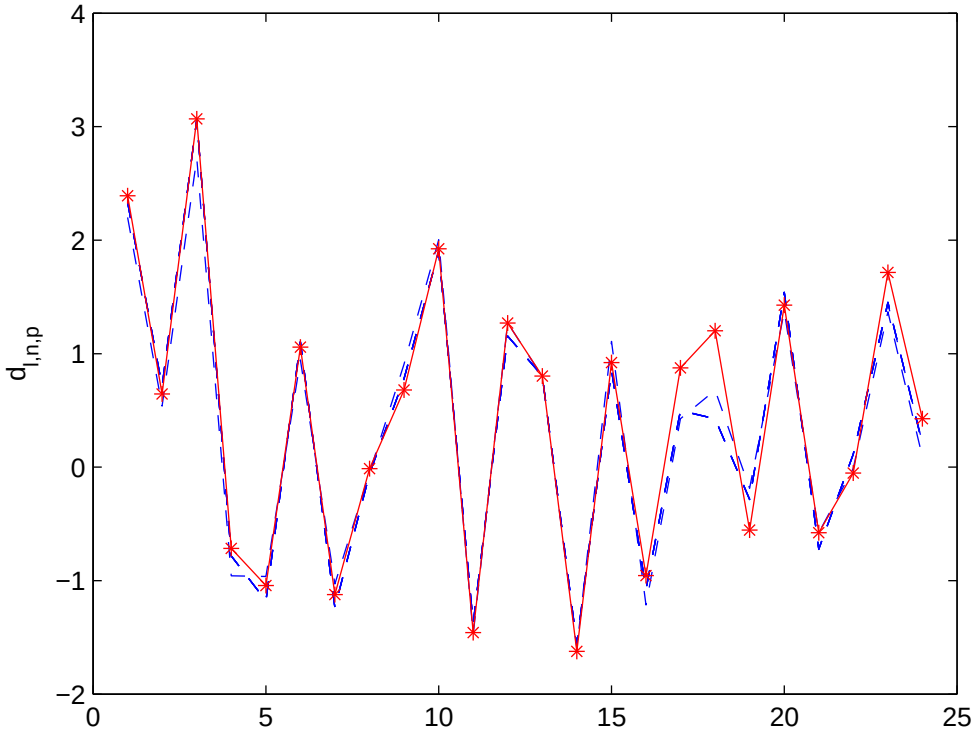

Figure 15.6: Evolution of $d_{l,n,p}$ for the selected values of l, n, and p used in Table 15.2 (with the exception of $(l, n, p) = (0, 0, 1)$) at Step 4 (Table 13.1). The red curve with star markers is the truth from PDB. The various blue dashed curves, which are mostly superimposed, show values of estiamted $d_{l,n,p}$ at Iteration 0 - 5. Convergence is rapid and accurate for lower indexed $d_{l,n,p}$ and slower and less accurate for higher indexed $d_{l,n,p}$.

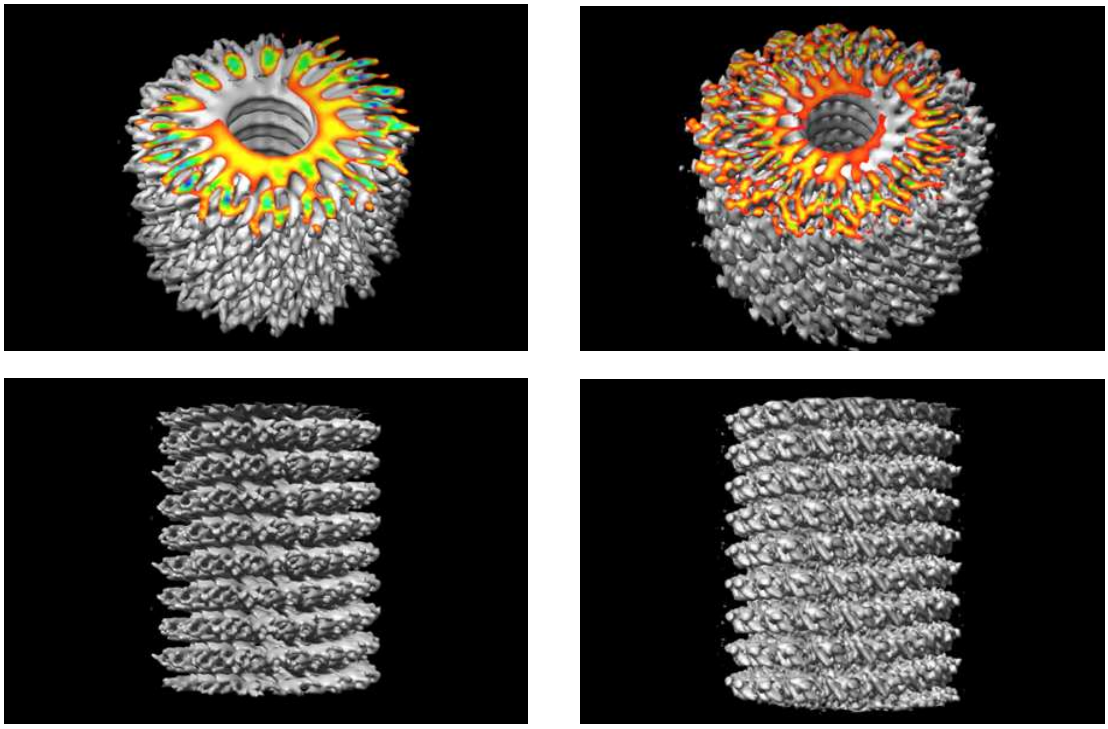

initial final

Figure 15.7: Change of the real-space 3-D cube from the initial to the final iteration of the calculation for which the evolution of $d_{l,n,p}$ is shown in Figure 15.6 and Table 15.2.

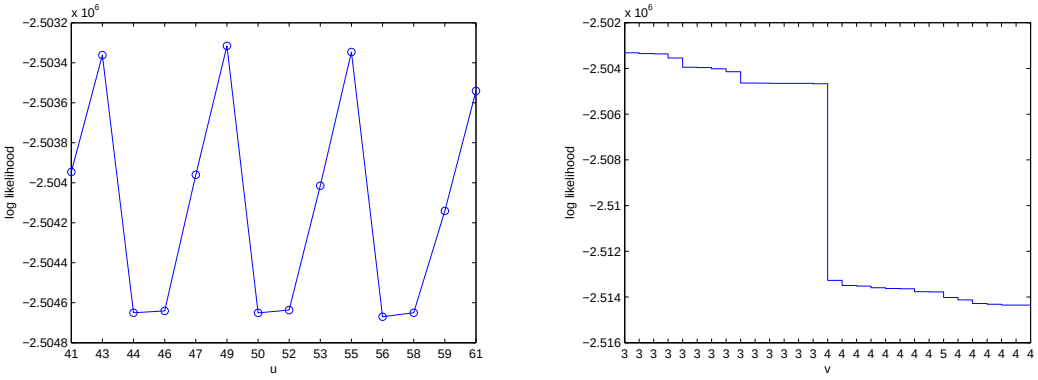

Figure 15.8: Plots of the SNR 0.2 log likelihood values from Table 15.3. Panel (a): The log likelihood values as a function of u for the case $v = 3$. In order to get the correct u, a high resolution reconstruction is required, otherwise, as shown in the plot, the estimated u is likely to be a multiple of 2 motifs per turn different from the true answer. Panel (b): The log likelihood values as a function of v showing that $v = 3$ has a substantially higher likelihood than $v = 4$ or $v = 5$.

However, with fewer images, the correct values of u and v are not always chosen. In Table 15.4 is shown the rank-ordered list of log likelihood values as a function of the assumed value of u and v for a reconstruction problem at SNR 0.2 with 1, 4, 16, or 64 subimages. Only the calculation with 64 images yields the correct estimate for u and v.

Table 15.3: Rank-ordered list of log likelihood values as a function of the assumed value of u and v for 64 images and SNR values 0.2 and 1.0. The correct values are $u = 49$ and $v = 3$. $\mathcal{Q}$ indicates the natural logarithm of the likelihood defined in Eq. 9.2.

SNR 0.2			SNR 1.0		
u	v	$\mathcal{Q}$	u	v	$\mathcal{Q}$
49	3	-2503315	49	3	-2093496
55	3	-2503346	55	3	-2093638
43	3	-2503362	43	3	-2093668
61	3	-2503541	61	3	-2094633
41	3	-2503946	41	3	-2096605
47	3	-2503961	47	3	-2096739
53	3	-2504015	53	3	-2096988
59	3	-2504141	59	3	-2097601
52	3	-2504637	52	3	-2099929
46	3	-2504641	46	3	-2099940
58	3	-2504650	58	3	-2099950
44	3	-2504650	44	3	-2100168
50	3	-2504651	50	3	-2100179
56	3	-2504670	56	3	-2100187
55	4	-2513270	55	4	-2143029
63	4	-2513495	63	4	-2144218
57	4	-2513522	57	4	-2144291
65	4	-2513596	65	4	-2144816
71	4	-2513626	71	4	-2144913
73	4	-2513640	73	4	-2144999
79	4	-2513767	79	4	-2145573
81	4	-2513776	81	4	-2145688
68	5	-2514022	68	5	-2147031
59	4	-2514125	59	4	-2147433
61	4	-2514286	61	4	-2148238
67	4	-2514319	67	4	-2148246
69	4	-2514354	69	4	-2148492
75	4	-2514355	75	4	-2148570
77	4	-2514361	77	4	-2148592

Table 15.4: Rank-ordered list of log likelihood values as a function of the assumed value of u and v for SNR value 0.2 and 1, 4, 16, and 64 images. The correct values are $u = 49$ and $v = 3$. $\mathcal{Q}$ indicates the natural logarithm of the likelihood defined in Eq. 9.2.

64 images			16 images			4 images			1 image		
u	v	$\mathcal{Q}$	u	v	$\mathcal{Q}$	u	v	$\mathcal{Q}$	u	v	$\mathcal{Q}$
49	3	-2503315	55	3	-625470	55	3	-156411	56	3	-38874
55	3	-2503346	49	3	-625477	49	3	-156417	50	3	-38877
43	3	-2503362	43	3	-625481	43	3	-156421	49	3	-38882
61	3	-2503541	61	3	-625529	61	3	-156425	47	3	-38883
41	3	-2503946	41	3	-625625	50	3	-156444	44	3	-38883
47	3	-2503961	47	3	-625639	41	3	-156447	53	3	-38884
53	3	-2504015	53	3	-625641	56	3	-156450	59	3	-38885
59	3	-2504141	59	3	-625676	47	3	-156451	55	3	-38885
52	3	-2504637	58	3	-625771	44	3	-156453	41	3	-38886
46	3	-2504641	46	3	-625774	52	3	-156453	61	3	-38888
58	3	-2504650	52	3	-625775	53	3	-156457	52	3	-38890
44	3	-2504650	50	3	-625781	46	3	-156457	58	3	-38891
50	3	-2504651	44	3	-625782	58	3	-156462	46	3	-38891
56	3	-2504670	56	3	-625789	59	3	-156465	43	3	-38891
55	4	-2513270	55	4	-627958	63	4	-156991	68	5	-39012
63	4	-2513495	57	4	-628022	55	4	-156991	57	4	-39020
57	4	-2513522	63	4	-628023	71	4	-157004	71	4	-39025
65	4	-2513596	65	4	-628035	73	4	-157005	59	4	-39027
71	4	-2513626	71	4	-628041	57	4	-157006	73	4	-39027
73	4	-2513640	73	4	-628042	65	4	-157007	55	4	-39030
79	4	-2513767	79	4	-628064	81	4	-157016	65	4	-39032
81	4	-2513776	81	4	-628075	79	4	-157025	61	4	-39032
68	5	-2514022	68	5	-628127	68	5	-157035	63	4	-39033
59	4	-2514125	67	4	-628169	75	4	-157040	75	4	-39033
61	4	-2514286	75	4	-628186	67	4	-157041	69	4	-39037
67	4	-2514319	61	4	-628190	77	4	-157044	77	4	-39037
69	4	-2514354	59	4	-628193	59	4	-157057	79	4	-39039
75	4	-2514355	69	4	-628195	61	4	-157062	67	4	-39039
77	4	-2514361	77	4	-628199	69	4	-157063	81	4	-39046

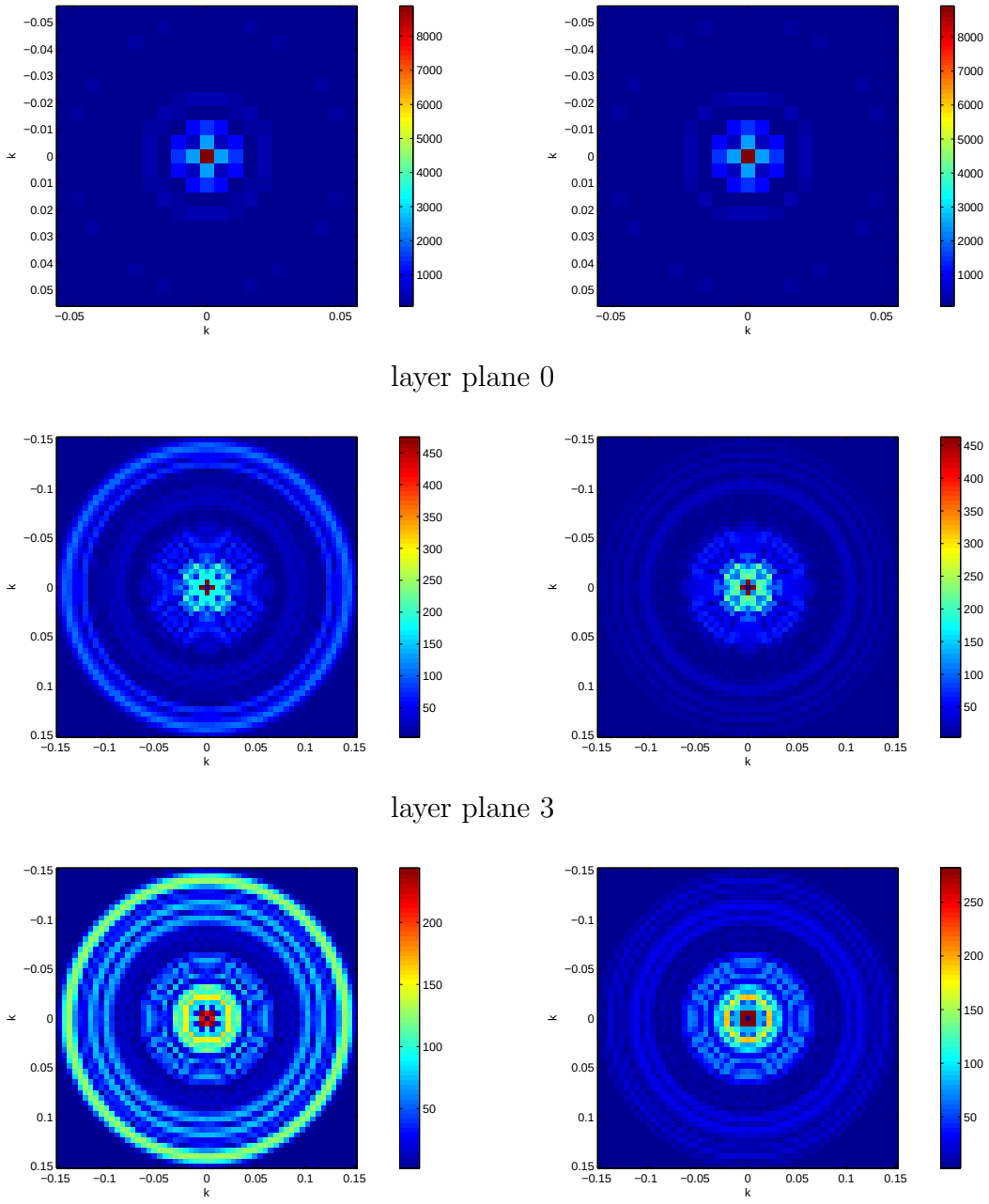

Figure 15.9: Layer planes shown as images: Column (a): The reconstruction from 64 images at SNR 0.2. Column (b): The planes computed from the PDB which would be used in a matched-FSC calculation.

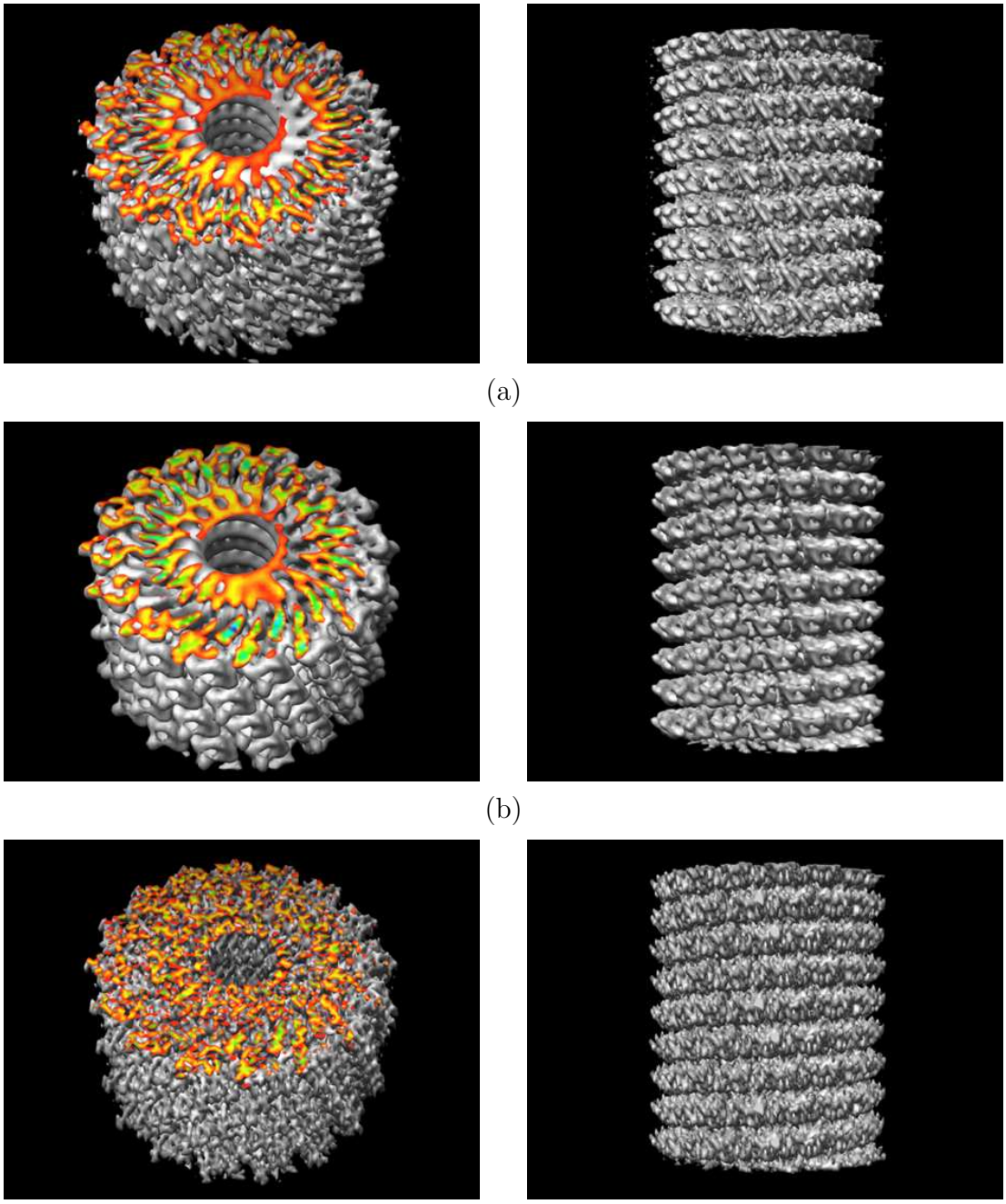

Figure 15.10: Surface renderings by UCSF Chimera [4]. Row (a): The reconstruction from 64 images at SNR 0.2. Row (b): The cube that results from the planes computed from PDB which would be used in a matched-FSC calculation. Row (c): The cube that results from the planes computed from PDB which would be used in a direct-FSC calculation.

15.7 Comparison with PDB for 64 images and SNR 0.2

Figures 15.9 and 15.10 compare the reconstruction from 64 synthetic images at SNR 0.2 with the PDB structure. Figure 15.9 shows three of the layer planes while Figure 15.10 shows the real-space 3-D cubes.

CHAPTER 16

NUMERICAL RESULTS BASED ON EXPERIMENTAL IMAGES

Figure 16.1 shows one experimental image as it progresses through the preprocessing. First the image is masked, then it is broken up into subimages, and then each subimage is transformed to reciprocal space.

16.1 Determination of the period

For one example image, Figure 16.2 shows the curve from which the estimate of the apparent period, $\hat{c}_a$, is determined. As discussed in Chapter 11, the curve is the average of the magnitude-squared over the discretized κ_2 variable of the 2-D FFT of the real space image. Note that the value of $\hat{c}_a$ is not ambiguous.

The stated sampling interval for the experimental images of TMV is 2.263Å. The published value for the period c of TMV is 69Å. All $\hat{c}_a$ values, one for each image, are listed in Table 16.1. Note that most exceed 69Å. One explanation is an inaccuracy in the sampling interval. In particular, if the sampling interval is reduced from 2.263Å to 2.2Å then the largest value of $\hat{c}_a$, 70.984Å, would be reduced to 69.008Å which is the published value. Therefore, in all calculations with both synthetic and experimental images, we have used a sampling interval of 2.2Å.

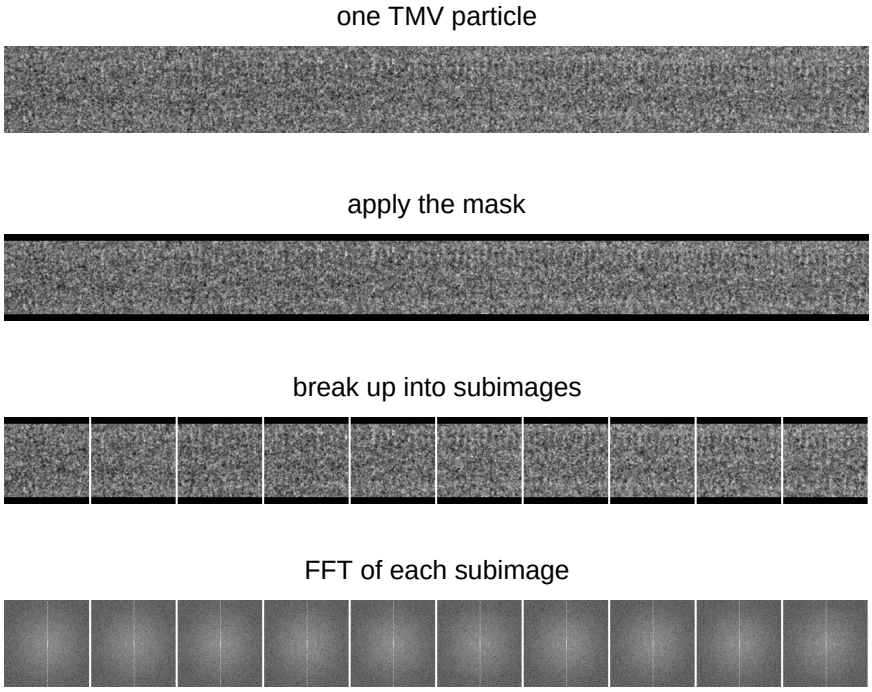

Figure 16.1: Preprocessing of one experimental image.

Table 16.1: A rank-ordered list of the estimated apparent period $\hat{c}_a$ in Å for the 110 experimental images of TMV.

69.003	69.297	69.485	69.609	69.757	69.935	70.072	70.263	70.482	70.654
69.061	69.311	69.498	69.656	69.803	69.947	70.096	70.296	70.497	70.672
69.093	69.375	69.521	69.666	69.82	69.947	70.104	70.338	70.521	70.673
69.104	69.388	69.548	69.679	69.82	69.988	70.123	70.344	70.521	70.682
69.114	69.405	69.551	69.697	69.822	69.995	70.153	70.359	70.53	70.728
69.147	69.408	69.554	69.7	69.859	70.017	70.153	70.374	70.551	70.784
69.163	69.416	69.559	69.707	69.88	70.024	70.182	70.397	70.563	70.815
69.17	69.438	69.573	69.722	69.899	70.038	70.185	70.463	70.568	70.826
69.248	69.447	69.587	69.725	69.902	70.055	70.195	70.465	70.606	70.829
69.27	69.465	69.598	69.742	69.905	70.058	70.203	70.471	70.645	70.86
69.275	69.472	69.608	69.754	69.927	70.062	70.258	70.476	70.65	70.984

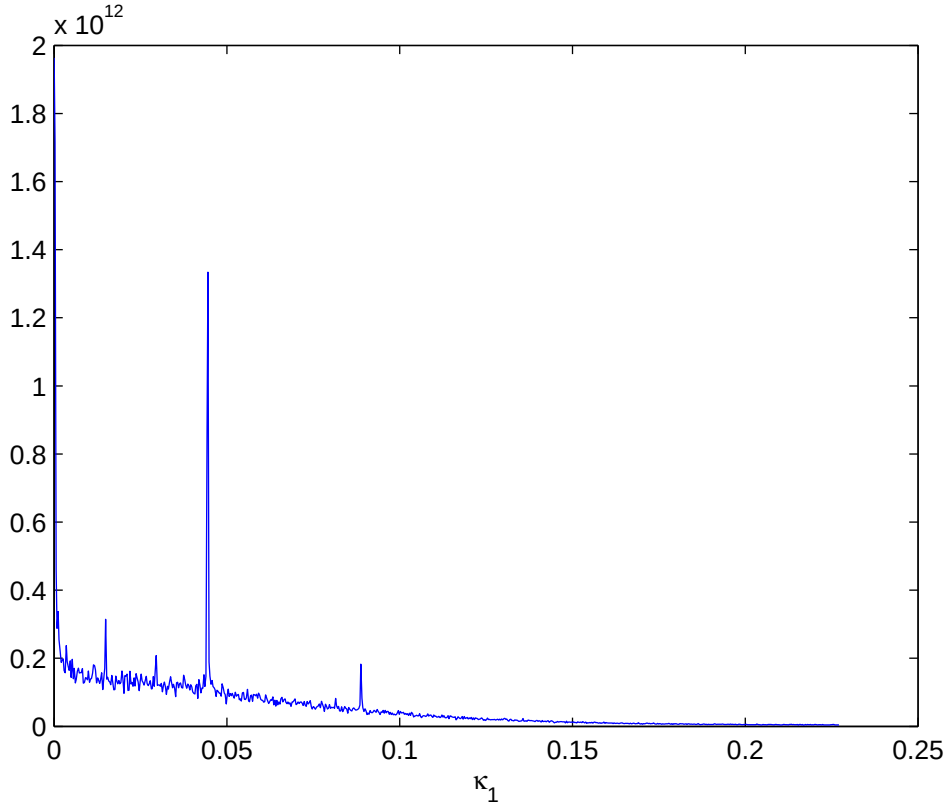

Figure 16.2: Fast Fourier Transform of one of the experimental TMV images. The highest peak appears at the 3rd layer line, and thus the apparent period is estimated to be 67.3401Å.

16.2 Resolution via FSC as a function of number of images

Figure 16.3 shows FSC curves of three types: direct-FSC where $F^{\mathrm{a}}(\mathbf{k})$ is the reconstruction resulting from using even numbered images, direct-FSC where $F^{\mathrm{a}}(\mathbf{k})$ is the reconstruction resulting from using odd numbered images, and even/odd-FSC, as a function of the number of images used in the reconstruction calculation. Each image yields subimages where each subimage measures 128×128 pixels. Three subimages per image are used due to computer memory constraints and the subimages used are taken from the center of the image. As the number of images increases, the three types of FSC give roughly the same resolution values given, i.e., at threshold of 0.5 for the case of 55 images. In Figure 16.4, a part of the data shown in Figure 16.3 is replotted in order to emphasize the gain in resolution achieved by using more images.

16.3 Ability to determine the correct values of u and v

In Table 16.2 is shown the rank-ordered list of log likelihood values as a function of the assumed value of u and v for a reconstruction problem with 64 images. The second highest log likelihood value corresponds to the correct u and v values, which are $u = 49$ and $v = 3$, while the highest log likelihood values correspond to $u = 43$ and $v = 3$. The data from Table 16.2 are plotted in Figure 16.5. These plots make clearer the absence of ambiguity in the estimate of v and the presence of ambiguity in the estimate of u, where the estimator is ambiguous about $u \in \{43, 49, 55\}$ which is every 6th integer corresponding to insertion or deletion of pair of motifs from each of the three turns of one period of the $v = 3$ helical symmetry.

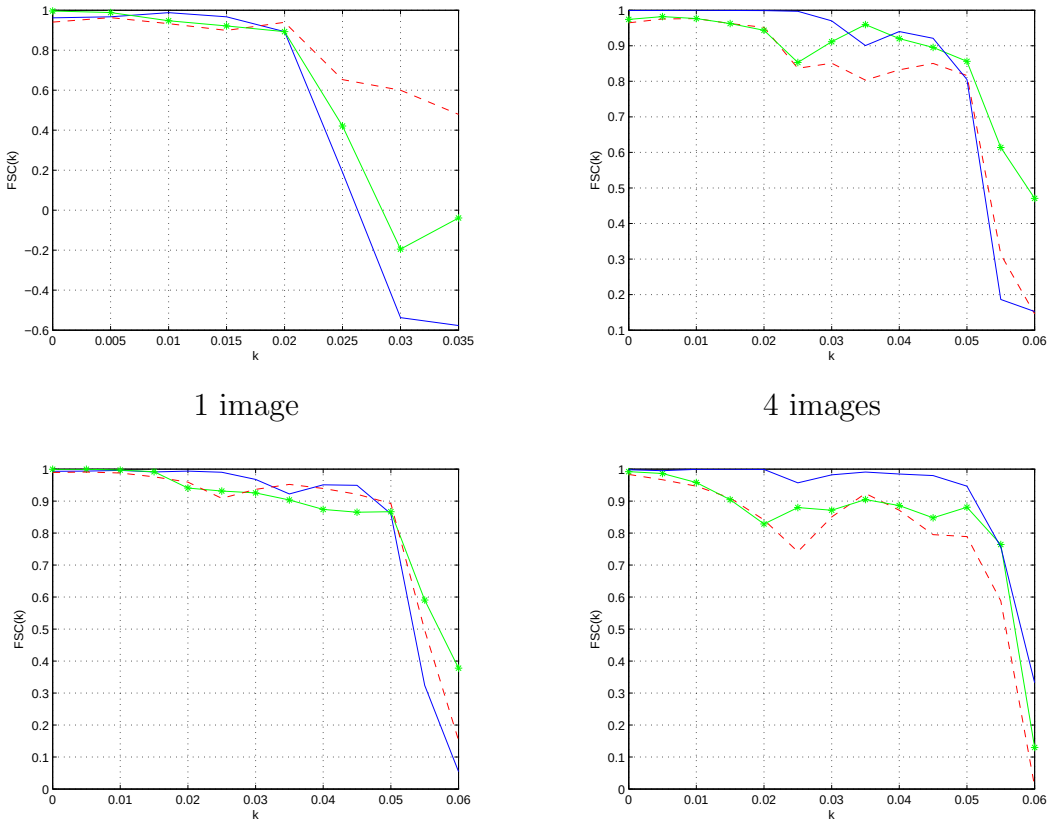

Figure 16.3: FSC curves as a function of number of experimental images used. Each panel shows three FSC curves: direct-FSC where the reconstruction results from using even numbered images, direct-FSC where the reconstruction results from using odd numbered images, and even/odd-FSC, which are indicated by dashed red, solid starred green, and solid blue, respectively.

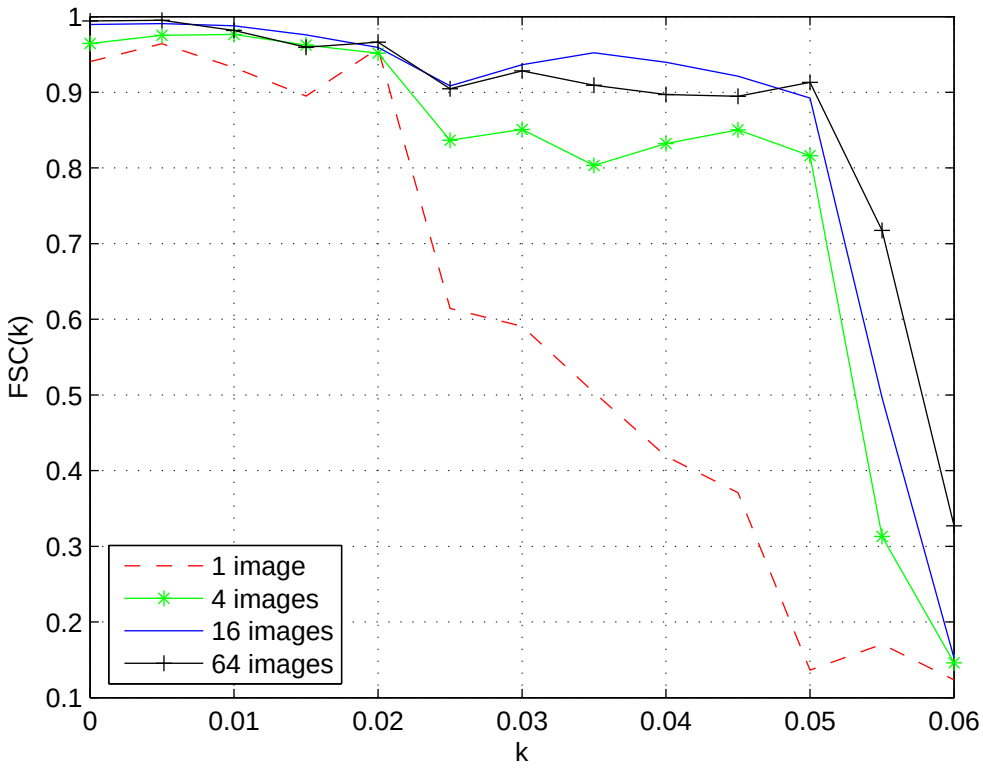

Figure 16.4: Direct-FSC curves as a function of number of experimental images used.

Table 16.2: Rank-ordered list of log likelihood values as a function of the assumed value of u and v for 64 images. The correct values are $u = 49$ and $v = 3$ which is the second highest log likelihood in the list.

u	v	log likelihood
43	3	-5046639
49	3	-5046673
55	3	-5046753
41	3	-5046845
47	3	-5046876
53	3	-5046936
61	3	-5046984
59	3	-5047025
58	3	-5047591
50	3	-5047599
56	3	-5047609
52	3	-5047614
46	3	-5047629
44	3	-5047677
59	4	-5054236
61	4	-5054445
67	4	-5054547
69	4	-5054587
75	4	-5054642
77	4	-5054645
55	4	-5054665
57	4	-5054752
68	5	-5054864
63	4	-5054903
65	4	-5054987
71	4	-5054998
73	4	-5055040
81	4	-5055117
79	4	-5055130

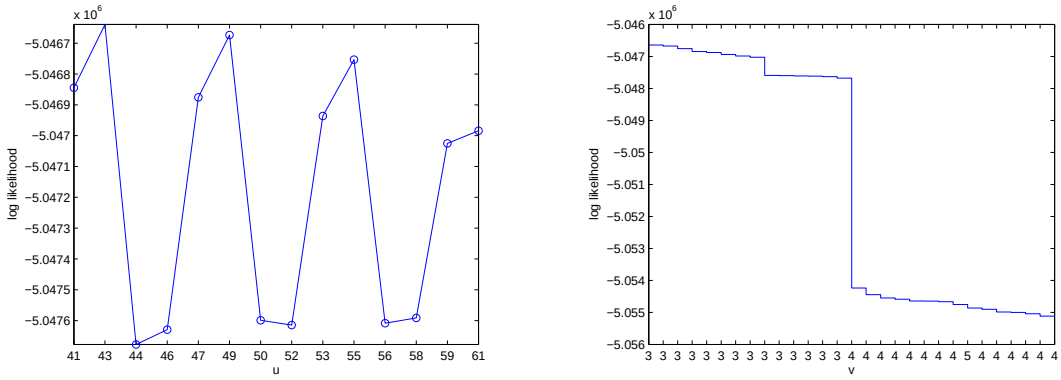

(a) (b)

Figure 16.5: Plots of the log likelihood values from Table 16.2. Panel (a): The log likelihood values as a function of u for the case $v = 3$. In order to get the correct u, a high resolution reconstruction is required, otherwise, as shown in the plot, the estimated u is likely to be a multiple of 2 motifs per turn different from the true answer. Panel (b): The log likelihood values as a function of v showing that $v = 3$ has a substantially higher likelihood than $v = 4$ or $v = 5$.

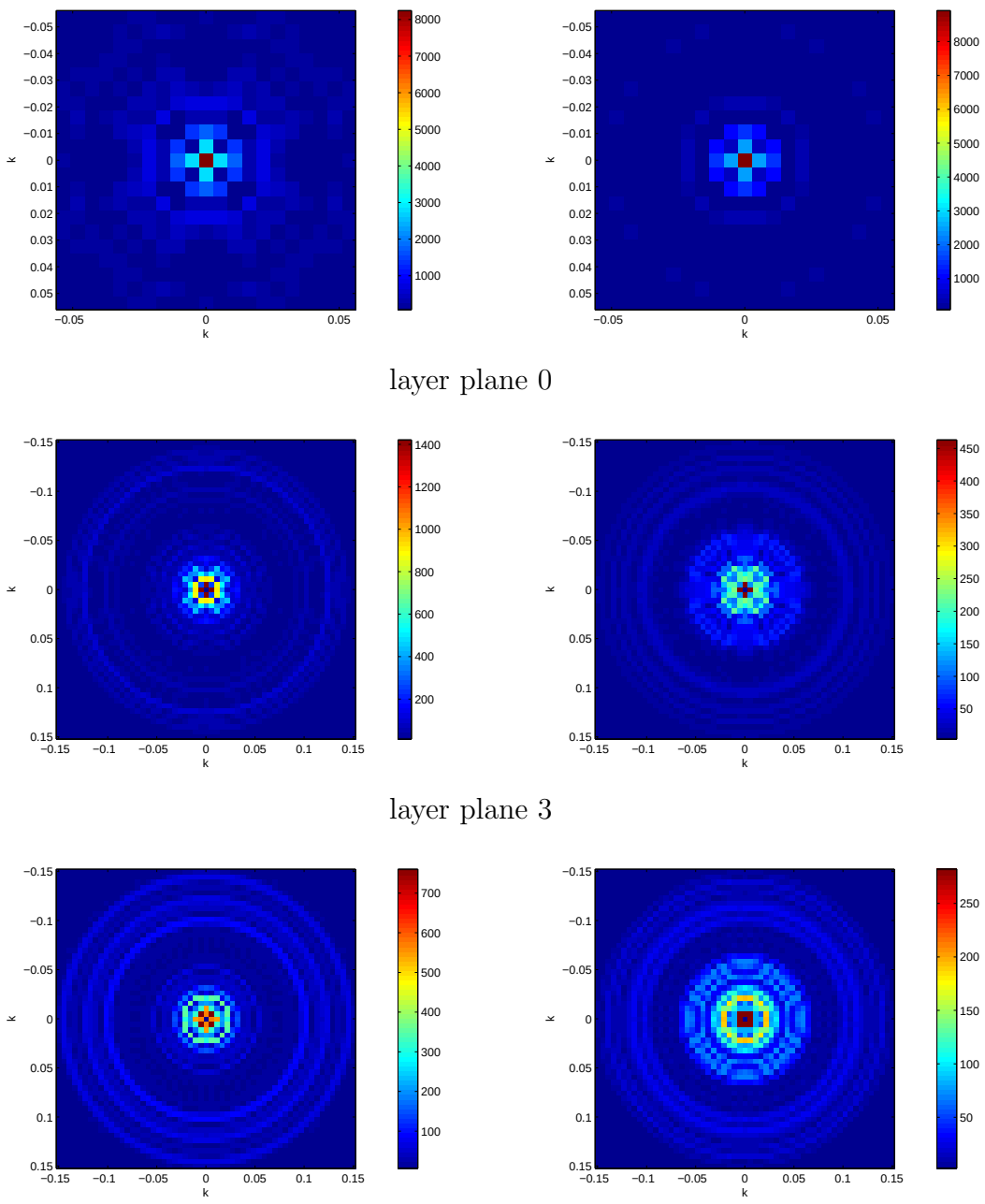

Figure 16.6: Layer planes shown as images: Column (a): The reconstruction from 64 experimental images. Column (b): The planes computed from the PDB which would be used in a matched-FSC calculation.

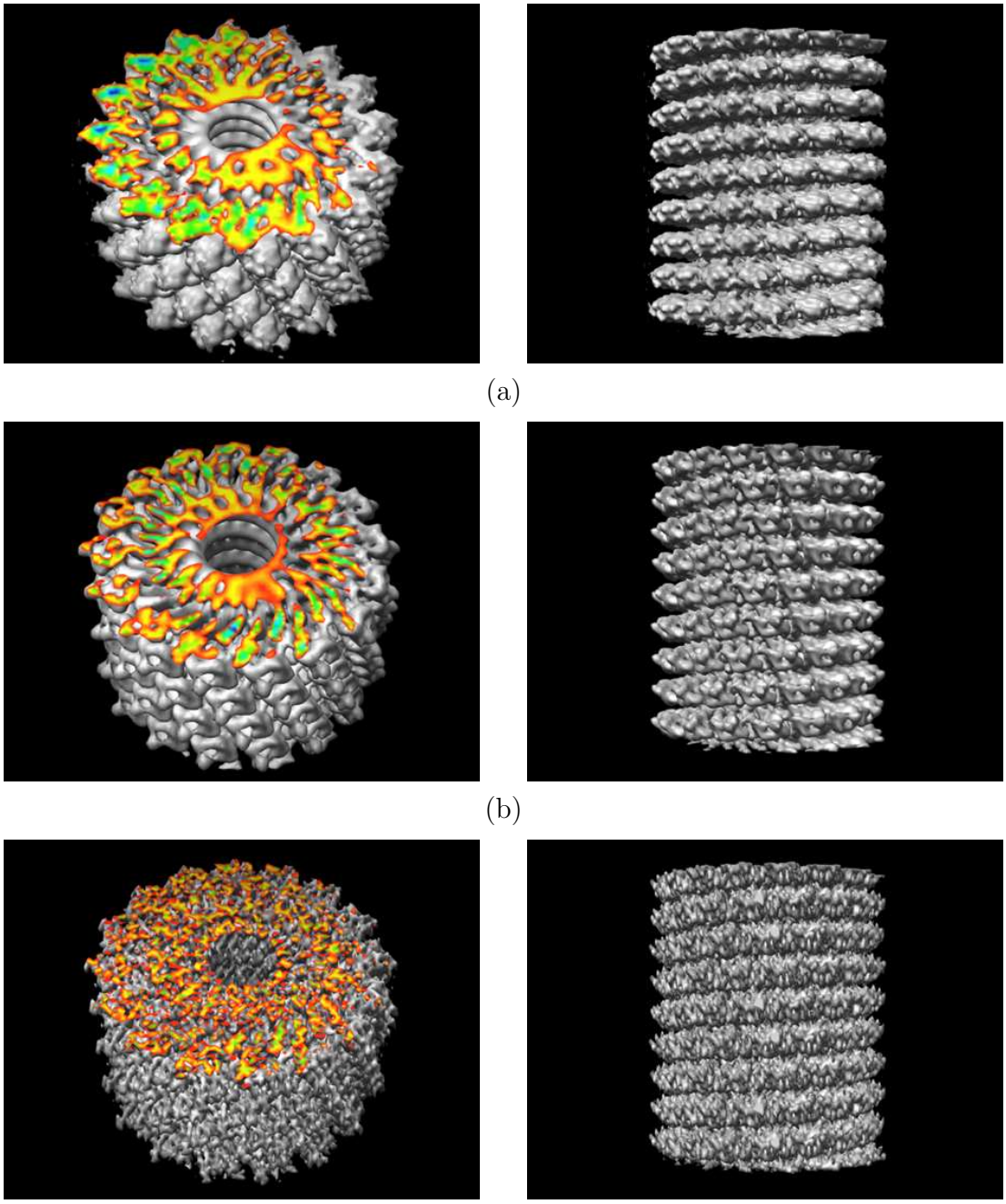

Figure 16.7: Surface renderings by UCSF Chimera [4]. Row (a): The reconstruction from 64 experimental images. Row (b): The cube that results from the planes computed from the PDB which would be used in a matched-FSC calculation. Row (c): The cube that results from the planes computed from the PDB which would be used in a direct-FSC calculation.

16.4 Comparison with PDB for 64 images

Figures 16.6 and 16.7 compare the reconstruction from 64 experimental images with the PDB structure. Figure 16.6 shows three of the layer planes while Figure 16.7 shows the real-space 3-D cubes.

CHAPTER 17

FUTURE WORK

The current software does not support different CTFs for different images. The current algorithm and software assume that c is a different and independent random variable for each subimage. The current algorithm and software process nonoverlapping subimages, while the usual approach is to use overlapping subimages. In some objects, it may be appropriate to use radial basis functions where $r_1 = 0$ and $\rho(\mathbf{x} = \mathbf{0}) \neq 0$ and these need to be implemented in both real and reciprocal space. Using different CTFs and overlapping subimages will require a parallel C implementation of the software.

APPENDIX A

CALCULATION OF THE NORMALIZER FOR THE RADIAL BASIS FUNCTIONS

The calculation begins with Eq. 6.50 which is repeated here:

$$M_{n,p}^2 = \int_a^b \left[c_1 J_n(\gamma_{n,p} r) + c_2 Y_n(\gamma_{n,p} r)\right]^2 r \mathrm{d}r \tag{A.1}$$

$$= \int_a^b \left[c_1^2 J_n^2(\gamma_{n,p} r) + 2c_1 c_2 J_n(\gamma_{n,p} r) Y_n(\gamma_{n,p} r) + c_2^2 Y_n^2(\gamma_{n,p} r)\right] r \mathrm{d}r. \tag{A.2}$$

Separate formulas for each of the three terms follow:

$$\int_a^b J_n^2(\gamma_{n,p} r) r \mathrm{d}r = \frac{r^2}{4}[2J_n^2(\gamma_{n,p} r) - 2J_{n+1}(\gamma_{n,p} r) J_{n-1}(\gamma_{n,p} r)]\Big|_a^b \tag{A.3}$$

$$\int_a^b Y_n^2(\gamma_{n,p} r) r \mathrm{d}r = \frac{r^2}{4}[2Y_n^2(\gamma_{n,p} r) - 2Y_{n+1}(\gamma_{n,p} r) Y_{n-1}(\gamma_{n,p} r)]\Big|_a^b \tag{A.4}$$

$$\int_a^b J_n(\gamma_{n,p} r) Y_n(\gamma_{n,p} r) r \mathrm{d}r$$
$$= \frac{r^2}{4}[2J_n(\gamma_{n,p} r) Y_n(\gamma_{n,p} r) - J_{n+1}(\gamma_{n,p} r) Y_{n-1}(\gamma_{n,p} r) - J_{n-1}(\gamma_{n,p} r) Y_{n+1}(\gamma_{n,p} r)]\Big|_a^b. \tag{A.5}$$

Substitute these results into Eq. A.2 to get

$$\begin{aligned} M_{n,p}^2 &= c_1^2 \frac{b^2}{4}[2J_n^2(\gamma_{n,p} b) - 2J_{n+1}(\gamma_{n,p} b) J_{n-1}(\gamma_{n,p} b)] \\ &\quad - c_1^2 \frac{a^2}{4}[2J_n^2(\gamma_{n,p} a) - 2J_{n+1}(\gamma_{n,p} a) J_{n-1}(\gamma_{n,p} a)] \\ &\quad + 2c_1 c_2 \frac{b^2}{4}[2J_n(\gamma_{n,p} b) Y_n(\gamma_{n,p} b) - J_{n+1}(\gamma_{n,p} b) Y_{n-1}(\gamma_{n,p} b) - J_{n-1}(\gamma_{n,p} b) Y_{n+1}(\gamma_{n,p} b)] \\ &\quad - 2c_1 c_2 \frac{a^2}{4}[2J_n(\gamma_{n,p} a) Y_n(\gamma_{n,p} a) - J_{n+1}(\gamma_{n,p} a) Y_{n-1}(\gamma_{n,p} a) - J_{n-1}(\gamma_{n,p} a) Y_{n+1}(\gamma_{n,p} a)] \\ &\quad + c_2^2 \frac{b^2}{4}[2Y_n^2(\gamma_{n,p} b) - 2Y_{n+1}(\gamma_{n,p} b) Y_{n-1}(\gamma_{n,p} b)] \\ &\quad - c_2^2 \frac{a^2}{4}[2Y_n^2(\gamma_{n,p} a) - 2Y_{n+1}(\gamma_{n,p} a) Y_{n-1}(\gamma_{n,p} a)]. \end{aligned} \tag{A.6}$$

Assume

$$J_n(\gamma_{n,p} a) \neq 0. \tag{A.7}$$

Substitute Eq. 6.35 to get

$$
\begin{aligned}
&\frac{4}{c_2^2}M_{n,p}^2 \\
&= \left[\frac{Y_n(\gamma_{n,p}a)}{J_n(\gamma_{n,p}a)}\right]^2 b^2[2J_n^2(\gamma_{n,p}b) - 2J_{n+1}(\gamma_{n,p}b)J_{n-1}(\gamma_{n,p}b)] \\
&\quad - \left[\frac{Y_n(\gamma_{n,p}a)}{J_n(\gamma_{n,p}a)}\right]^2 a^2[2J_n^2(\gamma_{n,p}a) - 2J_{n+1}(\gamma_{n,p}a)J_{n-1}(\gamma_{n,p}a)] \\
&\quad -2\left[\frac{Y_n(\gamma_{n,p}a)}{J_n(\gamma_{n,p}a)}\right] b^2 \times \\
&\quad \times[2J_n(\gamma_{n,p}b)Y_n(\gamma_{n,p}b) - J_{n+1}(\gamma_{n,p}b)Y_{n-1}(\gamma_{n,p}b) - J_{n-1}(\gamma_{n,p}b)Y_{n+1}(\gamma_{n,p}b)] \\
&\quad +2\left[\frac{Y_n(\gamma_{n,p}a)}{J_n(\gamma_{n,p}a)}\right] a^2 \times \\
&\quad \times[2J_n(\gamma_{n,p}a)Y_n(\gamma_{n,p}a) - J_{n+1}(\gamma_{n,p}a)Y_{n-1}(\gamma_{n,p}a) - J_{n-1}(\gamma_{n,p}a)Y_{n+1}(\gamma_{n,p}a)] \\
&\quad +b^2[2Y_n^2(\gamma_{n,p}b) - 2Y_{n+1}(\gamma_{n,p}b)Y_{n-1}(\gamma_{n,p}b)] \\
&\quad -a^2[2Y_n^2(\gamma_{n,p}a) - 2Y_{n+1}(\gamma_{n,p}a)Y_{n-1}(\gamma_{n,p}a)]. \qquad \text{(A.8)}
\end{aligned}
$$

Collect terms separately. Terms(1)+(5)+(11): $2b^2$ multiply the follows,

$$
\begin{aligned}
&\frac{Y_n^2(\gamma_{n,p}a)}{J_n^2(\gamma_{n,p}a)}J_n^2(\gamma_{n,p}b) - 2\frac{Y_n(\gamma_{n,p}a)}{J_n(\gamma_{n,p}a)}J_n(\gamma_{n,p}b)Y_n(\gamma_{n,p}b) + Y_n^2(\gamma_{n,p}b) \\
&= \frac{Y_n^2(\gamma_{n,p}a)}{J_n^2(\gamma_{n,p}a)}J_n^2(\gamma_{n,p}b) - \frac{Y_n(\gamma_{n,p}a)}{J_n^2(\gamma_{n,p}a)}J_n(\gamma_{n,p}a)J_n(\gamma_{n,p}b)Y_n(\gamma_{n,p}b) \\
&\quad -\frac{Y_n(\gamma_{n,p}a)}{J_n(\gamma_{n,p}a)}J_n(\gamma_{n,p}b)Y_n(\gamma_{n,p}b) + \frac{J_n(\gamma_{n,p}a)}{J_n(\gamma_{n,p}a)}Y_n^2(\gamma_{n,p}b) \qquad \text{(A.9)} \\
&= \frac{Y_n(\gamma_{n,p}a)J_n(\gamma_{n,p}b)}{J_n^2(\gamma_{n,p}a)}[Y_n(\gamma_{n,p}a)J_n(\gamma_{n,p}b) - J_n(\gamma_{n,p}a)Y_n(\gamma_{n,p}b)] \\
&\quad +\frac{Y_n(\gamma_{n,p}b)}{J_n(\gamma_{n,p}a)}[-Y_n(\gamma_{n,p}a)J_n(\gamma_{n,p}b) + J_n(\gamma_{n,p}a)Y_n(\gamma_{n,p}b)] \qquad \text{(A.10)} \\
&= \frac{Y_n(\gamma_{n,p}a)J_n(\gamma_{n,p}b)}{J_n^2(\gamma_{n,p}a)}0 + \frac{Y_n(\gamma_{n,p}b)}{J_n(\gamma_{n,p}a)}0 \qquad \text{(A.11)} \\
&= 0. \qquad \text{(A.12)}
\end{aligned}
$$

Similarly, terms(3)+(8)+(13): $2a^2$ multiply the follows,

$$
-\frac{Y_n^2(\gamma_{n,p}a)}{J_n^2(\gamma_{n,p}a)}J_n^2(\gamma_{n,p}a) + 2\frac{Y_n(\gamma_{n,p}a)}{J_n(\gamma_{n,p}a)}J_n(\gamma_{n,p}a)Y_n(\gamma_{n,p}a) - Y_n^2(\gamma_{n,p}a) = 0. \quad \text{(A.13)}
$$

Substitute these results into Eq. A.8 to get,

$$\begin{aligned}
&\frac{4}{c_2^2}M_{n,p}^2 \\
&= \left[\frac{Y_n(\gamma_{n,p}a)}{J_n(\gamma_{n,p}a)}\right]^2 b^2[-2J_{n+1}(\gamma_{n,p}b)J_{n-1}(\gamma_{n,p}b)] \\
&\quad - \left[\frac{Y_n(\gamma_{n,p}a)}{J_n(\gamma_{n,p}a)}\right]^2 a^2[-2J_{n+1}(\gamma_{n,p}a)J_{n-1}(\gamma_{n,p}a)] \\
&\quad -2\left[\frac{Y_n(\gamma_{n,p}a)}{J_n(\gamma_{n,p}a)}\right] b^2[-J_{n+1}(\gamma_{n,p}b)Y_{n-1}(\gamma_{n,p}b) - J_{n-1}(\gamma_{n,p}b)Y_{n+1}(\gamma_{n,p}b)] \\
&\quad +2\left[\frac{Y_n(\gamma_{n,p}a)}{J_n(\gamma_{n,p}a)}\right] a^2[-J_{n+1}(\gamma_{n,p}a)Y_{n-1}(\gamma_{n,p}a) - J_{n-1}(\gamma_{n,p}a)Y_{n+1}(\gamma_{n,p}a)] \\
&\quad +b^2[-2Y_{n+1}(\gamma_{n,p}b)Y_{n-1}(\gamma_{n,p}b)] - a^2[-2Y_{n+1}(\gamma_{n,p}a)Y_{n-1}(\gamma_{n,p}a)]. \qquad \text{(A.14)}
\end{aligned}$$

By Eq. 6.48 it follows that

$$\begin{aligned}
-J_{v-1}(z)J_{v+1}(z) &= \left[J_v'(z) + \frac{v}{z}J_v(z)\right]\left[J_v'(z) - \frac{v}{z}J_v(z)\right] &\text{(A.15)}\\
&= [J_v'(z)]^2 - (\frac{v}{z})^2[J_v(z)]^2 &\text{(A.16)}\\
-Y_{v-1}(z)Y_{v+1}(z) &= [Y_v'(z)]^2 - (\frac{v}{z})^2[Y_v(z)]^2 &\text{(A.17)}
\end{aligned}$$

$$\begin{aligned}
&-J_{v+1}(z)Y_{v-1}(z) - J_{v-1}(z)Y_{v+1}(z) \\
&= \left[J_v'(z) - \frac{v}{z}J_v(z)\right]\left[Y_v'(z) + \frac{v}{z}Y_v(z)\right] \\
&\quad + \left[J_v'(z) + \frac{v}{z}J_v(z)\right]\left[Y_v'(z) - \frac{v}{z}Y_v(z)\right] &\text{(A.18)}\\
&= 2J_v'(z)Y_v'(z) - 2(\frac{v}{z})^2 J_v(z)Y_v(z). &\text{(A.19)}
\end{aligned}$$

Substitute these results into Eq. A.14 to get

$$\begin{aligned}
&\frac{4}{c_2^2}M_{n,p}^2 \\
&= \left[\frac{Y_n(\gamma_{n,p}a)}{J_n(\gamma_{n,p}a)}\right]^2 2b^2\left[[J_n'(\gamma_{n,p}b)]^2 - (\frac{n}{\gamma_{n,p}b})^2[J_n(\gamma_{n,p}b)]^2\right] \\
&\quad - \left[\frac{Y_n(\gamma_{n,p}a)}{J_n(\gamma_{n,p}a)}\right]^2 2a^2\left[[J_n'(\gamma_{n,p}a)]^2 - (\frac{n}{\gamma_{n,p}a})^2[J_n(\gamma_{n,p}a)]^2\right] \\
&\quad - 2\left[\frac{Y_n(\gamma_{n,p}a)}{J_n(\gamma_{n,p}a)}\right] 2b^2\left[J_n'(\gamma_{n,p}b)Y_n'(\gamma_{n,p}b) - (\frac{n}{\gamma_{n,p}b})^2 J_n(\gamma_{n,p}b)Y_n(\gamma_{n,p}b)\right]
\end{aligned}$$

$$
\begin{aligned}
&+2\left[\frac{Y_n(\gamma_{n,p}a)}{J_n(\gamma_{n,p}a)}\right]2a^2\left[J_n'(\gamma_{n,p}a)Y_n'(\gamma_{n,p}a)-(\frac{n}{\gamma_{n,p}a})^2J_n(\gamma_{n,p}a)Y_n(\gamma_{n,p}a)\right]\\
&+2b^2\left[[Y_n'(\gamma_{n,p}b)]^2-(\frac{n}{\gamma_{n,p}b})^2[Y_n(\gamma_{n,p}b)]^2\right]\\
&-2a^2\left[[Y_n'(\gamma_{n,p}a)]^2-(\frac{n}{\gamma_{n,p}a})^2[Y_n(\gamma_{n,p}a)]^2\right]. \qquad \text{(A.20)}
\end{aligned}
$$

Collect all the terms that are multiplied by $2b^2$,

$$
\begin{aligned}
&+\left[\frac{Y_n(\gamma_{n,p}a)}{J_n(\gamma_{n,p}a)}\right]^2\left[[J_n'(\gamma_{n,p}b)]^2-(\frac{n}{\gamma_{n,p}b})^2[J_n(\gamma_{n,p}b)]^2\right]\\
&-2\left[\frac{Y_n(\gamma_{n,p}a)}{J_n(\gamma_{n,p}a)}\right]\left[J_n'(\gamma_{n,p}b)Y_n'(\gamma_{n,p}b)-(\frac{n}{\gamma_{n,p}b})^2J_n(\gamma_{n,p}b)Y_n(\gamma_{n,p}b)\right]\\
&+[Y_n'(\gamma_{n,p}b)]^2-(\frac{n}{\gamma_{n,p}b})^2[Y_n(\gamma_{n,p}b)]^2 \qquad \text{(A.21)}
\end{aligned}
$$

Simplify terms(2)+(4)+(6) in Eq. A.21 to get

$$
\begin{aligned}
&(\frac{n}{\gamma_{n,p}b})^2\left[-Y_n^2(\gamma_{n,p}a)\frac{J_n^2(\gamma_{n,p}b)}{J_n^2(\gamma_{n,p}a)}+2Y_n(\gamma_{n,p}a)Y_n(\gamma_{n,p}b)\frac{J_n(\gamma_{n,p}b)}{J_n(\gamma_{n,p}a)}-Y_n^2(\gamma_{n,p}b)\right]\\
&= (\frac{n}{\gamma_{n,p}b})^2\left[\frac{Y_n(\gamma_{n,p}a)J_n(\gamma_{n,p}b)}{J_n^2(\gamma_{n,p}a)}[-Y_n(\gamma_{n,p}a)J_n(\gamma_{n,p}b)+J_n(\gamma_{n,p}a)Y_n(\gamma_{n,p}b)]\right.\\
&\quad\left.+\frac{Y_n(\gamma_{n,p}b)}{J_n(\gamma_{n,p}a)}[Y_n(\gamma_{n,p}a)J_n(\gamma_{n,p}b)-Y_n(\gamma_{n,p}b)J_n(\gamma_{n,p}a)]\right]\\
&= 0 \qquad \text{(A.22)}
\end{aligned}
$$

Substitute Eq. A.22 into Eq. A.21 to get

$$
\begin{aligned}
&\left[\frac{Y_n(\gamma_{n,p}a)}{J_n(\gamma_{n,p}a)}\right]^2[J_n'(\gamma_{n,p}b)]^2-\left[\frac{Y_n(\gamma_{n,p}a)}{J_n(\gamma_{n,p}a)}\right]2J_n'(\gamma_{n,p}b)Y_n'(\gamma_{n,p}b)+[Y_n'(\gamma_{n,p}b)]^2\\
&\quad= \frac{1}{J_n^2(\gamma_{n,p}a)}[J_n(\gamma_{n,p}a)Y_n'(\gamma_{n,p}b)-J_n'(\gamma_{n,p}b)Y_n(\gamma_{n,p}a)]^2 \qquad \text{(A.23)}
\end{aligned}
$$

Therefore, the total contribution of the b^2 terms is

$$
\frac{2b^2}{J_n^2(\gamma_{n,p}a)}[J_n(\gamma_{n,p}a)Y_n'(\gamma_{n,p}b)-J_n'(\gamma_{n,p}b)Y_n(\gamma_{n,p}a)]^2. \qquad \text{(A.24)}
$$

Similarly, the total contribution of the a^2 terms is

$$
-\frac{2a^2}{J_n^2(\gamma_{n,p}a)}[J_n(\gamma_{n,p}a)Y_n'(\gamma_{n,p}a)-J_n'(\gamma_{n,p}a)Y_n(\gamma_{n,p}a)]^2. \qquad \text{(A.25)}
$$

Substitute these results into Eq. A.20 to get

$$\begin{aligned}\frac{4}{c_2^2}M_{n,p}^2 &= \frac{2b^2}{J_n^2(\gamma_{n,p}a)}[J_n(\gamma_{n,p}a)Y_n'(\gamma_{n,p}b) - J_n'(\gamma_{n,p}b)Y_n(\gamma_{n,p}a)]^2 \\ &\quad -\frac{2a^2}{J_n^2(\gamma_{n,p}a)}[J_n(\gamma_{n,p}a)Y_n'(\gamma_{n,p}a) - J_n'(\gamma_{n,p}a)Y_n(\gamma_{n,p}a)]^2. \quad \text{(A.26)}\end{aligned}$$

Finally, substitute Eq. 6.36 to get

$$\begin{aligned}M_{n,p} &= \left[\frac{1}{2}\{b^2[J_n(\gamma_{n,p}a)Y_n'(\gamma_{n,p}b) - J_n'(\gamma_{n,p}b)Y_n(\gamma_{n,p}a)]^2\right. \\ &\quad \left.-a^2[J_n(\gamma_{n,p}a)Y_n'(\gamma_{n,p}a) - J_n'(\gamma_{n,p}a)Y_n(\gamma_{n,p}a)]^2\}\right]^{\frac{1}{2}}. \quad \text{(A.27)}\end{aligned}$$

APPENDIX B

CYLINDRICAL HANKEL TRANSFORM OF THE RADIAL BASIS FUNCTIONS

The function $H_{n,p}(R)$ is the nth order cylindrical Hankel transform (Eqs. 3.3 and 3.4) of the function $h_{n,p}(r)$. The Hankel transform can be computed symbolically as is demonstrated in this appendix. With the normalizer, Eq. 6.28 becomes

$$h_{n,p}(r) = \frac{1}{M_{n,p}}[c_1 J_n(\gamma_{n,p} r) + c_2 Y_n(\gamma_{n,p} r)]. \tag{B.1}$$

The Hankel transform is

$$\begin{aligned} H_{n,p}(R) &= 2\pi \int_a^b h_{n,p}(r) J_n(2\pi R r) r \mathrm{d}r \\ &= \frac{2\pi}{M_{n,p}} \left[\int_a^b c_1 J_n(\gamma_{n,p} r) J_n(2\pi R r) r \mathrm{d}r + \int_a^b c_2 Y_n(\gamma_{n,p} r) J_n(2\pi R r) r \mathrm{d}r \right]. \end{aligned} \tag{B.2}$$

Apply Eq. 6.39 to get

$$\begin{aligned} &\int_a^b J_n(\gamma_{n,p} r) J_n(2\pi R r) r \mathrm{d}r \\ &= \frac{r}{(2\pi R)^2 - \gamma_{n,p}^2} [2\pi R J_{n+1}(2\pi R r) J_n(\gamma_{n,p} r) - \gamma_{n,p} J_n(2\pi R r) J_{n+1}(\gamma_{n,p} r)] \Big|_a^b \end{aligned} \tag{B.3}$$

$$\begin{aligned} &= \frac{b}{(2\pi R)^2 - \gamma_{n,p}^2} [2\pi R J_{n+1}(2\pi R b) J_n(\gamma_{n,p} b) - \gamma_{n,p} J_n(2\pi R b) J_{n+1}(\gamma_{n,p} b)] \\ &\quad - \frac{a}{(2\pi R)^2 - \gamma_{n,p}^2} [2\pi R J_{n+1}(2\pi R a) J_n(\gamma_{n,p} a) - \gamma_{n,p} J_n(2\pi R a) J_{n+1}(\gamma_{n,p} a)]. \end{aligned} \tag{B.4}$$

Similarly,

$$\int_a^b Y_n(\gamma_{n,p} r) J_n(2\pi R r) r \mathrm{d}r$$

$$= \frac{r}{(2\pi R)^2-\gamma_{n,p}^2}[2\pi R J_{n+1}(2\pi Rr)Y_n(\gamma_{n,p}r)-\gamma_{n,p}J_n(2\pi Rr)Y_{n+1}(\gamma_{n,p}r)]\Big|_a^b \tag{B.5}$$

$$\begin{aligned} = & \frac{b}{(2\pi R)^2-\gamma_{n,p}^2}[2\pi R J_{n+1}(2\pi Rb)Y_n(\gamma_{n,p}b)-\gamma_{n,p}J_n(2\pi Rb)Y_{n+1}(\gamma_{n,p}b)] \\ & -\frac{a}{(2\pi R)^2-\gamma_{n,p}^2}[2\pi R J_{n+1}(2\pi Ra)Y_n(\gamma_{n,p}a)-\gamma_{n,p}J_n(2\pi Ra)Y_{n+1}(\gamma_{n,p}a)]. \end{aligned} \tag{B.6}$$

Substitute these results into Eq. B.2 to get

$$\begin{aligned} H_{n,p}(R) = & \frac{-2\pi b}{M_{n,p}((2\pi R)^2-\gamma_{n,p}^2)}[2\pi R J_{n+1}(2\pi Rb)J_n(\gamma_{n,p}b)Y_n(\gamma_{n,p}a) \\ & -\gamma_{n,p}J_n(2\pi Rb)J_{n+1}(\gamma_{n,p}b)Y_n(\gamma_{n,p}a)] \\ & +\frac{2\pi a}{M_{n,p}((2\pi R)^2-\gamma_{n,p}^2)}[2\pi R J_{n+1}(2\pi Ra)J_n(\gamma_{n,p}a)Y_n(\gamma_{n,p}a) \\ & -\gamma_{n,p}J_n(2\pi Ra)J_{n+1}(\gamma_{n,p}a)Y_n(\gamma_{n,p}a)] \\ & +\frac{2\pi b}{M_{n,p}((2\pi R)^2-\gamma_{n,p}^2)}[2\pi R J_{n+1}(2\pi Rb)Y_n(\gamma_{n,p}b)J_n(\gamma_{n,p}a) \\ & -\gamma_{n,p}J_n(2\pi Rb)Y_{n+1}(\gamma_{n,p}b)J_n(\gamma_{n,p}a)] \\ & -\frac{2\pi a}{M_{n,p}((2\pi R)^2-\gamma_{n,p}^2)}[2\pi R J_{n+1}(2\pi Ra)Y_n(\gamma_{n,p}a)J_n(\gamma_{n,p}a) \\ & -\gamma_{n,p}J_n(2\pi Ra)Y_{n+1}(\gamma_{n,p}a)J_n(\gamma_{n,p}a)]. \end{aligned} \tag{B.7}$$

By Eqs. 6.30 and 6.31, in Eq. B.7, terms(1)+(5) = 0 and terms(3)+(7) = 0. Terms(2)+(6) have value:

$$\frac{b}{M_{n,p}((2\pi R)^2-\gamma_{n,p}^2)}\gamma_{n,p}J_n(2\pi Rb)[J_{n+1}(\gamma_{n,p}b)Y_n(\gamma_{n,p}a)-Y_{n+1}(\gamma_{n,p}b)J_n(\gamma_{n,p}a)]$$

while terms(4)+(8) have value:

$$\frac{a}{M_{n,p}((2\pi R)^2-\gamma_{n,p}^2)}\gamma_{n,p}J_n(2\pi Ra)[J_{n+1}(\gamma_{n,p}a)Y_n(\gamma_{n,p}a)-Y_{n+1}(\gamma_{n,p}a)J_n(\gamma_{n,p}a)].$$

Simplify these results further by computing the follows,

$$J_{n+1}(\gamma_{n,p}b)Y_n(\gamma_{n,p}a)-Y_{n+1}(\gamma_{n,p}b)J_n(\gamma_{n,p}a)$$

$$
\begin{aligned}
&= \left[\frac{n}{\gamma_{n,p}b}J_n(\gamma_{n,p}b) - J'_n(\gamma_{n,p}b)\right] Y_n(\gamma_{n,p}a) \\
&\quad - \left[\frac{n}{\gamma_{n,p}b}Y_n(\gamma_{n,p}b) - Y'_n(\gamma_{n,p}b)\right] J_n(\gamma_{n,p}a) \qquad \text{(B.8)} \\
&= \frac{n}{\gamma_{n,p}b}[J_n(\gamma_{n,p}b)Y_n(\gamma_{n,p}a) - Y_n(\gamma_{n,p}b)J_n(\gamma_{n,p}a)] \\
&\quad + [Y'_n(\gamma_{n,p}b)J_n(\gamma_{n,p}a) - J'_n(\gamma_{n,p}b)Y_n(\gamma_{n,p}a)] \qquad \text{(B.9)} \\
&= Y'_n(\gamma_{n,p}b)J_n(\gamma_{n,p}a) - J'_n(\gamma_{n,p}b)Y_n(\gamma_{n,p}a). \qquad \text{(B.10)}
\end{aligned}
$$

Similarly,

$$
\begin{aligned}
&J_{n+1}(\gamma_{n,p}a)Y_n(\gamma_{n,p}a) - Y_{n+1}(\gamma_{n,p}a)J_n(\gamma_{n,p}a) \\
&\quad = Y'_n(\gamma_{n,p}a)J_n(\gamma_{n,p}a) - J'_n(\gamma_{n,p}a)Y_n(\gamma_{n,p}a). \qquad \text{(B.11)}
\end{aligned}
$$

Compute the derivative of $h_{n,p}(r)$, with the result that

$$
\begin{aligned}
&h'_{n,p}(r) \\
&= \frac{d}{dr}\left[\frac{-Y_n(\gamma_{n,p}a)J_n(\gamma_{n,p}r) + J_n(\gamma_{n,p}a)Y_n(\gamma_{n,p}r)}{M_{n,p}}\right] \qquad \text{(B.12)} \\
&= \frac{\gamma_{n,p}}{M_{n,p}}\left[Y'_n(\gamma_{n,p}r)J_n(\gamma_{n,p}a) - J'_n(\gamma_{n,p}r)Y_n(\gamma_{n,p}a)\right]. \qquad \text{(B.13)}
\end{aligned}
$$

Finally, substitute these results into Eq. B.7 to get

$$
\begin{aligned}
H_{n,p}(R) &= \frac{2\pi b}{M_{n,p}((2\pi R)^2 - \gamma_{n,p}^2)}\gamma_{n,p}J_n(2\pi Rb)h'_{n,p}(b)\frac{M_{n,p}}{\gamma_{n,p}} \\
&\quad - \frac{2\pi a}{M_{n,p}((2\pi R)^2 - \gamma_{n,p}^2)}\gamma_{n,p}J_n(2\pi Ra)h'_{n,p}(a)\frac{M_{n,p}}{\gamma_{n,p}} \qquad \text{(B.14)} \\
&= 2\pi\frac{bh'_{n,p}(b)J_n(2\pi Rb) - ah'_{n,p}(a)J_n(2\pi Ra)}{(2\pi R)^2 - \gamma_{n,p}^2} \qquad \text{(B.15)}
\end{aligned}
$$

where $h'_{n,p}(\cdot)$ is the derivative of $h_{n,p}(\cdot)$. If $2\pi R = \gamma_{n,p}$, the numerator and denominator are both zero. By L'Hospital's Rule,

$$
\begin{aligned}
H_{n,p}(R) &= 2\pi\frac{2\pi b^2 h'_{n,p}(b)J'_n(2\pi Rb) - 2\pi a^2 h'_{n,p}(a)J'_n(2\pi Ra)}{2(2\pi R)(2\pi)} \qquad \text{(B.16)} \\
&= \pi\frac{b^2 h'_{n,p}(b)J'_n(\gamma_{n,p}b) - a^2 h'_{n,p}(a)J'_n(\gamma_{n,p}a)}{\gamma_{n,p}}. \qquad \text{(B.17)}
\end{aligned}
$$

BIBLIOGRAPHY

[1] Seunghee Lee. *Model-based statistical inverse problems for objects with helical symmetry and applications to viral structural biology.* PhD thesis, School of Electrical and Computer Engineering, Purdue University, West Lafayette, Indiana, USA, May 2009.

[2] D. J. DeRosier and P. B. Moore. Reconstruction of three-dimensional images from electron micrographs of structures with helical symmetry. *J. Mol. Bio.*, 52:355–369, 1970.

[3] R. A. Crowther, D. J. DeRosier, A. Klug, and F. R. S. The reconstruction of a three-dimensional structure from projections and its application to electron microscopy. *Proc. Roy. Soc. Lond.*, A317:319–340, 1970.

[4] E. F. Pettersen, T. D. Goddard, C. C. Huang, G. S. Couch, D. M. Greenblatt, E. C. Meng, and T. E. Ferrin. UCSF Chimera—A visualization system for exploratory research and analysis. *J. Comput. Chem.*, 25(13):1605–1612, 2004.

[5] A. Klug, F. H. C. Crick, and H. W. Wyckoff. Diffraction by helical structures. *Acta Cryst.*, 11:199–213, 1958.

[6] D. J. DeRosier and A. Klug. Reconstruction of three dimensional structures from electron micrographs. *Nature*, 217:130–134, January 1968.

[7] W. Cochran, F. H. C. Crick, and V. Vand. The structure of synthetic polypeptides. I. the transform of atoms on a helix. *Acta Cryst.*, 5:581–586, 1952.

[8] A. N. Barrett, J. B. Leigh, K. C. Holmes, R. Leberman, E. Mandelkow, P. von. Sengbusch, and A. Klug. An electron-density map of tobacco mosaic virus at 10 Å resolution. *Cold Spring Harbor Symposium on Quantitative Biology*, 36:433–448, 1972.

[9] K. C. Holmes, G. J. Stubbs, E. Mandelkow, and U. Gallwitz. Structure of tobacco mosaic virus at 6.7 Å resolution. *Nature*, 254:192–196, March 1975.

[10] K. Namba and G. Stubbs. Solving the phase problem in fiber diffraction. application to tobacco mosaic virus at 3.6 Å resolution. *Acta Cryst.*, A41:252–262, 1985.

[11] K. Namba, R. Pattanayek, and G. Stubbs. Visualization for protein-nucleic

acid interactions in a virus: Refined structure of intact tobacco mosaic virus at 2.9 Å resolution by x-ray fiber diffraction. *J. Mol. Bio.*, 208:307–325, 1989.

[12] Rosalind E. Franklin and K. C. Holmes. Tobacco mosaic virus: application of the method of isomorphous replacement to the determination of the helical parameters and radial density distribution. *Acta Cryst.*, 11:213–220, 1958.

[13] Rosalind E. Franklin and A. Klug. The splitting of layer lines in x-ray fibre diagrams of helical structures: application to tobacco mosaic virus. *Acta Cryst.*, 8:777–780, 1955.

[14] P. F. C. Gilbert. The reconstruction of a three-dimensional structure from projections and its application to electron microscopy. II. direct methods. *Proc. Roy. Soc. Lond.*, B182:89–102, 1972.

[15] D. J. DeRosier. Three-dimensional image reconstruction of helical structures. *Phil. Trans. Roy. Soc. Lond.*, B261:209–210, 1971.

[16] D. G. Morgan and D. J. DeRosier. Processing images of helical structures: a new twist. *Ultramicroscopy*, 46:263–285, 1992.

[17] T. Jeng, R.A. Crowther, G. Stubbs, and W. Chiu. Visualization of alpha-helices in tobacco mosaic virus by cryo-electron microscopy. *J. Mol. Bio.*, 205:251–257, 1989.

[18] R. A. Crowther, Raul Padron, and Roger Craig. Arrangement of the heads of myosin in relaxed thick filaments from tarantula muscle. *J. Mol. Bio.*, 184:429–439, 1985.

[19] H. Wang and E. Nogales. An iterative Fourier-Bessel algorithm for reconstruction of helical structures with severe Bessel overlap. *Nature*, 435:911–915, 2004.

[20] E. H. Egelman. The iterative helical real space reconstruction method: surmounting the problems posed by real polymers. *J. Struct. Biol.*, 157:83–94, 2007.

[21] C. Sachse, J. Z. Chen, P. Coureux, M. E. Stroupe, M. Fandrich, and N. Grigorieff. High-resolution electron microscopy of helical specimens: a fresh look at tobacco mosaic virus. *J. Mol. Bio.*, 371:812–835, 2007.

[22] M. F. Moody. Image analysis of electron micrographs. In P. W. Hawkes

and U. Valdrè, editors, *Biophysical Electron Microscopy: Basic Concepts and Modern Techniques*, chapter 7, pages 145–287. Academic Press, 1990.

[23] Morris E. Rose. *Elementary Theory of Angular Momentum*. John Wiley and Sons, New York, 1957.

[24] Yibin Zheng and Peter C. Doerschuk. Iterative reconstruction of three-dimensional objects from averaged Fourier-transform magnitude: solution and fiber x-ray scattering problems. *J. Opt. Soc. Am. A*, 13(7):1483–1494, July 1996.

[25] Philip M. Morse and Herman Feshbach. *Methods of Theoretical Physics*. McGraw-Hill, New York, 1953.

[26] M. Stark, Harold. *An Introduction to Number Theory*. Markham Publishing Company, 1970.

[27] T. S. Baker, N. H. Olson, and S. D. Fuller. Adding the third dimension to virus life cycles: Three-dimensional reconstruction of icosahedral viruses from cryo-electron micrographs. *Microbiology and Molecular Biology Reviews*, 63(4):862–922, December 1999.

[28] Peter C. Doerschuk and John E. Johnson. *Ab initio* reconstruction and experimental design for cryo electron microscopy. *IEEE Trans. Info. Theory*, 46(5):1714–1729, August 2000.

[29] Zhye Yin, Yili Zheng, Peter C. Doerschuk, Padmaja Natarajan, and John E. Johnson. A statistical approach to computer processing of cryo electron microscope images: Virion classification and 3-D reconstruction. *J. Struct. Biol.*, 144(1/2):24–50, 2003.

[30] Earl A. Coddington and Norman Levinson. *Theory of Ordinary Differential Equations*. McGraw-Hill, New York, 1955.

[31] A. Erdelyi, editor. *Higher Transcendental Functions*. McGraw-Hill, 1953.

[32] Junghoon Lee, Peter C. Doerschuk, and John E. Johnson. Exact reduced-complexity maximum likelihood reconstruction of multiple 3-D objects from unlabeled unoriented 2-D projections and electron microscopy of viruses. *IEEE Trans. Image Proc.*, 16(11):2865–2878, November 2007.

[33] Seunghee Lee, Peter C. Doerschuk, and John E. Johnson. Reciprocal space

representation of helical objects and their projection images for helices constructed from motifs without spherical symmetry. *Ultramicroscopy*, 2008. In press.

[34] Yili Zheng. *Novel statistical models and a high-preformance computing toolkit for the solution of cryo electron microscopy inverse problems in viral structural biology*. PhD thesis, School of Electrical and Computer Engineering, Purdue University, West Lafayette, Indiana, USA, August 2008.

[35] Junghoon Lee. *A fast algorithm for maximum likelihood 3-D signal reconstruction from 2-D projections of unknown orientation and applications to the electron microscopy of viruses*. PhD thesis, School of Electrical and Computer Engineering, Purdue University, West Lafayette, Indiana, USA, December 2006.

[36] Marin van Heel. Similarity measures between images. *Ultramicroscopy*, 21:95–100, 1987.

[37] George Harauz and Marin van Heel. Exact filters for general geometry three dimensional reconstruction. *Optik*, 73(4):146–156, 1986.

[38] N. Grigorieff. Resolution measurement in structures derived from single particles. *Acta Cryst.*, D56:1270–1277, 2000.

[39] Marin van Heel and Michael Schatz. Fourier shell correlation threshold criteria. *J. Struct. Biol.*, 151:250–262, 2005.

[40] Joachim Frank. *Three-Dimensional Electron Microscopy of Macromolecular Assemblies*. Academic Press, San Diego, 1996.